

THE UNIVERSITY OF CHICAGO

SYNTHESIS OF COLLOIDAL SEMICONDUCTOR NANOCRYSTALS
IN UNCONVENTIONAL CIRCUMSTANCES:
HETEROGENEOUS MIXTURES AND HIGH-PRESSURE REACTORS

A DISSERTATION SUBMITTED TO
THE FACULTY OF THE DIVISION OF THE PHYSICAL SCIENCES
IN CANDIDACY FOR THE DEGREE OF
DOCTOR OF PHILOSOPHY

DEPARTMENT OF CHEMISTRY

BY
WOOJE CHO

CHICAGO, ILLINOIS

JUNE 2023

TABLE OF CONTENTS

LIST OF FIGURES	iv
LIST OF TABLES	ix
ACKNOWLEDGEMENTS	x
ABSTRACT	xiii
INTRODUCTION	1
CHAPTER ONE	
DIRECT SYNTHESIS OF COLLOIDAL SIX-MONOLAYER-THICK CADMIUM SELENIDE NANOPLATELETS	4
1.1. Development of Six-Monolayer-Thick CdSe Nanoplatelets	5
1.2. Brief Description on Synthesis of 6ML CdSe NPLs	6
1.3. Measured Properties of Directly Synthesized 6ML CdSe NPLs	7
1.4. A Growth Model for 6ML CdSe NPLs	11
1.5. Applications of 6ML CdSe NPLs	16
1.6. Open Question on Tuning Emission Wavelengths of CdSe NPLs	17
1.7. Summary and Outlook	20
1.8. Experimental Details	21
CHAPTER TWO	
SYNTHESIS OF COLLOIDAL GALLIUM NITRIDE AND ALUMINUM NITRIDE NANOCRYSTALS IN BIPHASIC MOLTEN SALT / ORGANIC SOLVENT MIXTURES	25
2.1. Importance of Colloidal Gallium Nitride and Aluminum Nitride Nanocrystals	26
2.2. Developments of Growth Methods for GaN and AlN Crystals	27
2.3. Limitations on Solution Synthesis of GaN and AlN Nanocrystals	28
2.4. General Considerations for the Solution Synthesis of GaN and AlN	30
2.5. Formation of GaN and AlN Nanocrystals in Solution	36
2.6. Formation of GaN Nanocrystals from a Biphasic Mixture	42
2.7. Nanocrystal Growths in a Molten Salt Phase	44

2.8. Solution Synthesis of III-Nitride Nanostructures Using High-Pressure Ammonia	47
2.9. Summary and Outlook	53
2.10. Experimental Details	54
2.11. Simulation Details	61
CHAPTER THREE	
HIGH-PRESSURE REACTOR SYSTEMS	63
3.1. A General Description on a High-Pressure Reactor System	67
3.2. Air-Free High-Pressure Reactor Systems	69
3.3. Example Experiments with High-Pressure Reactors	80
3.4. Summary and Outlook	85
REFERENCES	86

LIST OF FIGURES

Figure 1.1. (A) A TEM image of face-up 6ML CdSe NPLs. Inset: A high resolution TEM image of 6ML CdSe NPLs. (B) A high resolution TEM image of stacked 6ML CdSe NPLs. Adapted with permission from Ref. [19]. Copyright 2018 American Chemical Society. 7

Figure 1.2. (A) A PXRD pattern of 6ML CdSe NPLs. Vertical lines at the bottom show the X-ray reflections of bulk zinc-blende CdSe. (B) Raman spectrum of 6ML CdSe NPLs. (C) High resolution TEM image of a face-up 6ML CdSe NPL. (D) FFT conversion of (C) showing zinc-blende pattern from the [001] orientation. Adapted with permission from Ref. [19]. Copyright 2018 American Chemical Society. 8

Figure 1.3. (A) Absorption (black) and PL emission (red) spectra of 6ML CdSe NPLs. (B) A calculated fitting (dotted straight line) of peak position from Pidgeon-Brown model²⁵, compared to absorption spectrum of 6ML CdSe NPL (black line) and its 2nd derivatives (red line). (C) PL emission spectra of CdSe NPLs of different thicknesses from 3ML to 6ML. (D) PL emission and PLE spectra measured at different excitation wavelengths for 6ML CdSe NPLs. Adapted with permission from Ref. [19]. Copyright 2018 American Chemical Society. 9

Figure 1.4. Time-resolved PL of 6ML CdSe NPLs. The half-life of the PL was 4.3 nanoseconds. Adapted with permission from Ref. [19]. Copyright 2018 American Chemical Society. 10

Figure 1.5. Absorption and emission spectra from 6ML CdSe NPLs made with various sources of chlorides. Adapted with permission from Ref. [19]. Copyright 2018 American Chemical Society.11

Figure 1.6. (A) Scheme for the growth model of CdSe NPLs reported in Ref. [21], showing nucleated islands on a wide facet and a narrow facet. (B) Energy change of NPLs caused by an island formation on wide and narrow facets by area of the island. Following Ref. [21], E_V of -2.2 meV/\AA^3 , E_A of 5.7 meV/\AA^2 , and E_L of 37.1 meV/\AA were used. Blue dot represents the highest point of wide facet energy curve. Red dot and red X mark represent the intersections of wide facet and narrow facet energy curves of 5ML and 6ML, respectively. Adapted with permission from Ref. [19]. Copyright 2018 American Chemical Society. 12

Figure 1.7. (A) A map showing synthesizability of NPLs by edge energy (E_L) and surface energy (E_A) at the volume energy (E_V) of -2.2 meV/\AA^3 . Red circle represents the point with E_A of 5.7 meV/\AA^2 and E_L of 37.1 meV/\AA . Up to 5ML NPLs can form. (B) A map showing synthesizability of NPLs by E_L and E_A at the E_V of -1.8 meV/\AA^3 . Red circle represents the point with E_A of 5.7 meV/\AA^2 and E_L of 37.1 meV/\AA . Up to 7ML NPLs can be synthesized. Adapted with permission from Ref. [19]. Copyright 2018 American Chemical Society. 14

Figure 1.8. X-ray fluorescence (XRF) spectra of 6ML CdSe NPLs and the composition obtained from the fits. Adapted with permission from Ref. [19]. Copyright 2018 American Chemical Society. 15

Figure 1.9. (A) PL spectra of ASE measurement. Inset: Integrated PL area vs. pump fluence showing ASE threshold at $21 \mu\text{J}/\text{cm}^2$. (B) Absorption and emission spectra of 6ML CdSe NPL core and nCdZnS/6CdSe/nCdZnS ($n = 1, 2$) core-shell nanoheterostructure. Dotted lines represent absorption spectra, and solid lines illustrate emission spectra. Adapted with permission from Ref. [19]. Copyright 2018 American Chemical Society. 16

Figure 1.10. 3D contour mapping of PL intensity by excitation and emission wavelengths for (A) 6ML CdSe NPL and (B) 6ML CdSe-CdZnS core-shell structure. Adapted with permission from Ref. [19]. Copyright 2018 American Chemical Society. 17

Figure 1.11. Absorption and emission spectra of 6ML CdSe NPLs synthesized (A) without chloride and (B) with chloride ions. 18

Figure 1.12. The fitting curve of emission wavelengths by the number of additional monolayers to 3ML NPLs. 19

Figure 2.1. The parameter space accessible for traditional solution synthesis compared to the conditions optimized for chemical vapor deposition (CVD) and bulk crystal growth of GaN and AlN crystals and films. Reprinted with permission from Ref. [20]. Copyright 2023 American Chemical Society. 29

Figure 2.2. PXRD pattern of the product obtained by heating of gallium stearate and ammonia in trioctylamine. The reference pattern is from a previously reported gallium oxynitride spinel. Reprinted with permission from Ref. [20]. Copyright 2023 American Chemical Society. 31

Figure 2.3. A reaction scheme for reactions of 0.1-0.2 M gallium and aluminum halides with NH_3 at 290°C in trioctylamine/hexadecylamine (TOA/HDA) solution. Adapted with permission from Ref. [20]. Copyright 2023 American Chemical Society. 32

Figure 2.4. PXRD patterns measured from the products of the reactions of 0.1-0.2 M gallium halide or aluminum halide with excess NH_3 in TOA/HDA solution. The vertical lines show the positions and relative intensities for bulk zinc-blende (ZB, blue vertical lines) GaN, wurtzite (WZ, black vertical lines) GaN, and wurtzite (WZ, red vertical lines) AlN phases. Reprinted with permission from Ref. [20]. Copyright 2023 American Chemical Society. 33

Figure 2.5. (A) The atomic pair distribution function (PDF) measured for the products of the reaction between 0.2 M GaCl_3 and excess NH_3 in TOA/HDA solution. The experimental data (black line) are compared with the simulated PDF (red line) of a 1-nm-diameter wurtzite GaN nanocrystal (inset cartoon). (B, C) PDFs of the product of the reaction between 0.1 M AlBr_3 and excess NH_3 in TOA/HDA solution. Inset figures represent the structures used for simulations. The experimental data (black line) are compared with the simulated PDFs (red line) of a 1-nm-diameter spherical WZ AlN crystal (B) and a molecular 4-membered-ring AlN structure (C). Adapted with permission from Ref. [20]. Copyright 2023 American Chemical Society. 35

Figure 2.6. A reaction scheme for reactions of 1 M gallium and aluminum halides with NH_3 at 290°C in trioctylamine/hexadecylamine (TOA/HDA) solution yielding crystalline phases. Adapted with permission from Ref. [20]. Copyright 2023 American Chemical Society. 37

Figure 2.7. Photographs of a colloidal solution of GaN nanoparticles under ambient light (left) and under illumination with 302 nm ultraviolet (UV) light (right). Under UV, the solution glows yellow due to emissions from midgap states. Adapted with permission from Ref. [20]. Copyright 2023 American Chemical Society. 38

Figure 2.8. PXRD patterns from synthesized GaN nanocrystals and simulated GaN nanocrystals. (A) PXRD patterns of GaN nanocrystals synthesized by reacting NH_3 with GaCl_3 (black curve), GaBr_3 (red curve), and GaI_3 (blue curve) with reference lines from wurtzite (WZ, black vertical lines) and zinc blende (ZB, blue vertical lines) bulk GaN phases. (B) A PXRD pattern of a simulated WZ GaN nanorod with 2-nm diameter and 9-nm length. (C) A PXRD pattern of a simulated spherical ZB GaN nanocrystal with 4-nm diameter. Adapted with permission from Ref. [20]. Copyright 2023 American Chemical Society. 39

Figure 2.9. TEM images from synthesized GaN nanocrystals. Insets show high-resolution TEM images (A) A TEM image of WZ GaN nanorods and nanotetrapods synthesized using GaCl_3 . (B) A TEM image of WZ GaN nanorods synthesized using GaBr_3 . The image also shows spherical particles. (C) A TEM image of ZB GaN nanocrystals synthesized using GaI_3 . Adapted with permission from Ref. [20]. Copyright 2023 American Chemical Society. 39

Figure 2.10. PDFs from GaN nanocrystals synthesized with GaCl_3 (A, D), GaBr_3 (B, E), and GaI_3 (C, F) under ambient-pressure ammonia. The long-wavelength damped sine waves observed in (D) and, to a lesser extent, (E) are often present in experimental PDF data. These can originate from an imperfectly corrected background. Reprinted with permission from Ref. [20]. Copyright 2023 American Chemical Society. 40

Figure 2.11. (A) A PXRD pattern of AlN nanorods synthesized from AlBr_3 (black curve) with reference lines from WZ AlN phase (vertical lines). (B) A PXRD pattern of a simulated WZ AlN nanorod with 2-nm diameter and 9-nm length. (C) A TEM image of AlN nanorods. The inset shows a high-resolution TEM image. AlN nanorods are marked with dotted red lines. Adapted with permission from Ref. [20]. Copyright 2023 American Chemical Society. 41

Figure 2.12. Photographs of hot mixtures of gallium salts and alkylamines. (A) A mixture of 0.5 mmol KGaCl_4 , 2 mL of TOA, and 0.3 g of HDA at elevated temperatures (250 °C). (B) A mixture of 0.5 mmol GaCl_3 , 2 mL of TOA, and 0.3 g of HDA at elevated temperatures (250 °C). The KGaCl_4 mixture had a clear separation between an upper organic phase with a white emulsion and a lower, clear molten salt phase. The GaCl_3 mixture became a clear homogeneous solution. Reprinted with permission from Ref. [20]. Copyright 2023 American Chemical Society. 43

Figure 2.13. PXRD patterns obtained from the products of hot-injection approaches with mixtures of 1 mmol of gallium salt (KGaCl_4 or GaCl_3), 4 mL of TOA, and 0.6 g of HDA. Reprinted with permission from Ref. [20]. Copyright 2023 American Chemical Society. 44

Figure 2.14. Cartoons depicting microscopic reversibility during synthesis of II-VI and III-nitride nanocrystals. Yellow circles represent monomers of the corresponding system, and red squares illustrate ions in molten salts. Adapted with permission from Ref. [20]. Copyright 2023 American Chemical Society. 45

Figure 2.15. The free energy landscapes for the elementary step of breaking Ga-N surface bonds required for establishing microscopic reversibility. (A) A breaking step of Ga-N surface bond separates charges in a non-polar medium, increasing the energy of the system in large degree. (B) A highly polarizable molten salt medium facilitates rearrangement of surface Ga-N bonds during nanocrystal growth by effectively balancing charges upon breaking of a surface Ga-N bond. Adapted with permission from Ref. [20]. Copyright 2023 American Chemical Society. 47

Figure 2.16. (A) PXRD patterns of GaN nanorods produced using different ammonia pressures. Black vertical lines correspond to a WZ GaN reference. (B) A TEM image of GaN nanostructures synthesized using 5-MPa ammonia. The inset shows a high-resolution TEM image of GaN nanorods. (C, D) Simulated PXRD patterns of WZ GaN nanorods with different thicknesses (C) and different numbers of stacking faults (D). Adapted with permission from Ref. [20]. Copyright 2023 American Chemical Society. 48

Figure 2.17. A PDF pattern of GaN nanorods synthesized with ammonia at 5 MPa. (E) Shorter range data (black line) in pair with a simulated PDF pattern (red line) from WZ GaN nanorod with 2-nm diameter and 9-nm length (inset cartoon). (F) A longer range PDF reveals [0002] planes of WZ GaN. Adapted with permission from Ref. [20]. Copyright 2023 American Chemical Society. 50

Figure 2.18. Optical properties of GaN nanorods synthesized using high-pressure ammonia. (A) Absorption spectra of GaN nanorods dispersed in methylcyclohexane produced using different ammonia pressures. Small artifacts between 250-270 nm are from trace amounts of residual toluene. (B) Photoluminescence (PL, black curves) and photoluminescence excitation (PLE, colored curves) spectra of GaN nanorods from synthesis with 5 MPa ammonia. Arrows indicate the monitored emission wavelengths of PLE spectra of corresponding colors. The PLE spectra hint that the populations of thicker nanorods emit from midgap states of lower energy. Reprinted with permission from Ref. [20]. Copyright 2023 American Chemical Society. 51

Figure 2.19. (A) Absorbance (solid lines) and photoluminescence (dashed lines) of colloidal GaN nanoparticles synthesized with GaCl₃ (black curves), GaBr₃ (red curves), and GaI₃ (blue curves). (B) Photoluminescence of stoichiometric mixture of GaCl₃ and oleylamine diluted in methylcyclohexane. Adapted with permission from Ref. [20]. Copyright 2023 American Chemical Society. 53

Figure 2.20. A scheme for the high-pressure reactor setup. Reprinted with permission from Ref. [20]. Copyright 2023 American Chemical Society. 57

Figure 2.21. Enhancement of high-resolution TEM images. (A) Scheme for the enhancement. (B) Side-by-side comparison of an image of a GaN nanoparticle before (left) and after enhancement (right). Reprinted with permission from Ref. [20]. Copyright 2023 American Chemical Society. 59

Figure 3.1. A flow diagram for a basic high-pressure reactor system. 68

Figure 3.2. A flow diagram for an air-free high-pressure reactor system with a transparent thick-glass reactor vessel. 71

Figure 3.3. A flow diagram for high-pressure reactor system for high-pressure ammonia delivery.	72
Figure 3.4. A flow diagram for high-pressure reactor system during ammonia fill to an ammonia reservoir.	73
Figure 3.5. A flow diagram for high-pressure reactor system with a gas booster.	76
Figure 3.6. A flow diagram of a high-pressure reactor system with a capability of high-pressure injection and aliquoting.	78
Figure 3.7. (A) Powder X-ray diffraction (PXRD) pattern, (B) TEM image, and (C) high-resolution of TEM image of produced particles from the reaction of GaI ₃ in iodide eutectic and ammonia.	81
Figure 3.8. Hot isostatic pressing of ZnS and ZnSe nanoparticle films. (A) Optical microscopy and (B) SEM image of film of ZnSe nanoparticles after hot isostatic pressing at 270 °C and 15000 psi (100 MPa). (C) SEM image of film of ZnS nanoparticles after hot isostatic pressing at 450 °C and 15000 psi (100 MPa). (D) Refractive indices of ZnSe nanoparticle films before and after hot isostatic pressing. (E) Refractive indices of ZnS nanoparticle films before and after hot isostatic pressing. Adapted with permission from Ref. [115]. Copyright 2022 American Chemical Society.	84

LIST OF TABLES

Table 3.1. Descriptions on parts used in flow diagrams.	65
--	----

ACKNOWLEDGEMENTS

First, I would like to thank my research adviser, Professor Dmitri V. Talapin. It was a great fortune for me to work with him and learn from him. He is not only intellectually keen and inspirational, but also with an extraordinary personality. His advices on scientific projects from fundamental explorations to an ultimate goal have provided me much help from building essential details in the projects to understanding broader impacts of the projects. Also, he has been always supportive and patient about my research projects. In addition, I want to mark his agile leadership and willingness to learn. He is not only eager to absorb scientific knowledge, but also always tries to accept different opinions and to adopt better lab cultures. It has been very impressive for me to observe the whole lab has been keep evolving. Finally, I want to appreciate his hard work in finding the financial support for the group. All of my costly works would have not been possible without his great effort.

I would like to thank my committee members, Professor Jiwoong Park and Professor John Anderson, for their time and effort they spent for my dissertation and valuable comments on the dissertation and the defense presentation. I also appreciate their advices and considerations on my future career path.

I also appreciate kind introduction by the Talapin laboratory, as well as delightful discussions and collaborations with the group members. Dr. Igor Fedin taught me all basic experiments in our lab including CdSe nanoparticle synthesis. Dr. J. Matthew Kurley taught me many laboratory infrastructures and their operations. Dr. Abhijit Hazarika introduced me to high-temperature colloidal atomic layer deposition. Dr. Patrick D. Cunningham taught me synthesis of

ZnSe nanoplatelets. Dr. Eric M. Janke introduced me to self-assembly of nanoparticles. Dr. Vishwas Srivastava, Dr. Margaret H. Hudson, and Dr. Vladislav Kamysbayev introduced me to molten salt chemistry. I also remember Dr. Maggie Hudson taught me basic skills about building and maintaining high-pressure reactors. I would like to thank our former group administrator Tanya Shpigel and current group administrator Dr. Andrew Nelson. I also want to appreciate all internal collaborations with Dr. Igor Fedin, Dr. Igor Coropceanu, Dr. Abhijit Hazarika, Dr. Vishwas Srivastava, Dr. Joshua Portner, Dr. Patrick D. Cunningham, Dr. Himchan Cho, Dr. Jia-Ahn Pan, Dr. Justin C. Ondry, Alex Hinkle, Dr. Chenkun Zhou, Di Wang, Zirui Zhou, and Ruiming Lin. I would like to thank each and every member of the Talapin group, current and former, Dr. Jun Hyuk Chang, Dr. James Cassidy, Haoqi Wu, Aritrajit Gupta, Ahhyun Jeong, Zehan Mi, William Burke, Young-Hwan Kim, Kavan Mulloy, Dr. Xinzheng Lan, Eleanor Dunietz, Ayat Tasanov, Dr. Yuanyuan Wang, Thomas Habte, Nivedina Sarma, Huicheng Hu, Min Chen, Jingxing Geng, Dr. Iryna Golovina.

I would like to thank my external collaborators. Argonne National Laboratory has been essential for my research. In a number of researches, I collaborated with Dr. Xuedan Ma. I also want to thank Prof. Richard D. Schaller and his group, especially Dr. Benjamin T. Diroll and Dr. Alexandra Brumberg. It has been a great pleasure to collaborate with them. I would like to appreciate collaborations with theoretical chemists, Prof. Guilia Galli, Dr. Márton Vörös, Dr. Siyoung Kim, Prof. Eran Rabani, and Dr. John Philbin. I would also like to thank Prof. Robert Klie and his group members, Dr. Liang Hong and Jinglong Guo, for their great imaging skills. Finally, I would like to thank Dr. Burak Guzelurk for his help in atomic pair distribution function measurements.

I would like to thank internal core facilities of the University of Chicago. Transmission electron microscopy has been essential for my studies, and I appreciate all helps from Yimei Chen. I also appreciate helps from our X-ray facility and thank the director, Dr. Alexander Filatov. I would like to appreciate the hard work of Dr. Justin E. Jureller and Dr. Qiti Guo making MRSEC facilities available for us. I would like to thank Dr. C. Jin Qin, the director of the Mass Spec Facility; Dr. Josh Kurutz, the director of the NMR Facility; Dr. Elena Solomaha, the director of the BioPhysics Core Facility; and Dr. Philip Griffin, the director of the Soft Matter Laboratory.

I would like to acknowledge all the works of the Department of Chemistry. Melinda Moore and Dr. Vera Dragisich have provided me great helps whenever necessary. I also want to appreciate hard works of our former and current building managers, John Philips and Bentley Wall.

I was fortunate to have good friends during my graduate school years. I would like to thank Prof. Hyun June Park, Minsu Kim, Prof. Do Young Lee, Dr. Daniel Edmiston, Dr. Eunki Min, Seoyeon Choi, Dr. Hyeondo Luke Hwang, Dr. Donghyuk Suh, Dr. Gihoon Lee, Dr. Jaehyeok Jin, Injae Kim, DS Dasom Seo, Prof. Sangjin Lee, and Prof. Joshua Byun. I want to thank all Hyde Park Korean United Methodist Church members. I would also like to thank my old friends, Dr. Andrew Bae, Dr. Yehun Park, Dr. Young Hwi Kim, Dr. Hyunsuk Yoo, Dr. Minsuk Hyun, Dr. Andy Park, Jason Song, Dr. Sunny Kim, and Sangyoon Park.

Finally, I owe my special gratitude to my family. I thank my parents Yong Bong Cho and Jae Hyang Lee for their love, support, and faith in me. I also thank my aunt, Minjun Lee; uncles, Jae-Hyuk Yi and Myung-Ryul Lee; and my cousins, Ellie Dayong Lee, Soonyong Lee, Layna Lee, with their families.

ABSTRACT

Colloidal semiconductor nanocrystals have been widely synthesized in solution. Well-optimized solution synthesis can produce colloidal nanocrystals with great controls on their shapes, sizes, and size distributions. Solution synthesis not only is good in tenability of nanocrystals but also has great advantages in scalability, and consequent cost reduction in both nanocrystal productions and device applications. However, this great method is not applicable to all semiconductor materials. Group XIII nitrides are such materials difficult to produce in desirable quality in solution synthesis. Also solution synthesis is limited in temperature and pressure ranges, due to decomposition of organic molecules at high temperature and use of glass apparatus which cannot bear high pressure difference. Here, two ways to overcome limits in reaction conditions of solution synthesis are discussed: incorporation of biphasic reaction media and high-pressure reaction environment. It is proven that molten salt droplets immiscible with non-polar solvent can be interesting media for nanoparticle growth. Chapter One discusses about synthesis of six-monolayer CdSe nanoplatelets. To the known fact that zinc blende (ZB) CdSe nanoparticles grow laterally into nanoplatelets (NPLs) in molten cadmium acetate droplets, a twist of adding cadmium chloride is added to allow the CdSe NPL to grow thicker. Chapter Two explores solution synthesis of colloidal GaN and AlN nanocrystals enabled with incorporation of molten salt phase to non-polar solution. Chapter Two also discusses about a pressure control of an ammonia reactant, showing that a crystal size of GaN nanoparticles can be systematically tuned with the ammonia pressure. Chapter Three explains high-pressure reactor systems for nanomaterials science in detail.

INTRODUCTION

Colloidal semiconductor nanocrystals have been widely synthesized in solution.¹⁻⁶ The preparation of nanocrystals by colloidal solution synthesis methods provides significant advantages not only in the form of optical tunability via size and shape control but also of scalability and cost reduction in nanoparticle production and solution-based device integration.⁴⁻⁶

A conventional colloidal synthesis of nanoparticles utilizes homogeneity of solution to induce homogeneous nucleation and growth of nanoparticles. Though nucleation and growth of nanoparticles are not yet completely understood, formation of nanoparticles have been rationalized in many theoretical and experimental works based on classical nucleation and growth theory.⁷⁻¹³ LaMer mechanism⁸ was the first mechanism, that explains nanoparticle formation in three separate stages: 1) building up a concentration of free monomers, 2) burst of nucleation induced by oversaturation, and 3) decrease of monomer concentration and growth of nanoparticle with diffusion of monomers. While LaMer mechanism clearly separates nucleation and growth stages in relation with monomer concentrations, it has been also known that nucleation and growth stages can overlap in growing nanoparticles.⁹⁻¹⁰ Multiple ripening and growth processes of nanoparticles have been also suggested.¹¹⁻¹³ While Ostwald ripening suggests growth of larger particles at the

expense of smaller particles, digestive ripening process is also known where smaller particles grow with surface etching of larger particles.

Well-controlled nucleation and growth allow colloidal semiconductor nanoparticles to grow with great controls on size, size distribution, and shape.¹⁻⁶ For example, CdSe nanocrystals are not only able to be produced with various shapes but can have systematic size controls and near-atomic preciseness in their size.¹⁴⁻¹⁹ On the contrary, there are also material systems not established well for colloidal nanoparticle synthesis. Group XIII nitrides (III-nitrides) are semiconductor materials lacking well-established synthetic methods for colloidal nanoparticle synthesis.²⁰ Whereas bulk crystals of III-nitride materials have been widely manufactured and utilized, colloidal nanocrystals of III-nitrides have been rarely reported. Synthesis of III-nitride bulk materials requires high temperature and often elevated pressure, which have been incompatible with conventional solution synthesis of nanoparticles. Glass apparatus widely used for solution synthesis cannot bear large pressure difference as well as many solvents and surfactants containing long hydrocarbon chains start to decompose at temperature above 400 °C. This discrepancy in the reaction parameter between bulk III-nitride synthesis and solution synthesis hints why solution synthesis of III-nitride has been under-explored.

Here, two ways of expanding reaction conditions of solution synthesis are discussed: incorporation of biphasic reaction media and high-pressure reaction environment. It is proven that molten salt droplets immiscible with non-polar solvent can be interesting media for nanoparticle growth.²⁰⁻²¹ It is known that zinc blende (ZB) CdSe nanoparticles grow laterally into nanoplatelets (NPLs) in molten cadmium acetate.²¹ Chapter One discusses about a twist to the CdSe NPL synthesis to enable formation of a thicker population, six-monolayer CdSe NPLs. Chapter Two

explores solution synthesis of colloidal GaN and AlN nanocrystals enabled with incorporation of molten salt phase to non-polar solution. Chapter Two also discusses about a pressure control of an ammonia reactant, showing that a crystal size of GaN nanoparticles can be systematically tuned with the ammonia pressure. Chapter Three explains high-pressure reactor systems for nanomaterials science in detail.

CHAPTER ONE

DIRECT SYNTHESIS OF COLLOIDAL

SIX-MONOLAYER-THICK CADMIUM SELENIDE NANOPATELETS¹⁹

The synthesis of II-VI nanoplatelets has enabled virtually complete elimination of inhomogeneous spectral broadening and redefined the color purity of fluorescence emission achievable for colloidal nanomaterials. For a decade, a belief has risen that CdSe nanoplatelets cannot be directly synthesized with a thickness greater than 2.5 unit cells (~1.5 nm). In this work, we overcome this boundary by establishing a synthesis for six-monolayer-thick CdSe nanoplatelets. By simply introducing hydroxide or chloride ions in a standard CdSe nanoplatelet synthesis, six-monolayer thick nanoplatelets can be synthesized in high quality. We discuss the role of small ions on nanoplatelet nucleation and growth. This work demonstrates characteristics and possible applications of six-monolayer-thick CdSe nanoplatelets.

1.1. Development of Six-Monolayer-Thick CdSe Nanoplatelets

Quasi-2-dimensional semiconductor nanoplatelets (NPLs) have garnered widespread interest because of their uniquely narrow emission spectra and favorable characteristics for optical gain and lasing.²²⁻²⁶ Strongly quantum confined along thickness, NPLs exhibit the electronic structure of quantum wells determined by their thickness, which can be controlled with atomic precision.²⁷⁻³¹ Among all semiconductor NPLs, CdSe NPLs are probably the most studied. So far, four kinds of CdSe NPLs, emitting at around 396nm, 463nm, 513nm, and 553nm, have been intensely investigated for almost a decade.^{14,32-38} Despite some early confusions in identifying actual thicknesses of those NPLs, it has been successfully assigned to be 2-monolayer (2ML) to 5-monolayer (5ML) thickness by high-resolution TEM.³⁹ Another kind of NPLs with 6MLs of CdSe, once briefly mentioned in 2013,⁴⁰ however, was not explored, likely because its synthesis proved hard to reproduce. 6ML CdSe NPLs could be prepared by the colloidal atomic layer deposition (c-ALD) method,⁴¹ but there had been no reports on direct synthesis of 6ML CdSe NPLs, and their direct synthesis had been doubted as being difficult.^{21,42}

We reported a reproducible method to obtain 6ML CdSe NPLs through a direct colloidal synthesis route. In short, the synthesis is based on the conventional way of synthesizing CdSe NPLs⁴³⁻⁴⁴ with a modification of adding small anions such as hydroxides and chlorides. Formation of 6ML CdSe NPLs does not refute the belief of the absence of 6ML CdSe NPLs in traditional syntheses;^{21,42} yet it shows that an additional control can be enabled over CdSe NPL synthesis, with a small change in chemical conditions. Basic characterizations were performed with transmission electron microscopy (TEM), powder X-ray diffraction (PXRD), absorption spectroscopy, photoluminescence (PL), and amplified spontaneous emission (ASE). Having a

sharp PL emission, 6ML CdSe NPLs can be used to generate an orange-colored ASE (~610 nm) or a color-pure red PL (~630 nm) emission by growing CdZnS shells.

1.2. Brief Description on Synthesis of 6ML CdSe NPLs

The 6ML CdSe NPL synthesis is based on known methods of producing CdSe NPLs of other thicknesses.⁴³⁻⁴⁴ In a typical synthesis, 170 mg of cadmium myristate and 14 mL of 1-octadecene (ODE) were mixed in a 100 mL three-neck round-bottom flask and degassed under vacuum at 85 °C for 30 minutes. Then, the mixture was heated to 250 °C under nitrogen flow. At 250 °C, 12 mg of Se powder well dispersed in 1mL of ODE with 5-minute sonication was quickly injected (<1 second) to the reaction mixture under vigorous stirring. After 20 seconds, 60 mg of cadmium acetate hydrate was added to the reaction flask and the reaction mixture was stirred for another 60 seconds. Then, 0.15 mL of 0.5 M cadmium chloride aqueous solution was slowly introduced into the reaction flask dropwise in a span of 2 minutes. After another 3 minutes, the flask was rapidly cooled to room temperature using compressed air. While the reaction mixture was being cooled down, a solution containing 2 mL of oleic acid in 15 mL of methylcyclohexane (MCH) was injected into the reaction flask at around 150 °C. NPLs were first separated from the reaction batch by centrifugation and dispersed in a minimal amount of MCH. Due to the water added during the synthesis (a bad solvent for oleate-capped nanocrystals), most of the particles were precipitated in the centrifugation, including smaller quantum dots. By adding an excess amount of hexanes, smaller quantum dot byproducts could be washed out after centrifugation. The remaining precipitate was dispersed in MCH and impurities including irregularly shaped particles and 5ML CdSe NPLs were removed by size-selective precipitation.

1.3. Measured Properties of Directly Synthesized 6ML CdSe NPLs

TEM images revealed rectangular-shaped 6ML CdSe NPLs with lateral sizes of 21.0 ± 3.4 nm by 15.7 ± 1.8 nm (Figure 1.1 A). The thickness of the NPLs was 1.85 ± 0.16 nm as estimated from TEM images of stacked NPLs (Figure 1.1 B). This value matches with the dimension of 3 unit cells of zinc-blende CdSe, or 6 Se layers sandwiched between 7 Cd layers. The PXRD pattern, the Raman spectrum, and fast Fourier transforms (FFT) of the TEM images confirmed that the NPLs crystallize in the cubic zinc-blende structure as CdSe NPLs of other thicknesses (Figure 1.2).^{14,44-45}

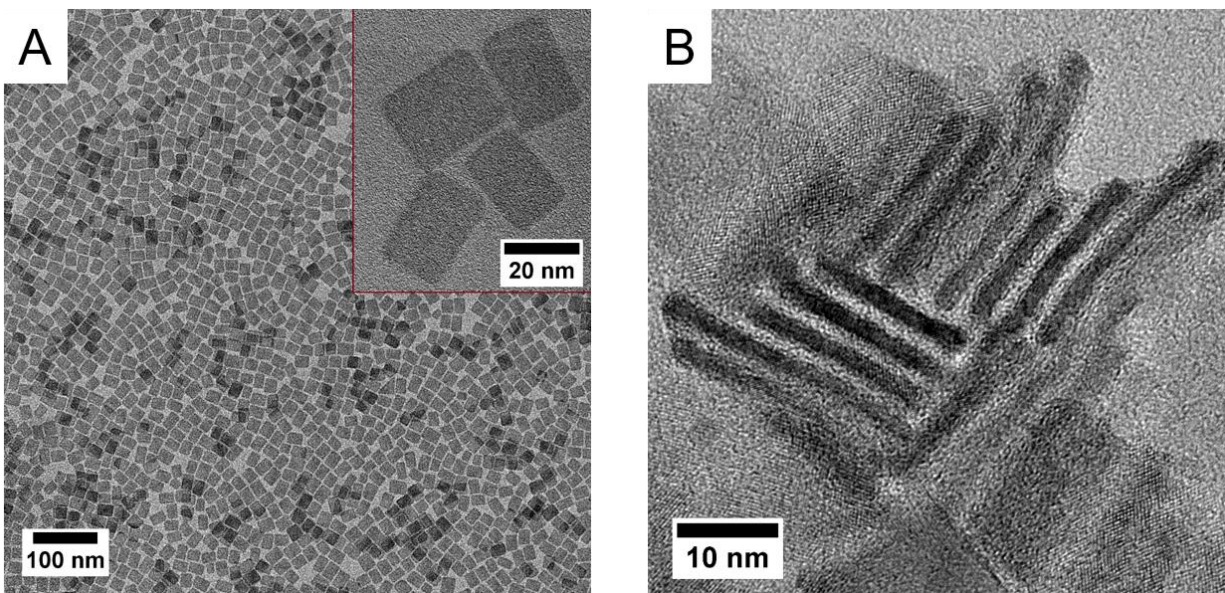


Figure 1.1. (A) A TEM image of face-up 6ML CdSe NPLs. Inset: A high resolution TEM image of 6ML CdSe NPLs. (B) A high resolution TEM image of stacked 6ML CdSe NPLs. Adapted with permission from Ref. [19]. Copyright 2018 American Chemical Society.

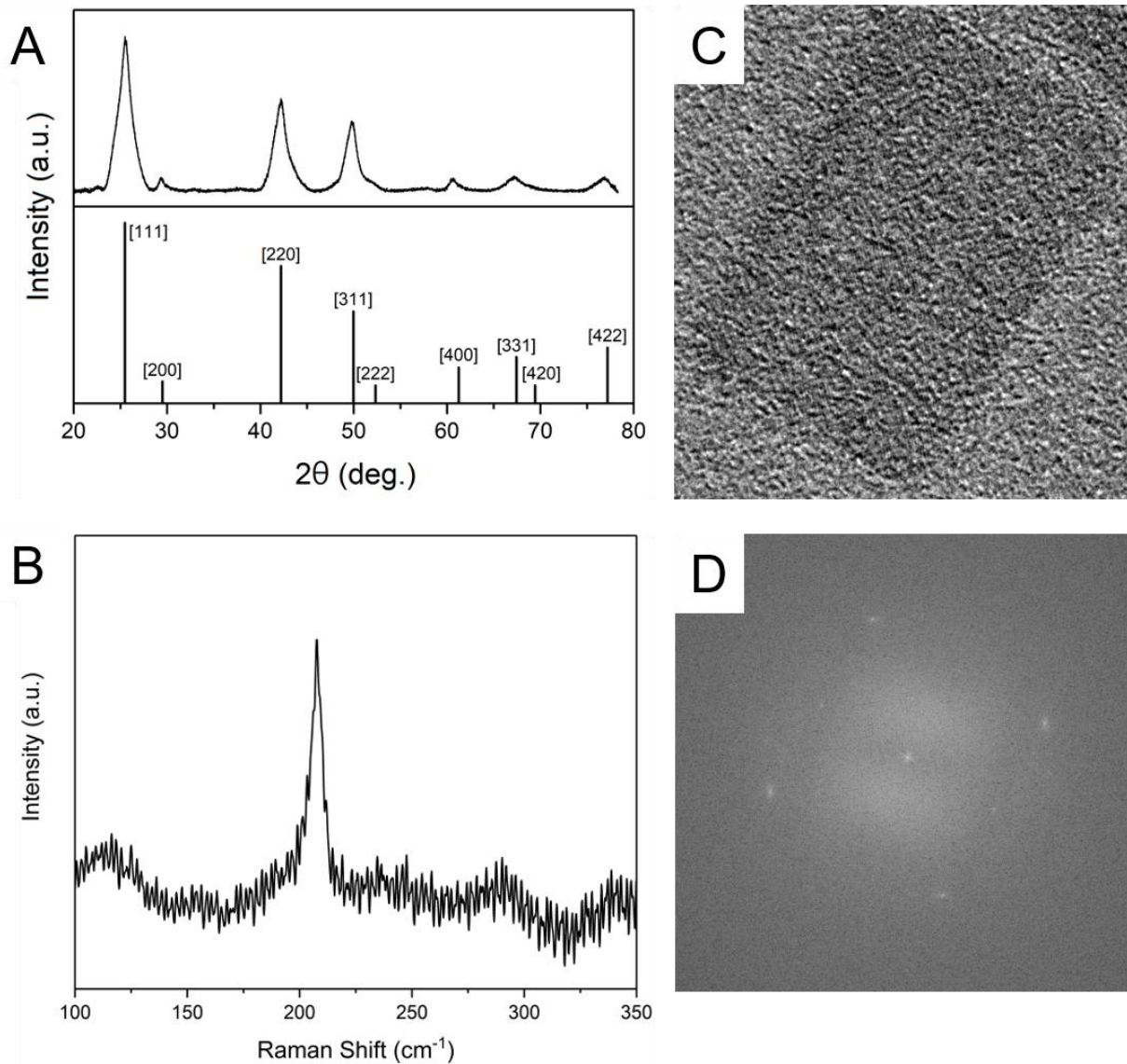


Figure 1.2. (A) A PXRD pattern of 6ML CdSe NPLs. Vertical lines at the bottom show the X-ray reflections of bulk zinc-blende CdSe. (B) Raman spectrum of 6ML CdSe NPLs. (C) High resolution TEM image of a face-up 6ML CdSe NPL. (D) FFT conversion of (C) showing zinc-blende pattern from the [001] orientation. Adapted with permission from Ref. [19]. Copyright 2018 American Chemical Society.

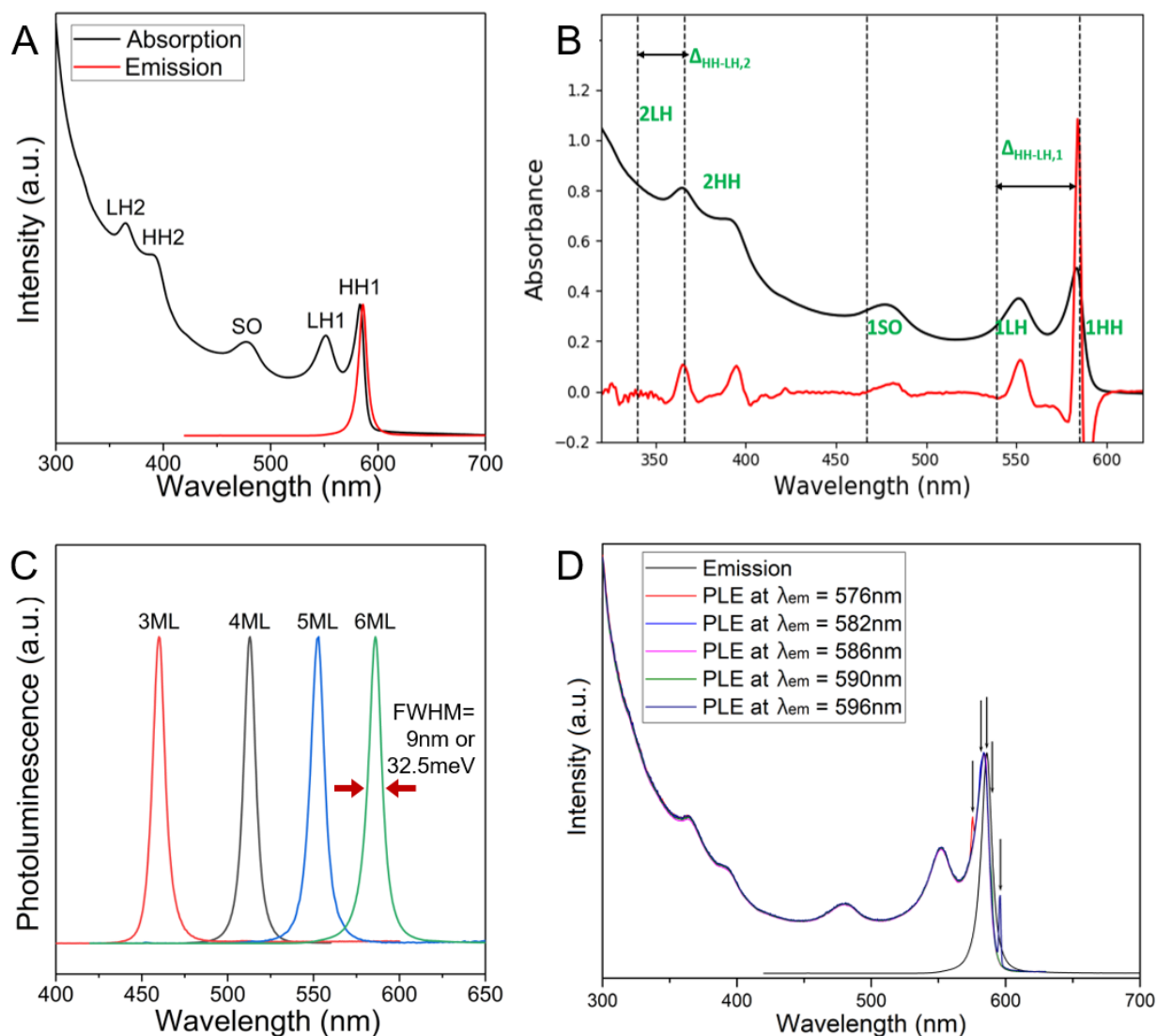


Figure 1.3. (A) Absorption (black) and PL emission (red) spectra of 6ML CdSe NPLs. (B) A calculated fitting (dotted straight line) of peak position from Pidgeon-Brown model²⁵, compared to absorption spectrum of 6ML CdSe NPL (black line) and its 2nd derivatives (red line). (C) PL emission spectra of CdSe NPLs of different thicknesses from 3ML to 6ML. (D) PL emission and PLE spectra measured at different excitation wavelengths for 6ML CdSe NPLs. Adapted with permission from Ref. [19]. Copyright 2018 American Chemical Society.

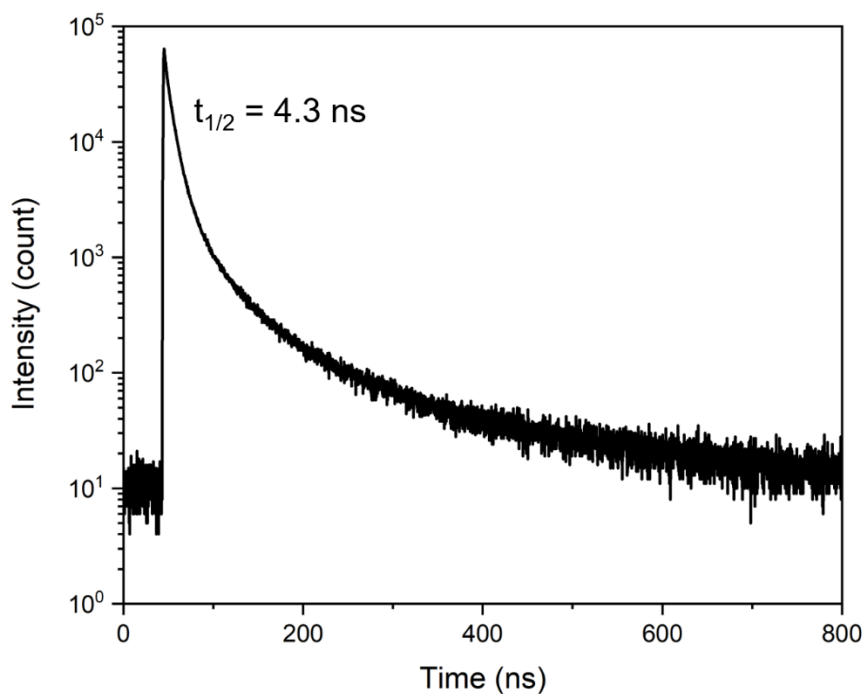


Figure 1.4. Time-resolved PL of 6ML CdSe NPLs. The half-life of the PL was 4.3 nanoseconds. Adapted with permission from Ref. [19]. Copyright 2018 American Chemical Society.

Well-resolved excitonic transitions could be seen in the absorption and PL spectra of the ensemble (Figure 1.3 A). The absorption had its first heavy-hole (HH1) and light-hole (LH1) excitonic peaks at 583 nm and 551 nm respectively, and the split-off hole (SO) transition at 477 nm. Two additional features were visible in the UV range at 392 nm and 364 nm, which can be attributed to transitions involving states from the second quantum well sub-band heavy-hole (HH2) and light-hole (LH2), respectively (Figure 1.3 B). PL emission peaked at 586 nm with the full width at half-maximum (FWHM) under 9 nm or 32.5 meV (Figure 1.3 C). A small Stokes shift between the HH1 and the emission band (~7 meV) also represented a common characteristic of CdSe NPLs. Photoluminescence excitation (PLE) spectra taken at various emission wavelengths

were almost identical suggesting that there was no inhomogeneous broadening of the emission band (Figure 1.3 D). 6ML CdSe NPLs could achieve 45% quantum yield and time-resolved PL of the NPLs showed similar decay with CdSe NPL of other thicknesses (Figure 1.4).⁴⁴

1.4. A Growth Model for 6ML CdSe NPLs

We found that water and chloride ions play an essential role in forming 6ML CdSe NPLs. The only difference in our system and traditional CdSe NPL synthesis was the addition of water or chloride ions. In the presence of different cations, water and chlorides repeatedly produced 6ML CdSe NPLs (Figure 1.5).

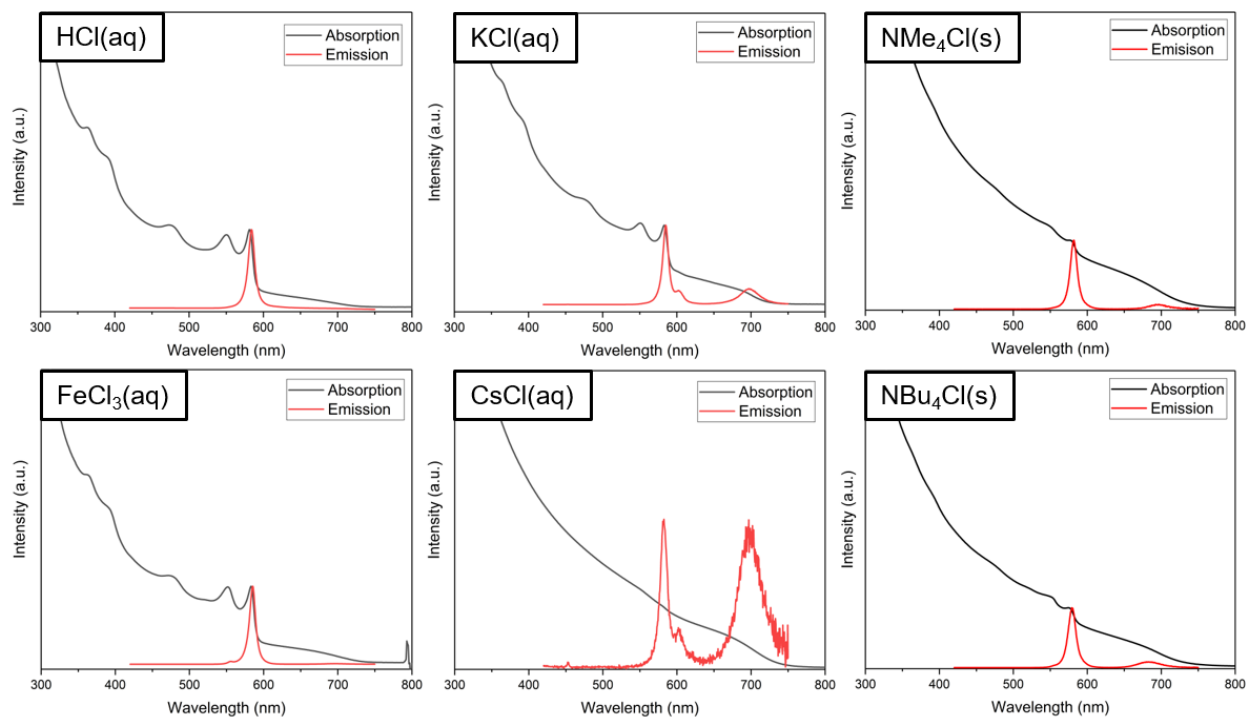


Figure 1.5. Absorption and emission spectra from 6ML CdSe NPLs made with various sources of chlorides. Adapted with permission from Ref. [19]. Copyright 2018 American Chemical Society.

According to the proposed NPL nucleation and growth model by the Norris group²¹, the formation of CdSe NPLs is controlled by the nucleation kinetics. This model is based on the fact that cadmium acetate is not soluble in ODE and its melt is not miscible with ODE. The authors also discovered that molten cadmium acetate liquid droplets in the reaction mixture are actual growth media of CdSe NPLs. In molten cadmium acetate, a monomer concentration is extremely high, and the growth conditions are controlled by the reaction kinetics rather than diffusion.

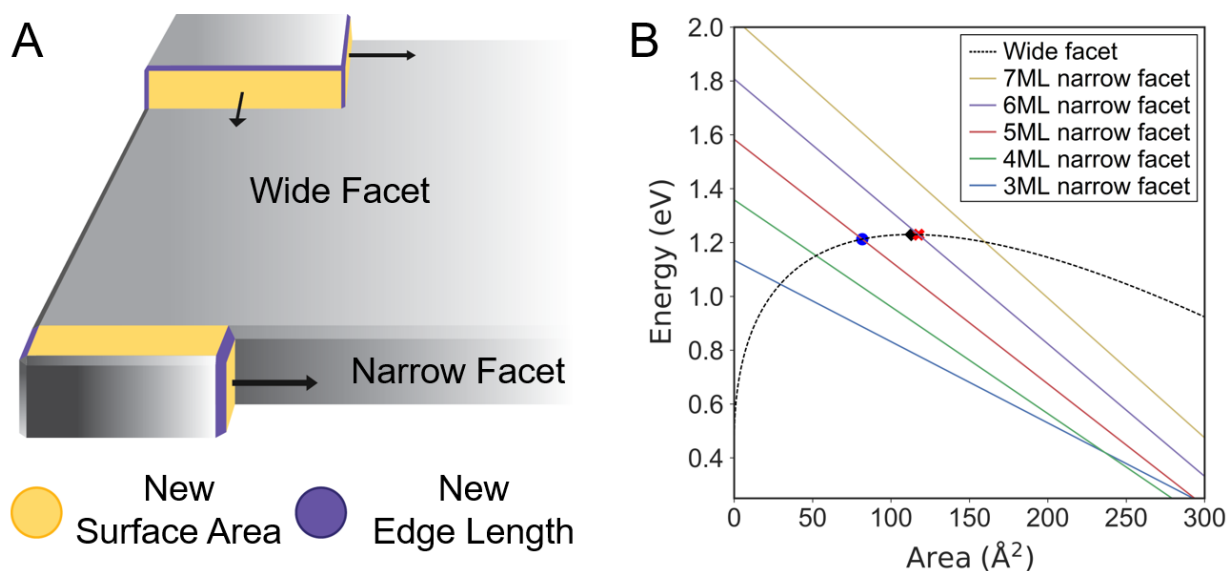
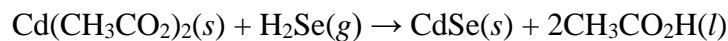


Figure 1.6. (A) Scheme for the growth model of CdSe NPLs reported in Ref. [21], showing nucleated islands on a wide facet and a narrow facet. (B) Energy change of NPLs caused by an island formation on wide and narrow facets by area of the island. Following Ref. [21], E_v of $-2.2 \text{ meV}/\text{\AA}^3$, E_A of $5.7 \text{ meV}/\text{\AA}^2$, and E_L of $37.1 \text{ meV}/\text{\AA}$ were used. Blue dot represents the highest point of wide facet energy curve. Red dot and red X mark represent the intersections of wide facet and narrow facet energy curves of 5ML and 6ML, respectively. Adapted with permission from Ref. [19]. Copyright 2018 American Chemical Society.

This model follows the general two-dimensional (2D) nucleation and growth theory⁴⁶; nanocrystal growth occurs through the nucleation of an island on the nanocrystal facet. In reaction-controlled growth, the growth of a nucleated island is fast and the rate-limiting step for the growth process is controlled by island nucleation barrier (ΔE). Energy change for a whole nanocrystal can be expressed as $\Delta E = \Delta V \cdot E_V + \Delta A \cdot E_A + \Delta L \cdot E_L$, accounting for the changes in volume (ΔV), surface area (ΔA), and edge length (ΔL), with specific energies for unit volume (E_V), surface area (E_A) and edge length (E_L). NPLs can be synthesized only under the condition where the nucleation on a narrow facet is thermodynamically favored over that on a wide facet. Otherwise, nanostructures grow in three dimensions (3D), forming quantum dots. According to the model (Figure 1.6), a nucleated island on 5ML narrow facet can be formed before that on wide facet, while that on 6ML narrow facet cannot. This explains the existence of 5ML NPLs and the absence of 6ML NPLs in conventional NPL syntheses.

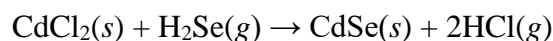
Following Norris's approach, availabilities of 3ML to 7ML NPLs are mapped for different values of E_L and E_A (Figure 1.7). In Figure 1.7 A, with given E_V , E_A , and E_L , 6ML NPL is not available. For constant E_V , 6ML is only available when E_A or E_L is increased. Considering steric crowding of carboxylate ligands on nanocrystal surfaces,⁴⁷⁻⁴⁸ an addition of small anionic ligands such as chlorides and possible hydroxides from water is expected to decrease rather than to increase E_L and E_A . X-ray fluorescence (XRF) measurements performed on purified 6ML CdSe NPLs estimated ~1.6 mol% of chlorine in the sample, which is equal to 10.4 mol% of total cadmium atoms on the surface of the NPLs (Figure 1.8). A possible explanation can come from an increased E_V . A small increase in E_V can avail 6ML formation (Figure 1.7 B).

E_V can be interpreted as a formation energy of a nucleated island, which is in a crude sense the heat of reaction:



$$\Delta_r H^\circ = -94.7 \text{ kJ/mol}$$

By adding cadmium chlorides to the reaction mixture, E_V can be increased on average because the reaction from cadmium chloride is endothermic:



$$\Delta_r H^\circ = +32.9 \text{ kJ/mol}$$

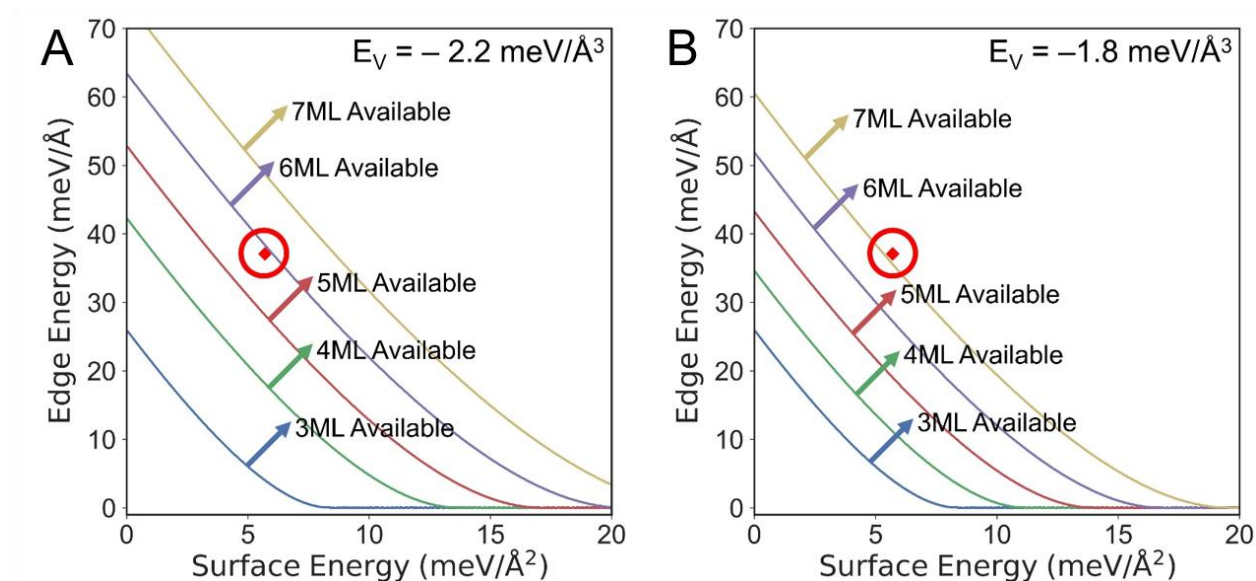


Figure 1.7. (A) A map showing synthesizability of NPLs by edge energy (E_L) and surface energy (E_A) at the volume energy (E_V) of -2.2 meV/Å^3 . Red circle represents the point with E_A of 5.7 meV/Å^2 and E_L of 37.1 meV/Å . Up to 5ML NPLs can form. (B) A map showing synthesizability of NPLs by E_L and E_A at the E_V of -1.8 meV/Å^3 . Red circle represents the point with E_A of 5.7 meV/Å^2 and E_L of 37.1 meV/Å . Up to 7ML NPLs can be synthesized. Adapted with permission from Ref. [19]. Copyright 2018 American Chemical Society.

From the XRF data (Figure 1.8), 1.57 mol of Cl atoms exist per 54.1 mol of Cd atoms in 6ML CdSe NPLs. For every Cl atom is from CdCl₂, among 54.1 mol of Cd atoms in the NPL, (1.57/2) mol of Cd atoms are from CdCl₂, which is 1.45% of the total Cd atoms. Therefore, the average heat of reaction of the NPL formation is $(-94.7 \times 0.9855 + 32.9 \times 0.0145)$ kJ/mol = -92.8 kJ/mol, which is 1.9 kJ/mol higher than the heat of reaction with cadmium acetate. According to the model shown in the Figure 1.7, only 0.4 meV/Å³ change, which equals to 2 kJ/mol for zinc-blende CdSe, is more than sufficient to enable the formation of 6ML CdSe NPLs. A small increase in E_v by incorporating a tiny amount of CdCl₂ (1.9 kJ/mol corresponding to 1.57 mol% of Cl) might be sufficient to change the nucleation barrier (ΔE) and enable formation of 6ML CdSe NPLs.

Analyzed result(FP method)

No.	Layer	Component	Result	Unit	Stat. Err.	LLD	LLQ	Element line	Intensity(cps/μA)
1	1	Film1	227	nm					
2	1	Cd	54.1	mol%	1.45	1.52	4.55	1: Cd-Kα	0.275
3	1	Se	44.4	mol%	0.374	0.0608	0.182	2: Se-Kα	2.213
4	1	Cl	1.57	mol%	0.0110	0.0237	0.0711	3: Cl-Kα	0.728

Spectrum

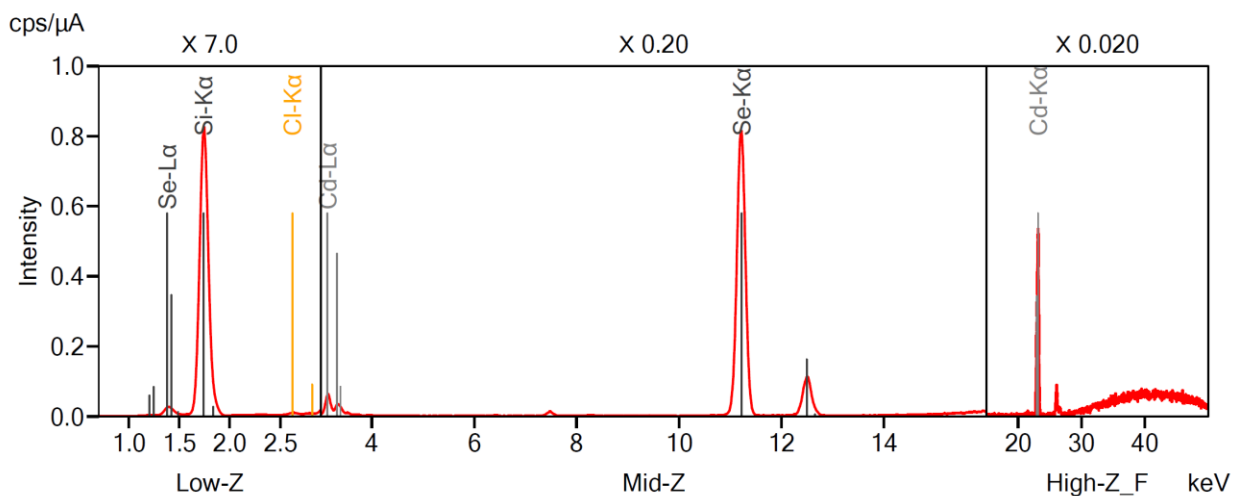


Figure 1.8. X-ray fluorescence (XRF) spectra of 6ML CdSe NPLs and the composition obtained from the fits. Adapted with permission from Ref. [19]. Copyright 2018 American Chemical Society.

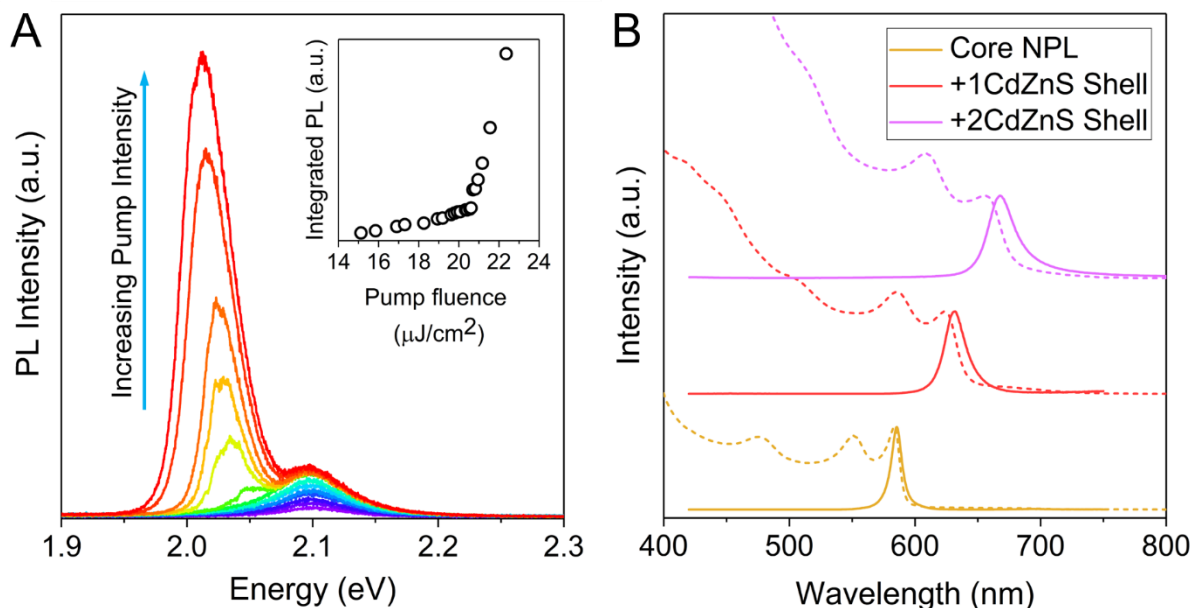


Figure 1.9. (A) PL spectra of ASE measurement. Inset: Integrated PL area vs. pump fluence showing ASE threshold at $21 \mu\text{J}/\text{cm}^2$. (B) Absorption and emission spectra of 6ML CdSe NPL core and nCdZnS/6CdSe/nCdZnS ($n = 1, 2$) core-shell nanoheterostructure. Dotted lines represent absorption spectra, and solid lines illustrate emission spectra. Adapted with permission from Ref. [19]. Copyright 2018 American Chemical Society.

1.5. Applications of 6ML CdSe NPLs

6ML CdSe NPLs can be useful in a number of practical applications. Excitation of a thin film of 6ML CdSe NPLs with 400 nm femtosecond laser pulses was used to study optical gain. 6ML CdSe NPLs showed sharp ASE emission, red-shifted to 616 nm, which can be due to the emission from the bi-exciton state (Figure 1.9 A). The ASE threshold was $21 \mu\text{J}/\text{cm}^2$, which is comparable to other reported thresholds for CdSe NPLs.⁴⁹⁻⁵⁰ The color-pure emission from NPLs is also appealing for lighting and display applications. For displays, PL emission at around 630 nm with narrow linewidth is desirable for red emitters. CdZnS shells could be successfully grown on 6ML CdSe NPL cores using colloidal atomic deposition (c-ALD) (Figure 1.9 B).⁵¹⁻⁵² With the

1ML shell, 1CdZnS/6CdSe/1CdZnS core-shell nanoplatelets achieved red PL emissions centered at 632 nm with a narrow FWHM of 20 nm or 62 meV. Also, no inhomogeneous broadening was found in 2D contour PL emission-excitation maps (Figure 1.10). This example shows that 6ML CdSe NPLs can be a good candidate for red emitters.

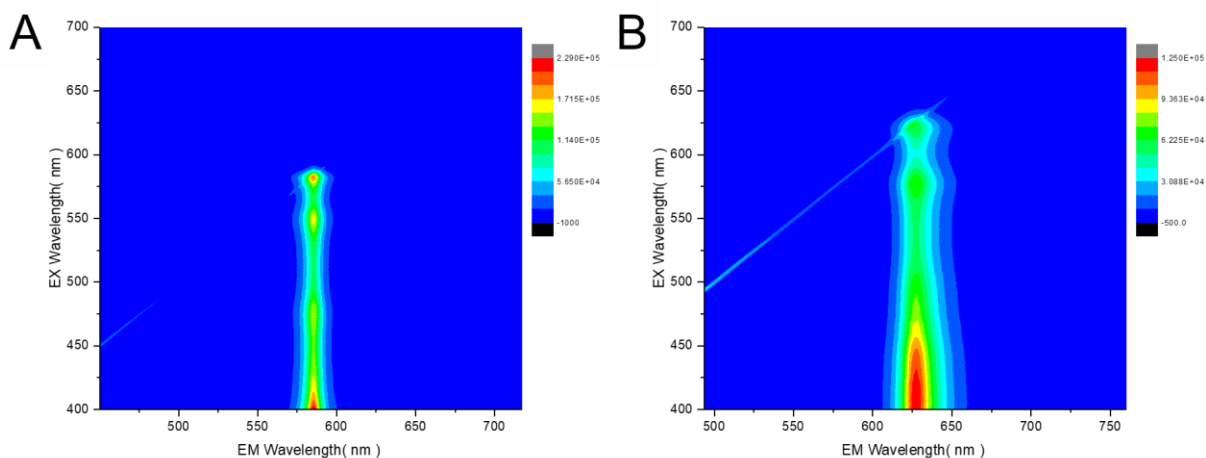


Figure 1.10. 3D contour mapping of PL intensity by excitation and emission wavelengths for (A) 6ML CdSe NPL and (B) 6ML CdSe-CdZnS core-shell structure. Adapted with permission from Ref. [19]. Copyright 2018 American Chemical Society.

1.6. Open Question on Tuning Emission Wavelengths of CdSe NPLs

Though the optimized method to produce 6ML CdSe NPLs uses aqueous cadmium chloride solution which contains both water and chloride, 6ML CdSe NPLs can be synthesized only with water without chloride. Small difference was constantly observed at emission profiles of 6ML CdSe NPLs synthesized with and without chloride ions (Figure 1.11).

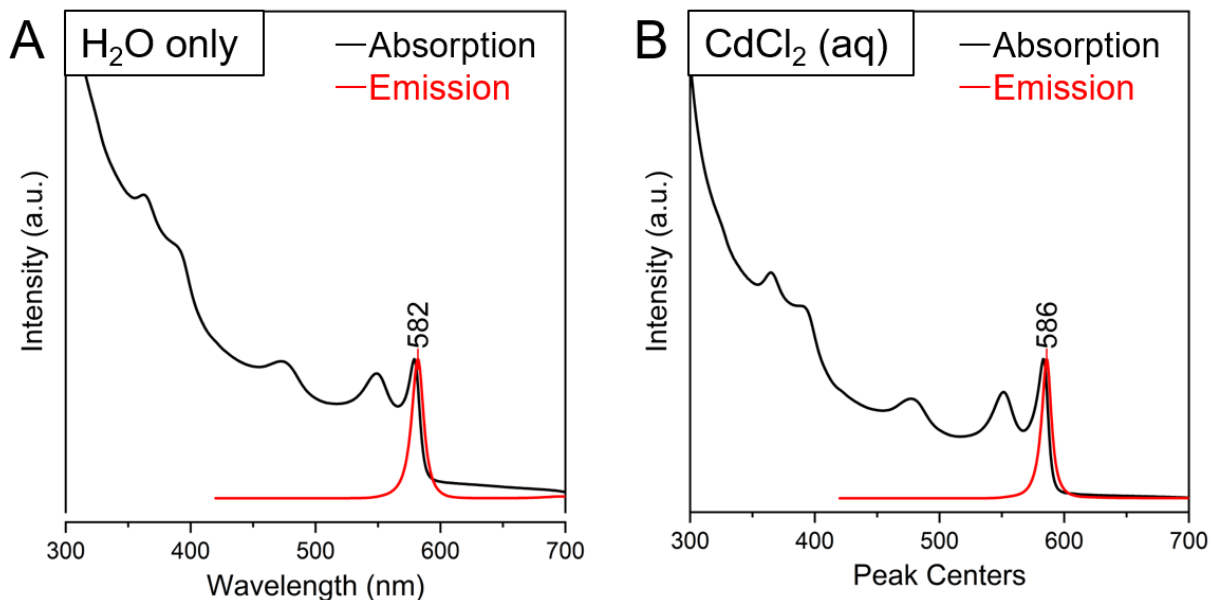


Figure 1.11. Absorption and emission spectra of 6ML CdSe NPLs synthesized (A) without chloride and (B) with chloride ions.

With a simple particle-in-a-box model, emission wavelengths of CdSe NPLs can be fitted to a second-order equation. An energy of emitted light, $E = \frac{hc}{\lambda}$, and this energy is inversely proportional to a square of thickness of NPL, L , according to the one-dimensional (1D) particle-in-a-box model, so $E \propto \frac{1}{L^2}$. Therefore, $L^2 \propto \lambda$. Assuming the thickness of 3ML CdSe NPL is d and each additional monolayer has same thickness, a . Then, for $(3+x)$ ML CdSe NPLs, a wavelength of their emission, $\lambda = b(d + ax)^2$, for a constant, b . By fitting commonly known emission wavelengths, 462 nm for 3ML, 512 nm for 4ML, and 550 nm for 5ML CdSe NPLs, to the equation, emission wavelength of $(3+x)$ ML CdSe NPLs is estimated as $\lambda = -6x^2 + 56x + 462$ in nm (Figure 1.12). It is noticeable that the wavelength of emission of synthesized 6ML CdSe NPL, 586 nm, deviates from the expected value from the fitting, 576 nm.

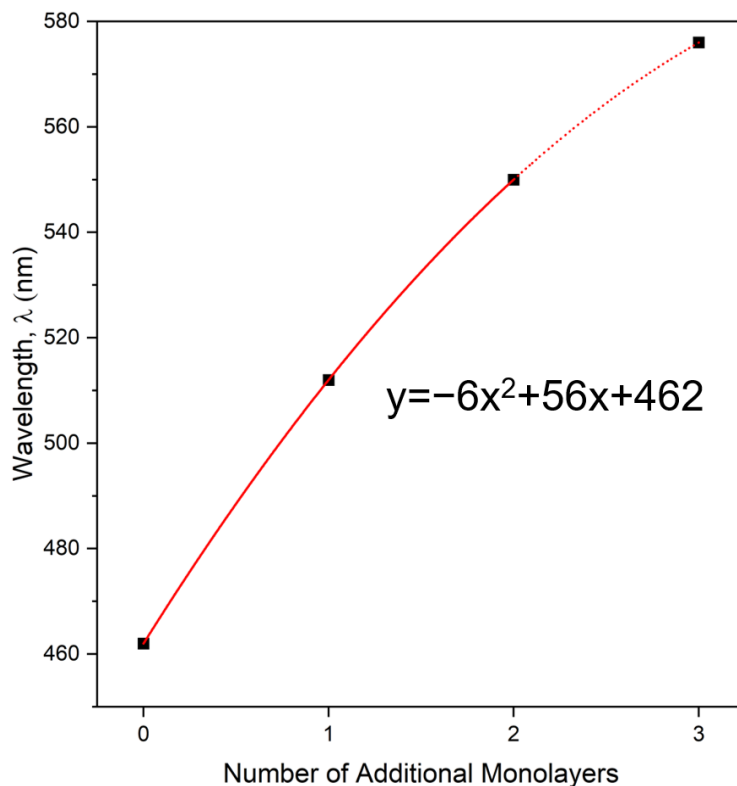


Figure 1.12. The fitting curve of emission wavelengths by the number of additional monolayers to 3ML NPLs.

In 2019, Dufour et al. reported that halide ions can reduce a tensile biaxial strain on the CdSe NPLs, which induces compression of the thickness of the NPLs.⁵³ As biaxial strain is reduced, the thickness of NPLs increases up to the expected value. Similar stress-release effect is expected to be in 6ML CdSe NPLs synthesized with addition of chloride, as about 10% of the surface cadmium is covered with chloride ions. For 6ML CdSe NPLs synthesized only with water, this release of biaxial strain seems to be weaker. This might be due to less incorporation of hydroxide ions onto the CdSe NPL surface, or due to the bulkier nature of a water molecule compared to chloride ions.

In summary, modifying a surface strain can be one of easily achievable ways to fine tune the emission properties of CdSe NPLs. As CdSe NPLs only exist in discrete thicknesses, emission wavelengths of these NPLs have not been continuously tunable like spherical CdSe quantum dots. In addition to doping and alloying of cations and anions, modulating surface strain can provide more opportunities to CdSe NPLs to meet required emission wavelengths for research and device application.

1.7. Summary and Outlook

A synthetic method for 6ML CdSe NPLs was demonstrated. It was confirmed that 6ML CdSe NPLs have characteristics similar to already known CdSe NPLs of other thicknesses. The reason for emergence of 6ML CdSe NPLs upon addition of water and chlorides is not yet fully understood, but we tentatively suggest that change in the nucleation barrier for island formation caused by chlorides may affect the ability to nucleate and grow 6ML CdSe NPLs. We hope this work can help better understand II-VI NPLs, their growth, and applications toward multicolored lasing and next generation displays.

The growth of anisotropic zinc-blende CdSe NPLs is remarkable because zinc-blende is isotropic. Though the exact reason of this growth is not fully understood, it seems a condensed phase such as molten cadmium acetate is a key for anisotropic growth of this cubic CdSe. As shown in this work, this condensed phase can be tuned to have different chemical potentials, and consequently to yield different nanocrystals. Open question here is whether similar growths and control are viable in different material systems, such as InP.

1.8. Experimental Details

1.8.1. Chemicals

Cadmium acetate hydrate ($\geq 99.99\%$, Aldrich), cadmium chloride (99.99% , Aldrich), cadmium formate (MP Biomedicals), cadmium nitrate tetrahydrate (98% , Aldrich), ethanol (200 Proof, Decon), hexanes (99.9% , Fisher), lithium sulfide (98% , Strem), methanol ($\geq 99.9\%$, Fisher), methylcyclohexane (MCH, $\geq 99\%$, anhydrous, Aldrich), myristic acid ($\geq 99\%$, Aldrich), nitric acid ($\geq 69\%$, for trace analysis, Fluka), selenium (99.99% , powder, ~ 100 mesh, Aldrich), 1-octadecene (ODE, 90% , technical grade, Aldrich), oleic acid (OA, 90% , technical grade, Aldrich), oleylamine (OAm, 70% , technical grade, Aldrich), sodium hydroxide ($\geq 98\%$, pellets, anhydrous, Aldrich), toluene ($\geq 99.8\%$, Fisher), zinc acetate (99.98% , anhydrous, Alfa Aesar) were used as received.

1.8.2. Synthesis of Cadmium Myristate¹⁵

In 500mL round-bottom flask, 0.240 g of sodium hydroxide and 1.370 g of myristic acid were fully dissolved in 240 mL of methanol with 1 hour of vigorous stirring. To the reaction flask, with continuous stirring, 0.617 g of cadmium nitrate tetrahydrate dissolved in 40 mL of methanol was added dropwise. White precipitations were vacuum-filtered with fritted glass funnel and washed with methanol five times. White solids were dried under vacuum overnight.

1.8.3. Synthesis of 6ML CdSe NPLs

In 100mL three-neck round-bottom flask, 170 mg of cadmium myristate and 14 mL of ODE was mixed. The mixture was degassed under vacuum at $85\text{ }^{\circ}\text{C}$ for 30 minutes, and then under

nitrogen flow, heated to 250 °C. Then, 12 mg of Se powder well dispersed in 1 mL of ODE with 5-minute sonication was quickly injected (<1 seconds) to the reaction mixture under vigorous stirring. 20 seconds later, 60 mg of cadmium acetate hydrate was added to the reaction flask and the reaction mixture was stirred for another 60 seconds. Then, 0.15 mL of 0.5 M cadmium(II) chloride aqueous solution was slowly introduced to the reaction flask dropwise for 2 minutes. After another 3 minutes, the reaction mixture was rapidly cooled to a room temperature. While the reaction mixture was being cooled down, oleic acid solution containing 2 mL OA and 15 mL of MCH was injected to the reaction flask at ~150 °C. NPLs were first separated from the reaction batch with a centrifugation and dispersed in a smallest amount of MCH. By adding excess amount of hexanes to MCH, smaller quantum dots could be separated by a centrifugation. This step can be repeated to increase purity. Remaining precipitations were dispersed in MCH and heavier particles including 5ML NPLs were removed by size-selective precipitation, which could be a simple centrifugation at high speed followed by removal of a bottom layer. This step also can be repeated for better purity. Overall process was similar for other chloride sources used for Figure 1.5; solutions were added dropwise, and solids were added one-time quickly. In any cases, chloride concentration and total chloride amount were kept same.

1.8.4. General Method for Building CdZnS Shell on CdSe NPL Core⁵¹⁻⁵²

A well-known method of a known colloidal atomic layer deposition (c-ALD) was modified and used for this experiment. For sulfide shell growth, a solution of lithium sulfide was used. Excess amount of sulfide was washed out with ethanol. For building cation layer, sulfide-capped

NPLs were treated with a solution containing both cadmium formate and zinc acetate. OAm was used as a surface ligand. Excess amount of metal precursors were washed out with ethanol.

The shell composition was analyzed with ICP-OES, which revealed that the shell was cadmium rich with Cd to Zn ratio to be 84 to 16.

1.8.5. Characterization Techniques

Transmission electron microscopy (TEM). TEM images were taken with both a 120 kV Tecnai Spirit LaB6 microscope and a 300 kV FEI Tecnai F30 microscope. Samples were prepared by drying diluted NPL solution on Ted Pella carbon-coated copper grids. For face-up images, NPL solution was diluted with MCH, and for stacked images, NPL solution was diluted with MCH and treated with ethanol.

Measurements of optical spectra. Solution samples were prepared by dispersion and dilution in MCH. UV/Vis absorption spectra of solution samples were taken with a Varian Cary 5000 UV-Vis-NIR spectrophotometer from 300 nm to 800 nm. PL and PLE spectra of solution samples were taken with a Horiba Jobin Yvon FluoroMax-4 and FluoroLog-3. Time-resolved PL decay was measured by Horiba Tempro with 405 nm pulsed source.

Powder X-ray diffraction (PXRD). PXRD pattern was obtained with a Bruker D8 with a Cu K α source. Samples were prepared by drop-casting concentrated solution of NPLs on clean glass surfaces.

Raman spectra. Raman spectra were obtained with a Horiba LabRamHR Evolution confocal Raman microscope with a 633 nm light source. Samples were prepared by drop-casting concentrated solution of NPLs on clean glass surfaces.

Inductively coupled plasma optical emission spectrometry (ICP-OES). Core-shell products in solution were precipitated with ethanol and completely dried. The solid was dissolved in concentrated nitric acid and diluted with purified water. This aqueous solution was analyzed with Agilent Technologies 700 Series ICP-OES.

X-ray fluorescence (XRF). XRF was measured with Rigaku NEX DE. Samples were prepared by drop-casting concentrated solution of NPLs on clean Si wafers.

Centrifugation. Centrifugations were mainly done with Eppendorf Centrifuge 5804 R at 11000 rpm (13934 rcf) for 10 minutes. Size-selective precipitations were performed with Eppendorf Minispin at 13400 rpm for 10 minutes.

Amplified spontaneous emission (ASE) measurements. Measurements of ASE were performed using a frequency-doubled Ti: sapphire femtosecond laser at 200 Hz focused on to the sample using a cylindrical lens to form a 2 mm × 170 μm stripe. Stripe emission was collected using a fiber and directed through a monochromator to a Princeton Instruments CCD.

CHAPTER TWO

SYNTHESIS OF COLLOIDAL GALLIUM NITRIDE AND ALUMINUM NITRIDE NANOCRYSTALS IN BIPHASIC MOLTEN SALT / ORGANIC SOLVENT MIXTURES²⁰

Group III nitrides are of great technological importance for electronic devices. These materials have been widely manufactured via high-temperature methods such as physical vapor transport (PVT), chemical vapor deposition (CVD), and hydride vapor phase epitaxy (HVPE). The preparation of group III nitrides by colloidal synthesis methods would provide significant advantages in the form of optical tunability via size and shape control and enable cost reductions through scalable solution-based device integration. Solution syntheses of III-nitride nanocrystals, however, have been scarce, and the quality of the synthesized products has been unsatisfactory for practical use. Here, we report that incorporating a molten salt in a solution synthesis enables crystalline growth of III-nitride nanoparticles. Crystalline gallium nitride and aluminum nitride nanomaterials can be grown in a biphasic molten-salt/organic-solvent mixture under ammonia atmosphere at moderate temperatures and colloidally stabilized by post-synthetic treatment with organic ligands. We suggest that microscopic reversibility in monomer attachment, which is essential for crystalline growth, can be achieved in molten salt media during the nucleation and the growth of the III-nitride nanocrystals. We also show that increased ammonia pressure increases

the size of the gallium nitride nanocrystals produced. This work demonstrates that use of molten salt and high-pressure reactants significantly expands the chemical scope of solution synthesis of inorganic nanomaterials.

2.1. Importance of Colloidal Gallium Nitride and Aluminum Nitride Nanocrystals

Gallium nitride (GaN) is a major semiconductor material for blue light-emitting diodes, lasers, and high-power and high-frequency electronic devices owing to its wide band gap, chemical stability, high breakdown electric field, and high electron saturation velocity.⁵⁴⁻⁵⁶ Aluminum nitride (AlN) is another important group-III nitride material with intriguing properties such as an unusually strong ionicity of chemical bonds, very large absolute free energy of formation, a wide 6.0 eV bandgap, high thermal conductivity, and piezoelectricity.⁵⁶⁻⁵⁸ Owing to these characteristics, AlN is used in optoelectronic devices,⁵⁹⁻⁶⁰ high-power electronics,⁶¹ and microelectromechanical systems.⁶² As AlN and GaN are isostructural, they can form solid solutions (i.e. $\text{Al}_x\text{Ga}_{1-x}\text{N}$), and important heterostructures such as quantum wells have been prepared with this materials system.⁶³

Colloidal semiconductor nanocrystals can demonstrate unique size-dependent optical and electronic properties. In small nanocrystals, the quantum confinement of electron and hole wavefunctions enables fine-tuning of electronic structures via size and shape engineering. Colloidal nanomaterials offer a way to incorporate semiconductors into non-epitaxial thin-film devices (LEDs, displays, light detectors, etc.) using inexpensive solution-based processing and patterning.⁶⁴ Importantly, group III nitrides do not incorporate rare or toxic elements and do not release highly toxic gases upon decomposition, which is rare among III-V and most other semiconductors.

2.2. Developments of Growth Methods for GaN and AlN Crystals

Various methods have been developed to grow GaN and AlN bulk crystals in melts, solutions, fluxes, and supercritical ammonia.^{56,65-75} III-nitride films have been grown on various substrates by vapor phase growth including physical vapor transport (PVT), metal organic chemical vapor deposition (MOCVD), molecular-beam epitaxy (MBE), and hydride vapor phase epitaxy (HVPE).^{56,65-66} GaN and AlN with quasi one-dimensional (1D) structures such as nanorods, nanotubes, or nanocones have been produced through chemical vapor deposition (CVD), MBE, and template-assisted confined growth, and their optoelectronic properties have been examined.⁶⁷⁻⁷³ Thin two-dimensional (2D) GaN crystals have also been synthesized by encapsulated growth within the narrow gap between graphene and silicon carbide (SiC) and by surface-confined nitridation reaction on liquid metal.⁷⁴⁻⁷⁵

Little work has been published on solution synthesis of colloidal GaN and AlN nanomaterials compared to the enormous body of work on II-VI semiconductors or on group III phosphide and arsenide semiconductors. Sardar et al. reported the solvothermal reaction of gallium-cupferron complex, $[\text{Ga}(\text{C}_6\text{H}_5\text{N}_2\text{O}_3)_3]$, or gallium chloride with hexamethyldisilazane in toluene.⁷⁶ Another bimolecular synthesis was recently reported by Choi et al. using gallium stearate and lithium bis(trimethylsilyl)amide in 1-octadecene solvent.⁷⁷ There are also reports on synthetic routes using thermal decomposition of molecular or polymeric precursors. Manz et al. found that molecular gallium azide can thermally decompose in triglyme solvent at 216 °C in 24 hours. Unfortunately, the particles were not sufficiently crystalline to provide X-ray diffraction data.⁷⁸ Mičić et al. reported the synthesis of GaN nanoparticles by pyrolysis of poly(imidogallane).⁷⁹ The method required long reaction times (>48 hours) and produced only a

low yield of colloidal particles. The method was later improved by Pan et al. using dimeric bis(dimethylamido)gallium to produce a higher yield of colloidal particles in a shorter reaction time (24 hours).⁸⁰ All these syntheses produced GaN nanoparticles, but their quality (crystallinity, defects, surface passivation, colloidal stability, size monodispersity) have not been on par with established II-VI (e.g., CdSe), IV-VI (e.g., PbS), and III-V (e.g., InP) quantum dot materials successfully used for device applications.

Reports of solution syntheses of AlN nanoparticles are even more limited. Lan et al. reported an ammonothermal method involving heating Al metal and ammonium chloride at 450 °C for 2 days.⁸¹ Sardar et al. reported a solvothermal reaction of aluminum-cupferron complex or aluminum chloride with hexamethyldisilazane in toluene similar to their GaN synthesis⁷⁶ but at higher temperature of 350 °C or 450 °C.⁸² These two methods produced some AlN nanoparticles but with very limited control over size, shape, and colloidal stability. AlN synthesis at lower temperature (110 °C) was reported by Lu et al. using aluminum chloride and lithium nitride, but the nanoparticles showed crystalline X-ray diffraction patterns only after annealing at 600 °C.⁸³

2.3. Limitations on Solution Synthesis of GaN and AlN Nanocrystals

To date, a traditional colloidal nanoparticle synthesis, via controlled nucleation and growth from molecular precursors in solution phase, has been unable to produce GaN and AlN nanocrystals with structural perfection, size, and shape control comparable to those produced by well-developed methods for preparing, e.g., CdSe, InP, and CsPbBr₃ nanocrystals. This difficulty can be rationalized by taking into account the need for microscopic reversibility of monomer addition during the growth of crystalline particles.⁸⁴ Irreversible formation of chemical bonds

during crystal growth implies that the bonds cannot be efficiently rearranged after they are formed. This inability to disassemble and reorganize incorrectly bonded fragments, which are inevitably formed during crystal growth, prevents formation of perfect crystals, so syntheses lacking microscopic reversibility typically result in highly defective or amorphous products rather than crystalline reaction products. The bond dissociation energies (BDEs) for Ga-N, Al-N, Cd-Se, and In-P bonds are 240 kJ/mol, 268 kJ/mol, 128 kJ/mol, and 198 kJ/mol, respectively.⁸⁵⁻⁸⁶ Since GaN and AlN crystals incorporate much stronger bonds than CdSe or InP crystals, growing crystalline GaN and AlN nanostructures may require higher temperatures or other unusual conditions for achieving reversible bond formation.

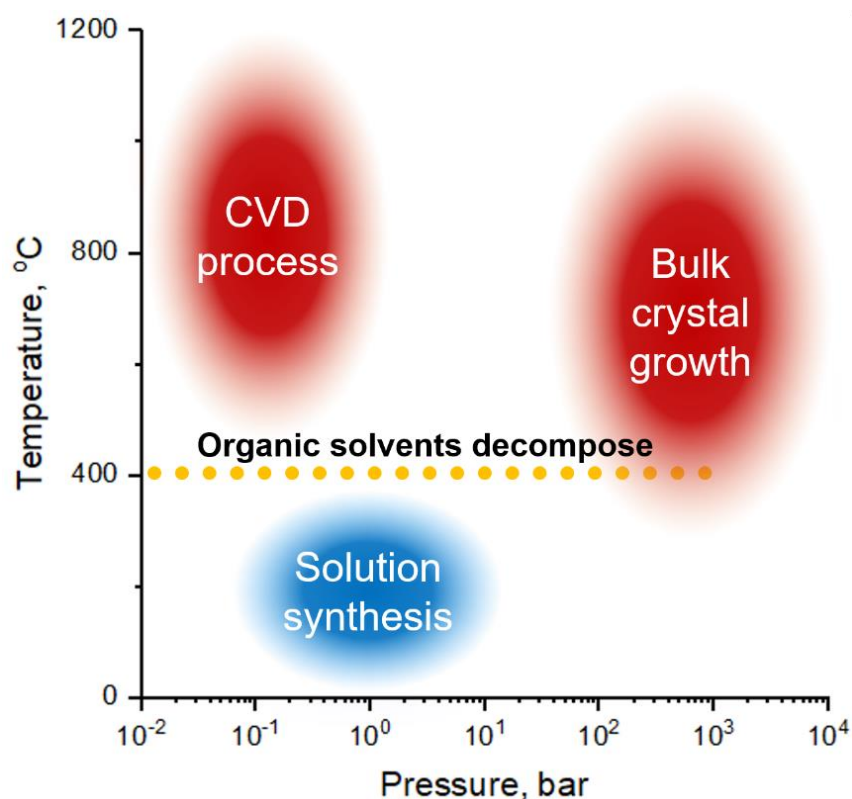


Figure 2.1. The parameter space accessible for traditional solution synthesis compared to the conditions optimized for chemical vapor deposition (CVD) and bulk crystal growth of GaN and AlN crystals and films. Reprinted with permission from Ref. [20]. Copyright 2023 American Chemical Society.

A simple comparison of the optimized conditions for the CVD synthesis of GaN and AlN films, growth of bulk GaN and AlN crystals, and the parameter space accessible for traditional colloidal synthesis (Figure 2.1) suggests that traditional solution synthesis of GaN and AlN nanostructures may be difficult to implement with currently used reaction setups, solvents, and surface ligands. Most CVD processes for GaN and AlN growth happen in the 500-1000 °C temperature range.^{65,73} Other popular growth techniques for bulk GaN and AlN crystals require both high temperature and high pressure; e.g. 350-850 °C and 100-500 MPa have been used in the ammonothermal syntheses.^{56,66} Solution synthesis, however, typically uses high-boiling organic solvents that chemically decompose above 400 °C.⁸⁷ Furthermore, typical laboratory glassware cannot access the pressure range previously identified suitable for growth of high-quality GaN crystals. These limitations suggest that different synthetic approaches are needed to achieve controllable solution synthesis of crystalline III-nitride materials.

2.4. General Considerations for the Solution Synthesis of GaN and AlN

Solution synthesis offers a broad scope of precursors, surface ligands, and additives that can efficiently mediate precursor reactivity through tuning solvent polarity, redox potentials, pH, and other parameters. For colloidal synthesis of compound semiconductors, the metal sources are usually metal cations coordinated with long alkyl-chain ligands (e.g. Cd(oleate)₂, InCl₃-oleylamine complex). The chalcogenide or pnictide precursors are provided as reduced species soluble in non-polar solvents (e.g. tri-*n*-octylphosphine selenide (TOPSe), tris(trimethylsilyl)phosphine [(CH₃)₃Si]₃P). A variety of metal precursors have been studied in solution syntheses of III-V nanocrystals including metal carboxylates and metal halides.^{76-79,88-91} Indium and gallium

carboxylates have been explored extensively for synthesis of III-V nanocrystals resulting in good control over size and size distribution.^{77,88-91} However, we found that higher oxophilicity of Ga(III) species compared to In(III) creates a problem for synthesis of phase-pure GaN nanocrystals. In our studies, gallium precursors containing Ga-O bonds easily introduced oxygen doping of GaN phase during the reaction. For example, the reaction of gallium stearate in trioctylamine solvent with thoroughly dried, oxygen-free ammonia at 290 °C produced gallium oxynitride spinel ($\text{Ga}_{2.81}\text{O}_{3.57}\text{N}_{0.43}$) rather than GaN (Figure 2.2).

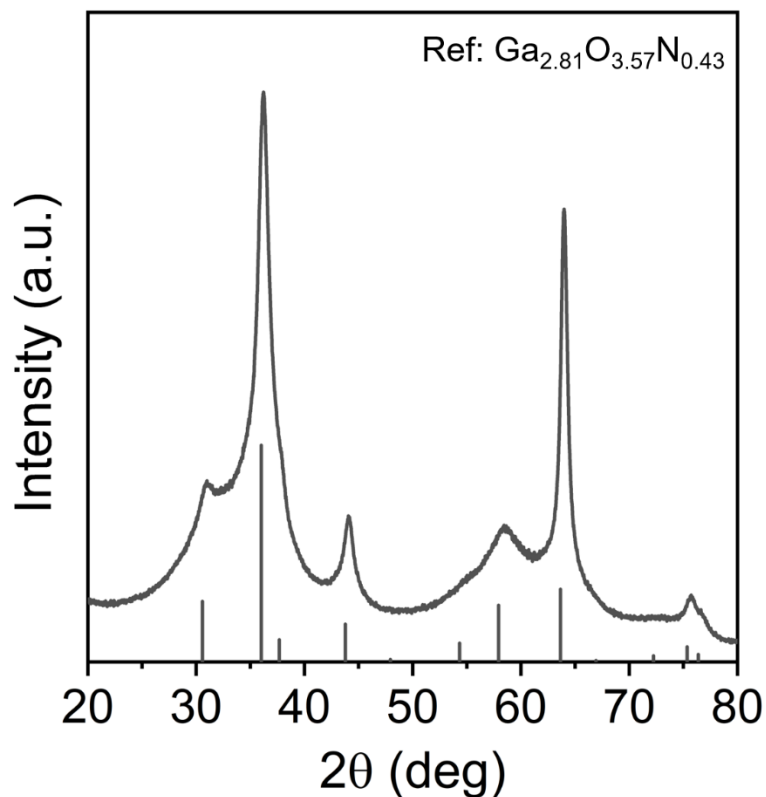


Figure 2.2. PXRD pattern of the product obtained by heating of gallium stearate and ammonia in trioctylamine. The reference pattern is from a previously reported gallium oxynitride spinel.⁹²⁻⁹³ Reprinted with permission from Ref. [20]. Copyright 2023 American Chemical Society.

In fact, a careful inspection of reported powder X-ray diffraction (PXRD) patterns for GaN nanocrystals synthesized from gallium cupferron and stearate precursors⁷⁶⁻⁷⁷ revealed a small peak at $\sim 43^\circ$ 2θ angle (Cu K_α source), which is not present in either wurtzite or zincblende gallium nitride phases but typical for gallium oxynitrides.⁹² From these observations, we suspected that metal precursors used for GaN synthesis should not contain Ga-O bonds. The same is likely to be true for aluminum, as aluminum makes an even stronger bond with oxygen than gallium (BDE for Ga-O is 374 kJ/mol, while for Al-O it is 502 kJ/mol).⁸⁵ Therefore, to avoid inclusion of oxygen impurities in GaN and AlN nanostructures, we used oxygen-free precursors, solvents, and other components of the reaction mixture.

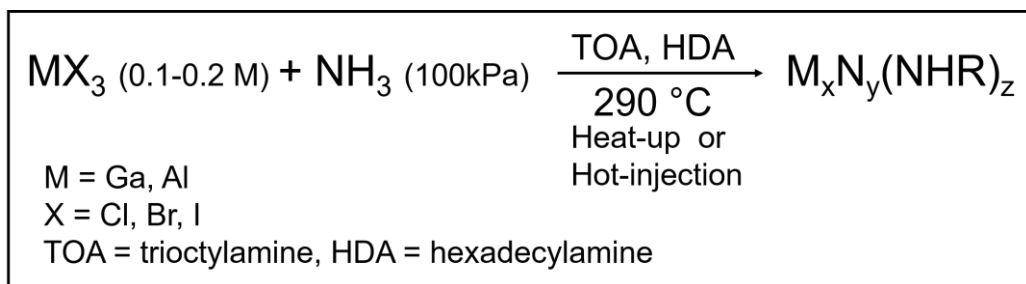


Figure 2.3. A reaction scheme for reactions of 0.1-0.2 M gallium and aluminum halides with NH_3 at 290°C in trioctylamine/hexadecylamine (TOA/HDA) solution. Adapted with permission from Ref. [20]. Copyright 2023 American Chemical Society.

Oxygen-free conditions can be realized by using metal halides, ammonia, and amines. These precursors have been successfully used for CVD synthesis of III-nitride materials.⁶⁵ We studied the products of reactions between MX_3 (M=Ga, Al; X= Cl, Br, I) and NH_3 in alkylamine solvent (Figure 2.3). In a heat-up approach, 0.1 M or 0.2 M solutions of MX_3 in 4 mL of freshly distilled trioctylamine (TOA) and 0.6 g of hexadecylamine (HDA) were heated from room temperature to 290°C under a constant flow of ammonia. Alternatively, in a hot-injection approach,

the MX_3 solution was pre-heated to 290 °C under dry nitrogen atmosphere, followed by the addition of flowing ammonia through the reaction flask for 5 minutes. The reaction mixture was kept at 290 °C for one hour before cooling to room temperature. As-synthesized products in both approaches were non-colloidal at room temperature and could be separated from solution with centrifugation. The resulting white solids were washed with toluene to remove the remaining alkylamines and then with methanol to remove ammonium halides, a major byproduct of these reactions.

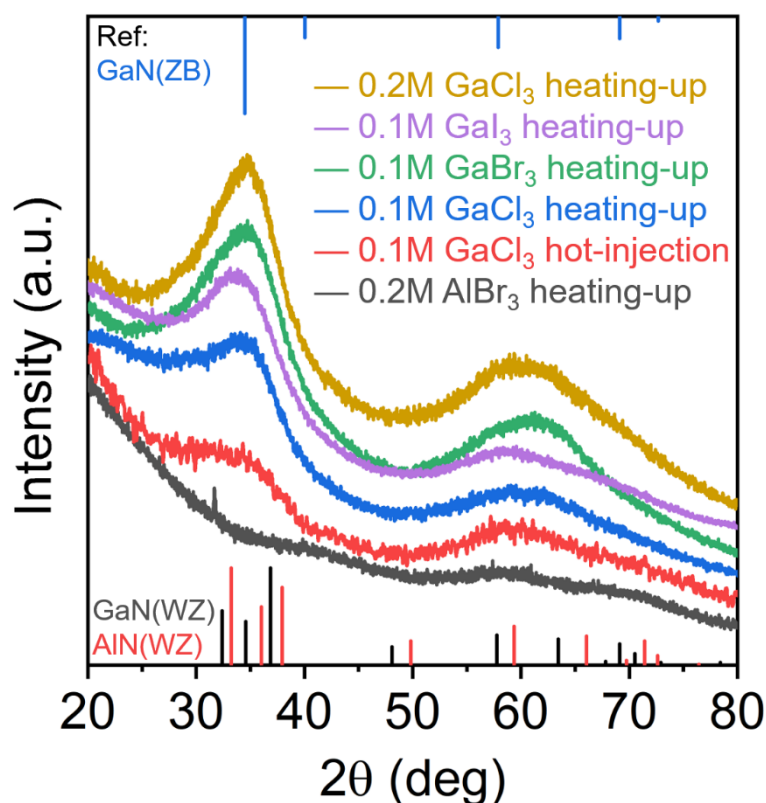


Figure 2.4. PXRD patterns measured from the products of the reactions of 0.1-0.2 M gallium halide or aluminum halide with excess NH_3 in TOA/HDA solution. The vertical lines show the positions and relative intensities for bulk zinc-blende (ZB, blue vertical lines) GaN, wurtzite (WZ, black vertical lines) GaN, and wurtzite (WZ, red vertical lines) AlN phases. Reprinted with permission from Ref. [20]. Copyright 2023 American Chemical Society.

All the reaction products of GaX_3 precursors showed similar PXRD patterns with two broad features around 35° and 60° 2θ angles. No obvious diffraction peaks were present in the PXRD pattern of a product of the reaction between ammonia and AlBr_3 , implying formation of an amorphous material (Figure 2.4). To better understand the nature of the reaction products, we carried out X-ray atomic pair distribution function (PDF) analysis of the products formed by reacting 0.1 M or 0.2 M MX_3 ($\text{M}=\text{Ga}, \text{Al}$; $\text{X}=\text{Cl}, \text{Br}, \text{I}$) solutions with excess NH_3 . Figure 2.5 shows the pair distribution functions, $G(r)$, for the “GaN” and “AlN” reaction products. We compared our experimental data with the simulated $G(r)$ from GaN and AlN nanocrystals. For the $\text{GaCl}_3+\text{NH}_3$ reaction products, the interatomic distances for the first two $G(r)$ peaks are close to the positions expected for crystalline GaN, but the peaks at larger distances significantly deviate from the interatomic distances in a GaN crystal (Figure 2.5 A). The first $G(r)$ peak reflects Ga-N bonds, which is slightly shorter (1.90 \AA) than the expected distance in GaN crystals (1.95 \AA). The second $G(r)$ peak reflects the nearest Ga \cdots Ga distances, and these distances match well to the expected value in GaN crystals, which implies that Ga-N-Ga bond angles are close to 109.5° expected for tetrahedral coordination. The second peak splits into two components, suggestive of two distinct bonding motifs. Moreover, the ratio of intensities for the first two $G(r)$ peaks corresponding to Ga-N and Ga \cdots Ga distances in our reaction product is significantly larger than that ratio for crystalline GaN. This discrepancy suggests that many nitrogen atoms forming Ga-N bonds do not participate in the bridging Ga-N-Ga bonding. A shorter Ga-N bond length, broader features from Ga \cdots Ga correlations, and suppressed intensities for the peaks from longer-distance atomic pairs are predicted to be the characteristics of amorphous GaN.⁹⁴ Taken together, our PDF analysis concludes that the $\text{GaCl}_3+\text{NH}_3$ reaction product is an amorphous material consisting of

distorted tetrahedral structures with numerous Ga vacancies, which only locally resembles the tetrahedrally coordinated crystalline phase.

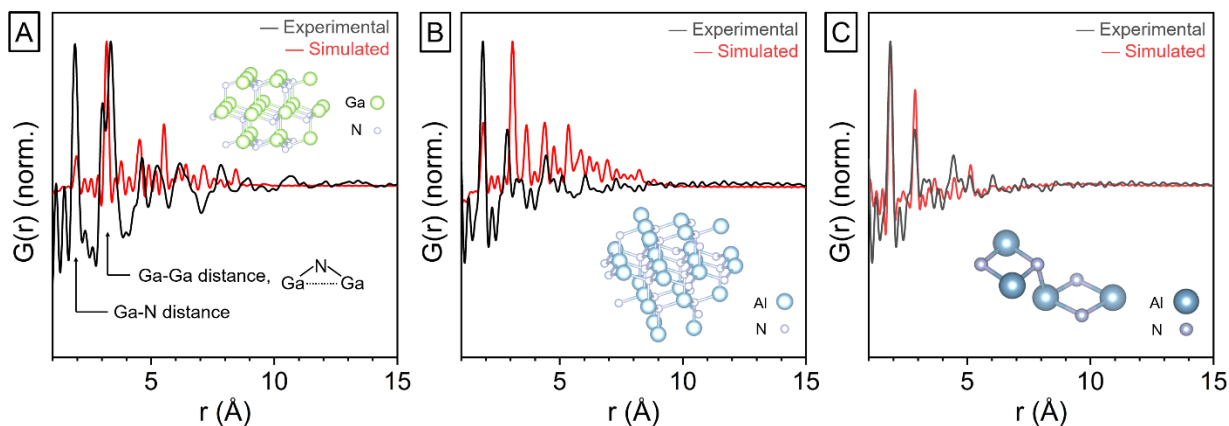


Figure 2.5. (A) The atomic pair distribution function (PDF) measured for the products of the reaction between 0.2 M GaCl_3 and excess NH_3 in TOA/HDA solution. The experimental data (black line) are compared with the simulated PDF (red line) of a 1-nm-diameter wurtzite GaN nanocrystal (inset cartoon). (B, C) PDFs of the product of the reaction between 0.1 M AlBr_3 and excess NH_3 in TOA/HDA solution. Inset figures represent the structures used for simulations. The experimental data (black line) are compared with the simulated PDFs (red line) of a 1-nm-diameter spherical WZ AlN crystal (B) and a molecular 4-membered-ring AlN structure (C). Adapted with permission from Ref. [20]. Copyright 2023 American Chemical Society.

Based on the PDF analysis, the $\text{AlBr}_3+\text{NH}_3$ reaction product has a totally different structure than its gallium counterpart. Except for the first peak (Al-N bonds, ~ 1.90 Å), all other $G(r)$ features significantly deviate from those expected for AlN crystals (Figure 2.5 B). The $\text{AlBr}_3+\text{NH}_3$ reaction did not yield a product adopting any motif of the wurtzite (WZ) or zinc blende (ZB) structures. The second $G(r)$ peak, corresponding to the nearest $\text{Al}\cdots\text{Al}$ distance (2.87 Å), significantly deviates from the $\text{Al}\cdots\text{Al}$ distance in WZ or ZB AlN (3.08 Å). A rapid decay of $G(r)$ amplitude also suggests formation of small molecular fragments with no long-range correlations. We suggest that experimental $G(r)$ data can best be described as polymeric structures incorporating Al_2N_2 four-membered rings. There are numerous prior reports of small molecules and short chains with an Al-

$(\mu_2\text{-NR})_2\text{-Al}$ four-membered ring structural motif.⁹⁵ The Al-N-Al bond angle calculated from the positions of first two $G(r)$ peaks is also consistent with this assignment (Figure 2.5 C).

The non-crystalline nature of MX_3+NH_3 reaction products can result from the irreversible binding of metal and nitrogen containing fragments with no subsequent rearrangements of subunits. In contrast, the formation of GaN and AlN crystals requires microscopically reversible binding of the atomic building blocks.⁸⁴ Traditional CVD synthesis of III-nitrides approaches microscopic reversibility of GaN and AlN growth by using high temperatures. Unfortunately, solution methods do not permit arbitrarily increasing reaction temperature due to solvent decomposition. This may be one reason why, despite the great success of CVD-grown nitride semiconductors, there has only been limited progress with solution synthesis of GaN and AlN nanomaterials.

2.5. Formation of GaN and AlN Nanocrystals in Solution

We found that crystalline GaN and AlN nanostructures could be synthesized if the reaction between Ga or Al halides and ammonia was carried out in the reaction mixture containing higher concentrations of metal halide precursors, nominally exceeding 1 M GaX_3 or AlX_3 in TOA and HDA (Figure 2.6). In a typical synthesis, 5 mmol of finely ground anhydrous metal halide salt was mixed with 4 mL of TOA and 0.6 g of HDA, and then ammonia was passed over the mixture at room temperature, followed by heating to 290 °C. The reaction mixture was held at 290 °C for one hour and then cooled down to room temperature. The resulting III-nitride particles were not colloidal at this stage and were collected with centrifugation. The solid was washed first with toluene and then methanol to remove excess alkylamines and ammonium halide, respectively. The nanoparticles could then be colloiddally stabilized in an *n*-hexane or toluene solution of oleylamine

and oleic acid (10 % v/v each) after brief sonication. The remaining non-colloidal part was removed by centrifugation, and nanoparticles in the supernatant were flocculated with ethanol followed by dispersion in fresh *n*-hexane or methylcyclohexane to form a colloidal solution (Figure 2.7). The entire process of synthesis and purification was conducted under an inert atmosphere; this is necessary during synthesis to avoid oxygen inclusion and is highly recommended during purification, as the III-nitride particles slowly lose their colloidal stability upon exposure to air.

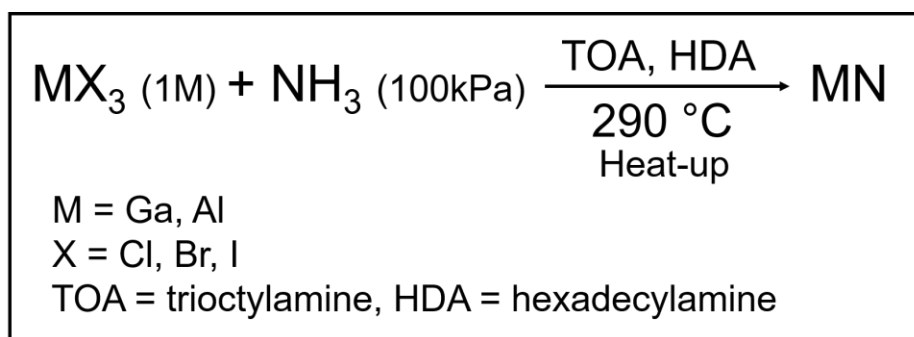


Figure 2.6. A reaction scheme for reactions of 1 M gallium and aluminum halides with NH_3 at 290 °C in trioctylamine/hexadecylamine (TOA/HDA) solution yielding crystalline phases. Adapted with permission from Ref. [20]. Copyright 2023 American Chemical Society.

Gallium chloride and gallium bromide precursors yielded highly anisotropic WZ-phase GaN nanostructures, grown along the [0001] crystallographic direction, which included nanotetrapods and nanorods (Figures 2.8 A, 2.9 A-B). Their PXRD patterns showed sharp (0002) peaks in agreement with simulated X-ray diffraction patterns for nanorods of WZ GaN phase (Figures 2.8 A-B). TEM images indicated that the products from reactions using gallium chloride had a higher proportion of nanotetrapods than those from gallium bromide reactions (Figures 2.9 A-B). TEM images also revealed that the product from gallium bromide reactions had tiny spherical nanocrystals, which were not noticeable in PXRD patterns, mixed with the nanorods.

When gallium iodide was used as the precursor, spherical ZB-phase GaN nanocrystals formed instead of WZ GaN nanorods (Figures 2.8 A, 2.9 C). The Scherrer grain size of the spherical ZB GaN particles was about 4 nm, and the PXRD pattern matched well with the simulated pattern (Figures 2.8 A,C).



Figure 2.7. Photographs of a colloidal solution of GaN nanoparticles under ambient light (left) and under illumination with 302 nm ultraviolet (UV) light (right). Under UV, the solution glows yellow due to emissions from midgap states. Adapted with permission from Ref. [20]. Copyright 2023 American Chemical Society.

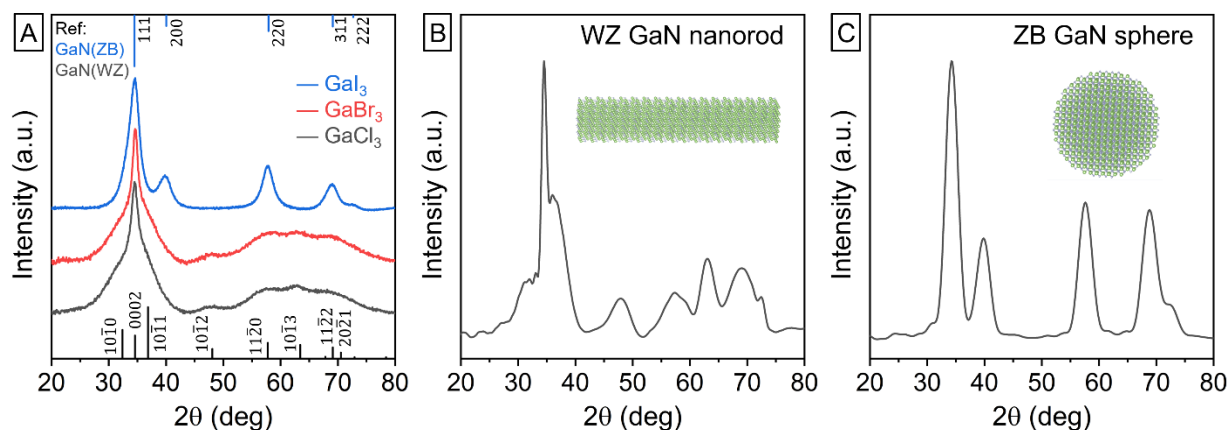


Figure 2.8. PXRD patterns from synthesized GaN nanocrystals and simulated GaN nanocrystals. (A) PXRD patterns of GaN nanocrystals synthesized by reacting NH_3 with GaCl_3 (black curve), GaBr_3 (red curve), and GaI_3 (blue curve) with reference lines from wurtzite (WZ, black vertical lines) and zinc blende (ZB, blue vertical lines) bulk GaN phases. (B) A PXRD pattern of a simulated WZ GaN nanorod with 2-nm diameter and 9-nm length. (C) A PXRD pattern of a simulated spherical ZB GaN nanocrystal with 4-nm diameter. Adapted with permission from Ref. [20]. Copyright 2023 American Chemical Society.

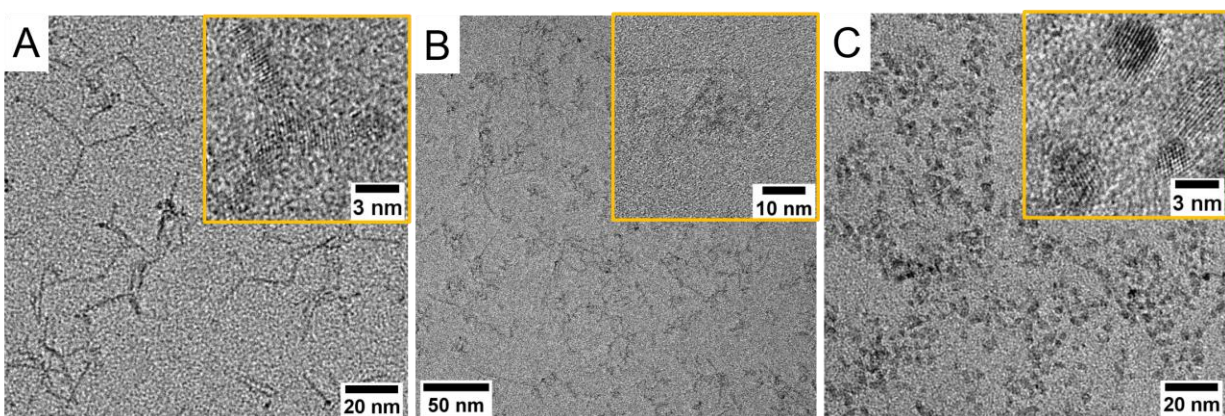


Figure 2.9. TEM images from synthesized GaN nanocrystals. Insets show high-resolution TEM images (A) A TEM image of WZ GaN nanorods and nanotetrapods synthesized using GaCl_3 . (B) A TEM image of WZ GaN nanorods synthesized using GaBr_3 . The image also shows spherical particles. (C) A TEM image of ZB GaN nanocrystals synthesized using GaI_3 . Adapted with permission from Ref. [20]. Copyright 2023 American Chemical Society.

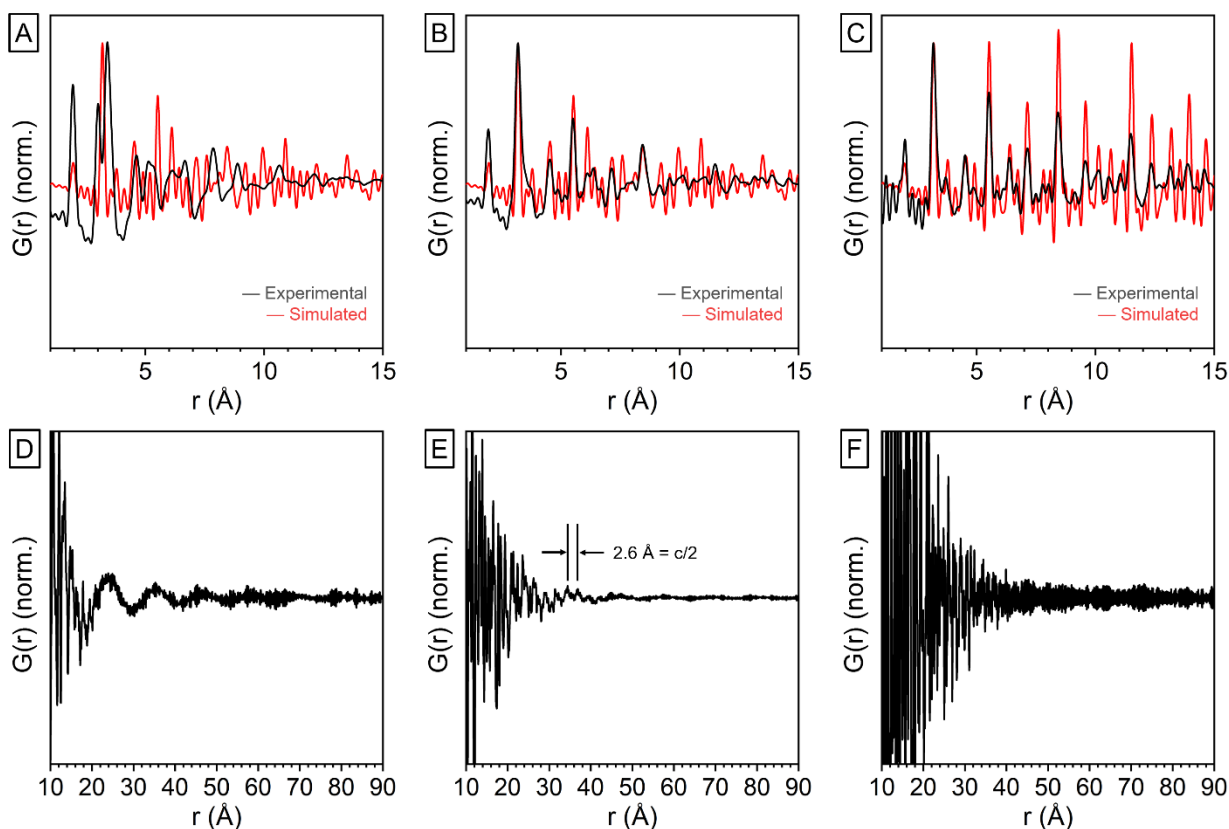


Figure 2.10. PDFs from GaN nanocrystals synthesized with GaCl_3 (A, D), GaBr_3 (B, E), and GaI_3 (C, F) under ambient-pressure ammonia. The long-wavelength damped sine waves observed in (D) and, to a lesser extent, (E) are often present in experimental PDF data. These can originate from an imperfectly corrected background.⁹⁶ Reprinted with permission from Ref. [20]. Copyright 2023 American Chemical Society.

X-ray PDF analysis of the nanocrystalline reaction products was also performed for direct comparison with the amorphous GaN products (Figure 2.10). The importance of combined PXRD and PDF studies can be highlighted on the examples of the reaction products of 1 M GaCl_3 and GaBr_3 with NH_3 . The reaction products for both reactions showed similar PXRD patterns (Figure 2.8 A), but PDF data revealed that GaCl_3 reaction product contained significant amounts of amorphous byproducts, similar to what was discussed in the previous section (Figures 2.5 A, 2.10 A). PDFs of products from gallium bromide and gallium iodide reactions match well with expected

patterns from simulated nanocrystalline GaN in WZ and ZB phases, respectively (Figures 2.10 B-C). It is notable that PDFs of GaN nanocrystals from gallium bromide showed periodic correlations up to 5 nm interatomic distance (Figure 2.10 E). The correlation has a period of 0.26 nm, which is the distance between [0002] planes of WZ-GaN crystal, hinting that nanocrystals grew anisotropically along the [0001] direction, in agreement with the narrow (0002) PXRD peak.

The reaction of 1 M AlBr_3 with NH_3 also produced WZ AlN nanorods grown along the [0001] direction, showing a sharp (0002) peak in PXRD, in line with the patterns observed for GaN nanorods (Figure 2.11). To the best of our knowledge, this is the first example of colloidal crystalline AlN nanoparticles synthesized in solution. Unfortunately, the yield of AlN nanorods versus amorphous AlN byproducts varied from run to run, and the conditions for synthesis of AlN nanocrystals of various sizes and shapes are yet to be optimized.

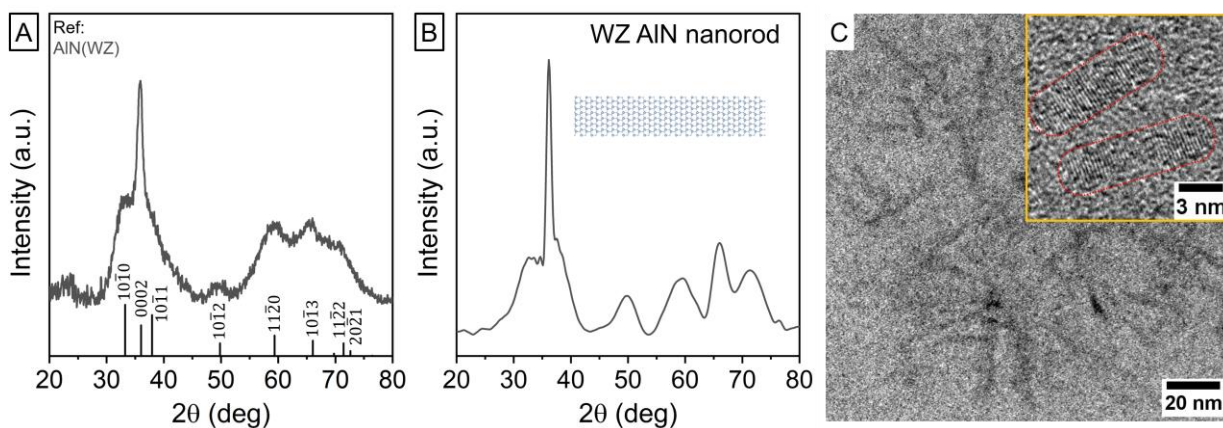


Figure 2.11. (A) A PXRD pattern of AlN nanorods synthesized from AlBr_3 (black curve) with reference lines from WZ AlN phase (vertical lines). (B) A PXRD pattern of a simulated WZ AlN nanorod with 2-nm diameter and 9-nm length. (C) A TEM image of AlN nanorods. The inset shows a high-resolution TEM image. AlN nanorods are marked with dotted red lines. Adapted with permission from Ref. [20]. Copyright 2023 American Chemical Society.

2.6. Formation of GaN Nanocrystals from a Biphasic Mixture

The formation of crystalline GaN and AlN particles is counterintuitive because using the same MX_3 and NH_3 precursors yielded amorphous products when the halide salt was present at lower concentrations (cf. Figures 2.3-2.5). A careful inspection of the reaction conditions showed that the most notable difference among the experimental runs producing crystalline versus amorphous products was homogeneity of the reaction mixture. Crystalline particles formed when we used large amounts of GaX_3 or AlX_3 salts and when the halide salts were not fully dissolved in TOA/HDA solvent before the reaction started. Due to low melting points of gallium and aluminum halides (77.9 °C for GaCl_3 , 121.5 °C for GaBr_3 , 212 °C for GaI_3 , and 97.5 °C for AlBr_3), the reaction mixtures contained a molten inorganic salt phase immiscible with the organic phase. This molten salt phase likely plays an important role in the formation of crystalline GaN and AlN phases, as discussed below.

The reaction between GaX_3 and NH_3 generated fine white solids of ammonium halide and III-nitride products that obscured direct observation of molten gallium halide droplets during the reaction. Therefore, we aimed to determine whether this inhomogeneity was indeed required for the synthesis of crystalline particles or crystallization was simply induced by an increased salt concentration. While gallium chloride is soluble in the mixture of TOA and HDA at high temperature, potassium tetrachlorogallate (KGaCl_4) remains phase-separated from TOA/HDA mixtures at 250 °C, which is above the melting point of KGaCl_4 (Figure 2.12). Hot injection of excess ammonia into a homogeneous solution containing 1 mmol of GaCl_3 in 4 mL of TOA and 0.6 g of HDA pre-heated to 290 °C resulted in amorphous reaction products (Figure 2.13). The hot injection of excess ammonia into a biphasic mixture of 1 mmol of KGaCl_4 , 4 mL of TOA, and 0.6 g of HDA at 290 °C resulted in a qualitatively different reaction product (Figure 2.13). A

homogeneous solution of gallium chloride generated only amorphous species, similar to those described in Figure 2.4, while the biphasic mixture of KGaCl_4 produced crystalline WZ-GaN nanorods. Therefore, it appears plausible that the molten salt phase is required to generate crystalline III-nitride nanomaterials.

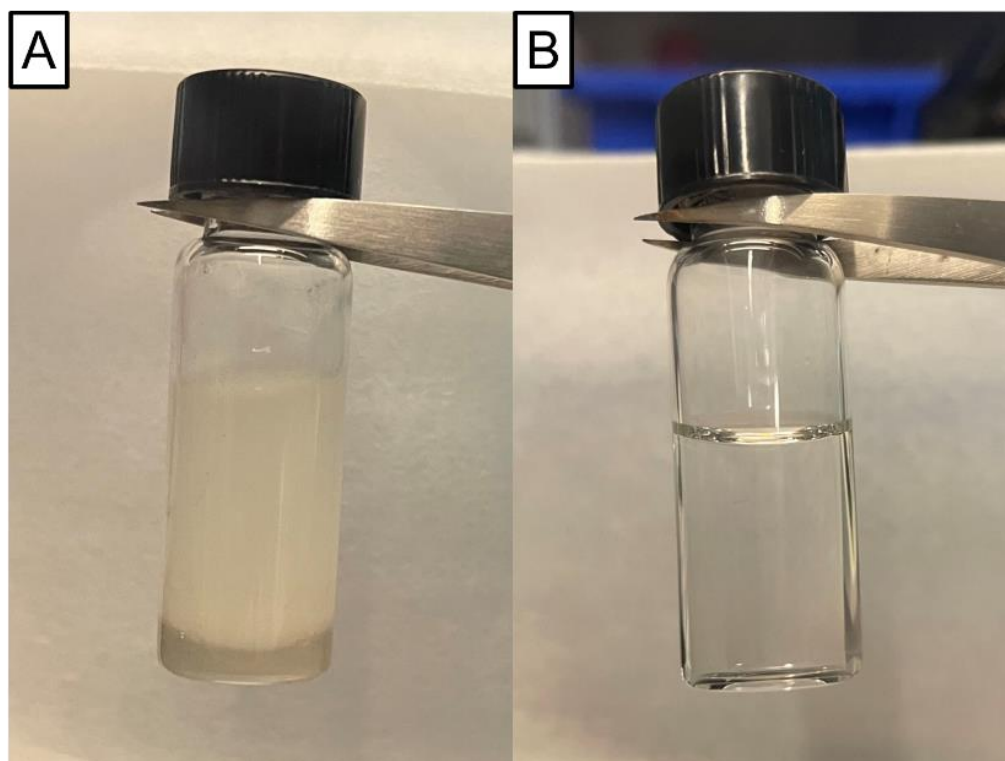


Figure 2.12. Photographs of hot mixtures of gallium salts and alkylamines. (A) A mixture of 0.5 mmol KGaCl_4 , 2 mL of TOA, and 0.3 g of HDA at elevated temperatures (250 °C). (B) A mixture of 0.5 mmol GaCl_3 , 2 mL of TOA, and 0.3 g of HDA at elevated temperatures (250 °C). The KGaCl_4 mixture had a clear separation between an upper organic phase with a white emulsion and a lower, clear molten salt phase. The GaCl_3 mixture became a clear homogeneous solution. Reprinted with permission from Ref. [20]. Copyright 2023 American Chemical Society.

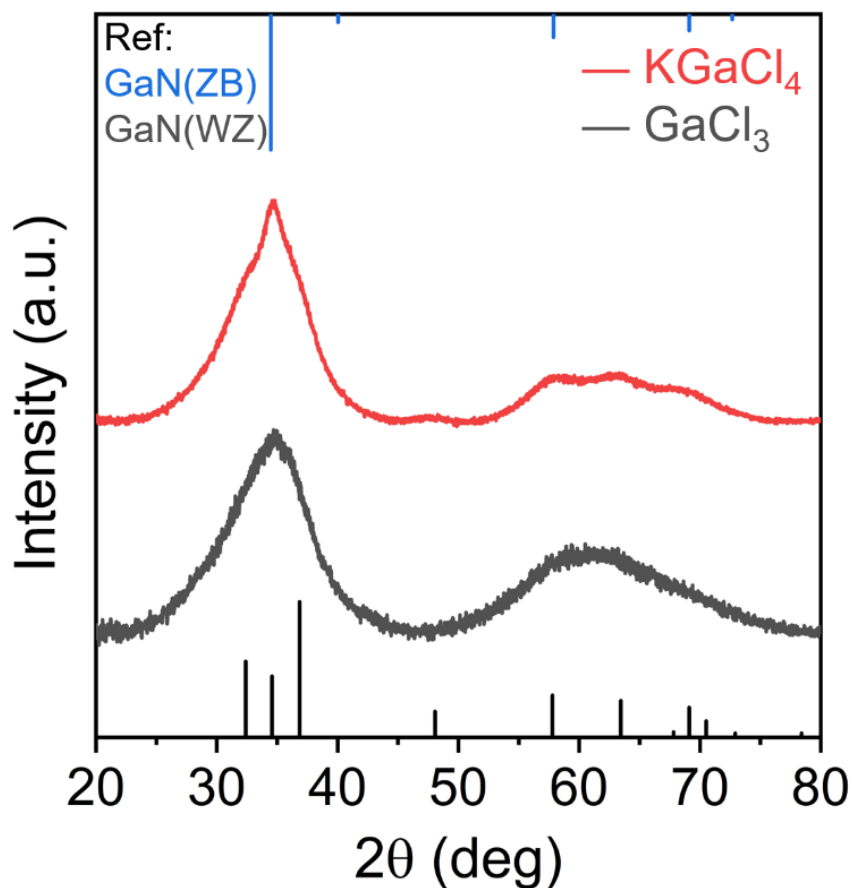


Figure 2.13. PXRD patterns obtained from the products of hot-injection approaches with mixtures of 1 mmol of gallium salt (KGaCl₄ or GaCl₃), 4 mL of TOA, and 0.6 g of HDA. Reprinted with permission from Ref. [20]. Copyright 2023 American Chemical Society.

2.7. Nanocrystal Growths in a Molten Salt Phase

As described previously, microscopic reversibility during nucleation and growth is essential to generate crystalline particles. Figure 2.14 schematically illustrates monomer additions to a growing nanoparticle in different material systems. In a synthesis of II-VI (e.g., CdSe) nanocrystals, monomer additions are reversible due to relatively small chemical bond energy, and, therefore, the growth of a crystalline phase can occur at relatively low temperatures via reversible

addition of atoms (Figure 2.14 A). Unlike II-VI semiconductors, GaN and AlN have strong bonds which impede efficient formation of crystalline products in organic solution (Figure 2.14 B). However, our results suggest that the presence of molten salts in the reaction mixture can restore the microscopic reversibility during nucleation and growth (Figure 2.14 C).

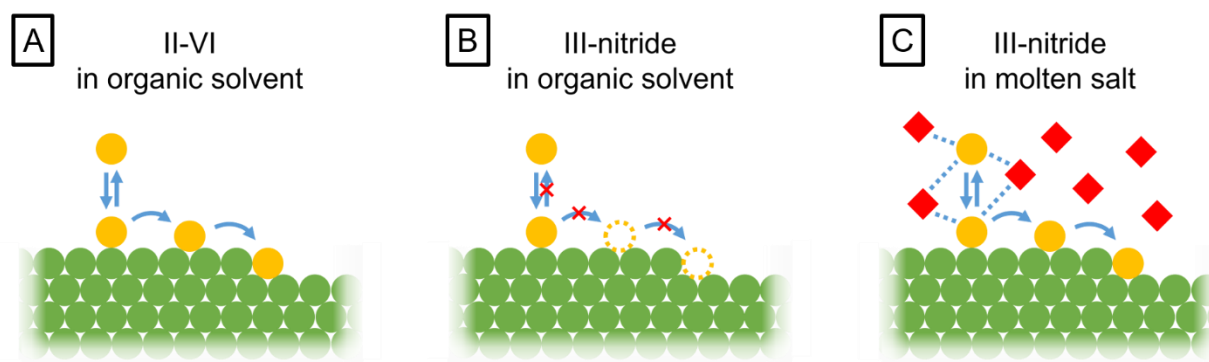


Figure 2.14. Cartoons depicting microscopic reversibility during synthesis of II-VI and III-nitride nanocrystals. Yellow circles represent monomers of the corresponding system, and red squares illustrate ions in molten salts. Adapted with permission from Ref. [20]. Copyright 2023 American Chemical Society.

Establishing microscopic mechanism to explain the effect of molten salt on GaN and AlN nanocrystal synthesis requires further investigation. We suggest that the molten salt environment facilitates monomer detachment by efficiently stabilizing charged species. Figure 2.15 schematically depicts possible pathways for surface atom detachment with cleavage of Ga-N bonds. For a typical ZB or WZ III-V nanocrystal terminated with thermodynamically stable low-index facets, surface metal atoms can be bonded to two X-type ligands, which can be represented as Z-type GaX_2 fragment.⁹⁷⁻⁹⁸ In non-polar organic solvents, charged species are energetically unfavorable and chemical species typically remain charge-neutral. A detachment of the surface Ga atom likely proceeds via L-promoted Z-type ligand displacement⁹⁷ where nucleophilic L-type

ligand (alkylamine) binds to the surface Ga atom and weakens its bonding with the crystal lattice (Figure 2.15 A). Such cleavage generates charged species, and the energy of the system is greatly increased. However, in a highly polarizable molten salt environment, charged species are present in large quantities. The removal of a Z-type GaX_2 group can be promoted by an X-type anion, followed by a proton transfer from an ammonium ion to negatively charged surface nitrogen site (Figure 2.15 B). This process, nominally X-promoted Z-type ligand displacement, does not produce any highly unstable charged nor under-coordinated reaction products, and the energy change of the system is moderate. The detachment of misbound surface atoms can therefore occur more efficiently in molten salts compared to non-polar organic solvents, which are typically used for nanocrystal synthesis.

There are considerable precedents that molten salt phases encourage the formation of crystalline phases at lower temperatures in flux-based solid state synthesis.⁹⁹⁻¹⁰⁰ Also, the presence of molten salt byproducts in solid state metathesis reactions is suspected to be important for obtaining crystalline materials.¹⁰¹⁻¹⁰² In colloidal nanocrystal synthesis, there are experimental and computational evidences that molten salt droplets of cadmium acetate can serve as the nucleation and growth media during synthesis of two-dimensional ZB CdS, CdSe, or CdTe nanoplatelets.²¹ High concentrations of the reagents in molten salt result in reaction-rate-controlled rather than diffusion-controlled kinetics of nucleation and growth.²¹ The same argument may explain the formation of anisotropic WZ III-nitride nanocrystals, because one-dimensional nanorods and two-dimensional nanoplatelets can form through very similar reaction-rate-limited pathway.¹⁰³ It has been also reported that high monomer concentration causes WZ CdSe particles to become rods rather than spheres.¹⁶ However, the monomer concentration alone cannot explain the formation of spherical ZB GaN nanocrystals. The effect of halide ions on surface energy of different nanocrystal

facets may be an alternative explanation for the shape and phase of our reaction products. It has been shown that different halide additives can affect the shapes and the phases of nanocrystals for other systems.¹⁰⁴⁻¹⁰⁶

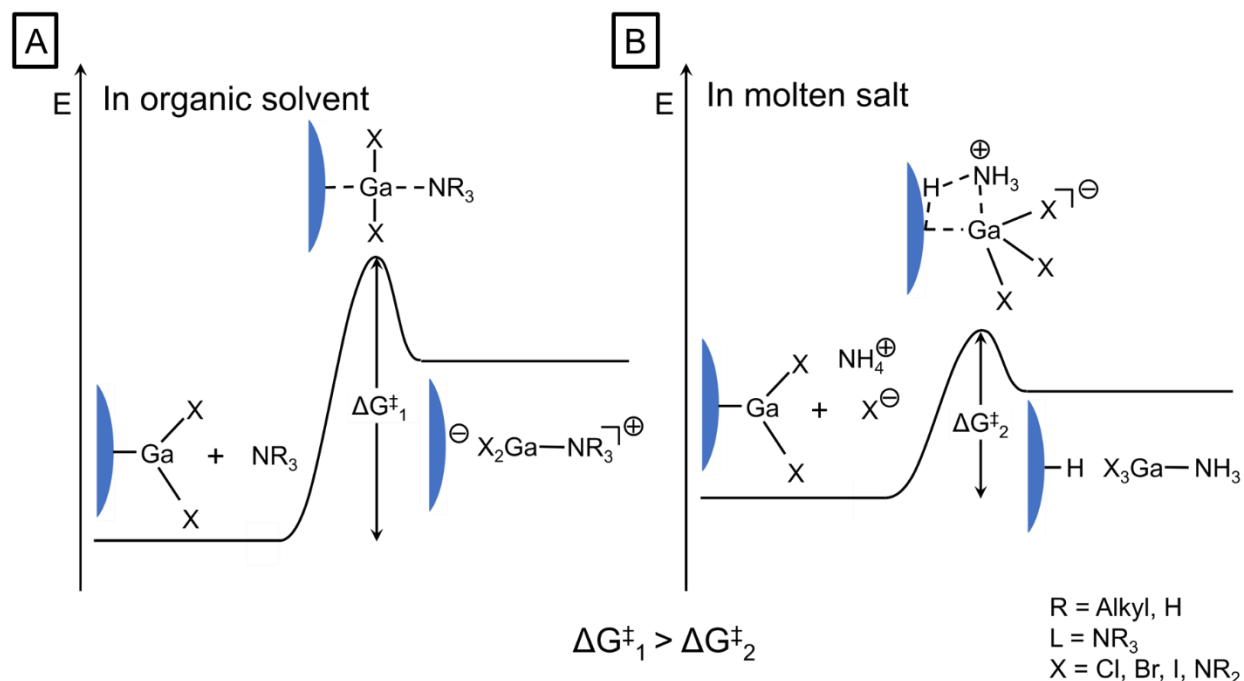


Figure 2.15. The free energy landscapes for the elementary step of breaking Ga-N surface bonds required for establishing microscopic reversibility. (A) A breaking step of Ga-N surface bond separates charges in a non-polar medium, increasing the energy of the system in large degree. (B) A highly polarizable molten salt medium facilitates rearrangement of surface Ga-N bonds during nanocrystal growth by effectively balancing charges upon breaking of a surface Ga-N bond. Adapted with permission from Ref. [20]. Copyright 2023 American Chemical Society.

2.8. Solution Synthesis of III-Nitride Nanostructures Using High-Pressure Ammonia

The growth of bulk GaN crystals is typically carried out using high-pressure ammonia, often under supercritical conditions.^{56,66} To test the effect of ammonia pressure on the colloidal synthesis of III-nitride nanocrystals, we developed a system for running solution phase reactions under high-pressure ammonia gas.

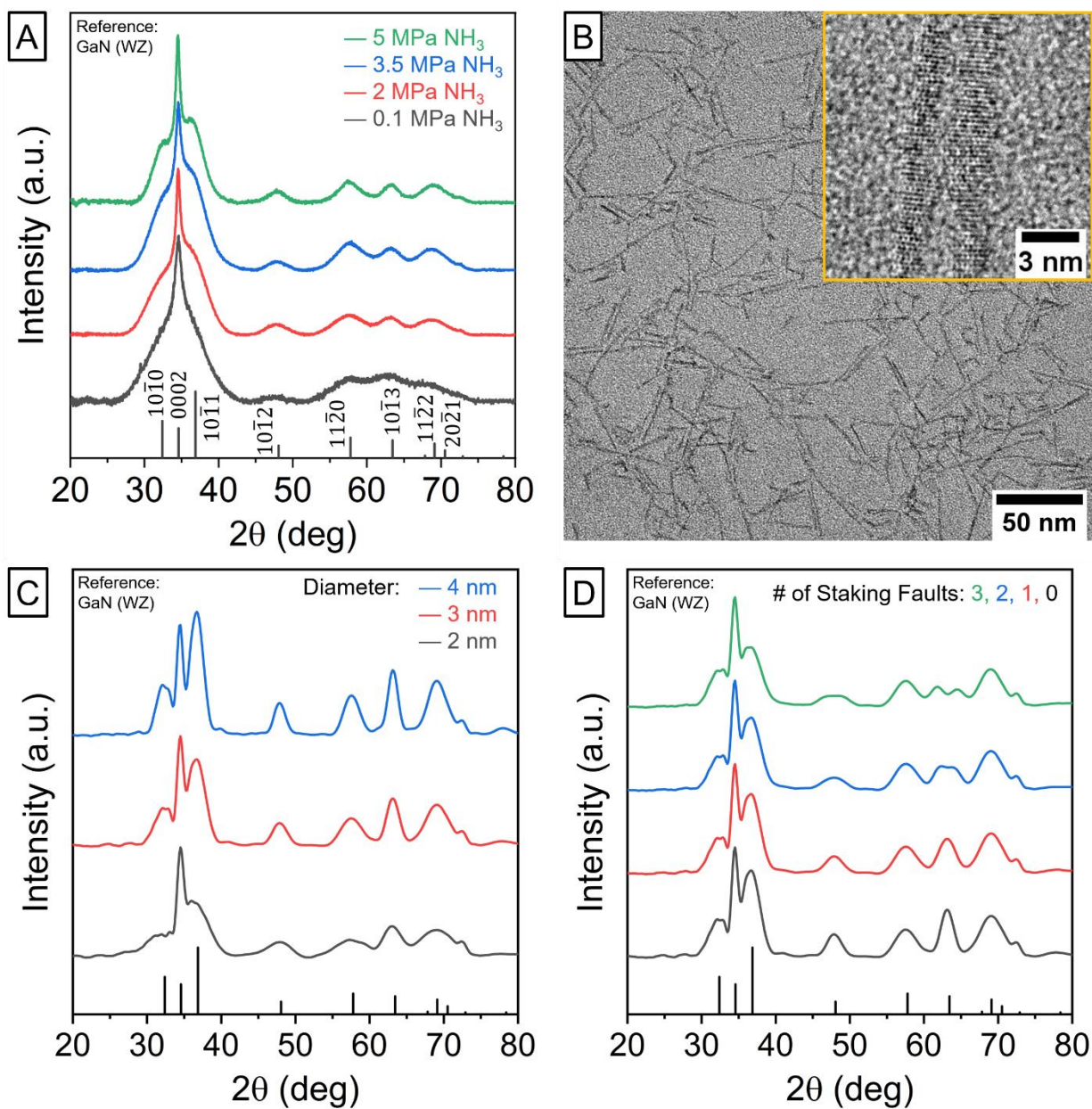


Figure 2.16. (A) PXR D patterns of GaN nanorods produced using different ammonia pressures. Black vertical lines correspond to a WZ GaN reference. (B) A TEM image of GaN nanostructures synthesized using 5-MPa ammonia. The inset shows a high-resolution TEM image of GaN nanorods. (C, D) Simulated PXR D patterns of WZ GaN nanorods with different thicknesses (C) and different numbers of stacking faults (D). Adapted with permission from Ref. [20]. Copyright 2023 American Chemical Society.

A mixture of 5 mmol of KGaCl_4 , 4 mL of TOA, and 0.6 g of HDA was contained in a silicon nitride liner and pre-heated to 290 °C in a stainless-steel pressure vessel. High-pressure ammonia was prepared by heating pre-dried liquid ammonia in a separate pressure vessel. The two pressure vessels were connected, and high-pressure ammonia of 2, 3.5, or 5 MPa was transferred to the reaction vessel. As the case of ambient pressure GaN synthesis, after heating for one hour at 290 °C, the vessels were cooled to room temperature. As an ambient-pressure (100 kPa) control, the reaction mixture containing the same amounts of KGaCl_4 , TOA, and HDA was pre-heated to 290 °C, followed by a flow of ambient-pressure ammonia for 5 minutes. This mixture was maintained for one hour at 290 °C, and then cooled to room temperature. In all cases, as-synthesized particles did not form stable colloidal dispersions and could be collected by centrifugation. Precipitates were washed first with toluene to remove excess alkylamines and then with methanol to remove salt byproducts. A brief sonication with oleylamine and oleic acid (10 % v/v each) in *n*-hexane or toluene stabilized the GaN nanocrystals as a colloidal solution. After removal of the remaining solids by centrifugation, GaN nanocrystals were flocculated with ethanol from colloidal solution and redispersed in fresh *n*-hexane or methylcyclohexane.

While GaN nanorods were formed regardless of ammonia pressure, a clear difference between the reaction products synthesized using ambient-pressure ammonia and high-pressure ammonia was observed in PXRD patterns and in the absorption spectra (Figures 2.16 A, 2.18 A). Generally, the diameter of GaN nanorods increased as the ammonia pressure increased. The X-ray diffraction peaks became significantly narrower for nanorods grown at higher ammonia pressures (Figure 2.16 A). This trend agreed with our simulated PXRD patterns of WZ-GaN nanorods with different thicknesses (Figure 2.16 C). PXRD patterns of high-pressure reaction products also showed a more intense $(10\bar{1}1)$ peak compared to the $(10\bar{1}0)$ peak. Our simulations suggest that

stacking faults can decrease the intensity ratio of $(10\bar{1}1)$ to $(10\bar{1}0)$ (Figure 2.16 D), and a more intense $(10\bar{1}1)$ peak may imply that WZ-GaN nanocrystals synthesized at high ammonia pressure have fewer stacking faults. GaN nanocrystals synthesized at high ammonia pressure also yielded TEM images of higher contrast compared to the materials synthesized at an ambient pressure (Figure 2.16 B).

A PDF analysis further confirmed the formation of highly crystalline GaN (Figure 2.17 A). It is notable that the PDF of GaN nanorods synthesized with high-pressure ammonia exhibits long-range correlations, up to ~ 7 nm distances (Figure 2.17 B). The period of these oscillations was 0.26 nm, which is one-half of c-lattice constant of GaN, implying elongation of WZ nanocrystals along $[0001]$ direction.

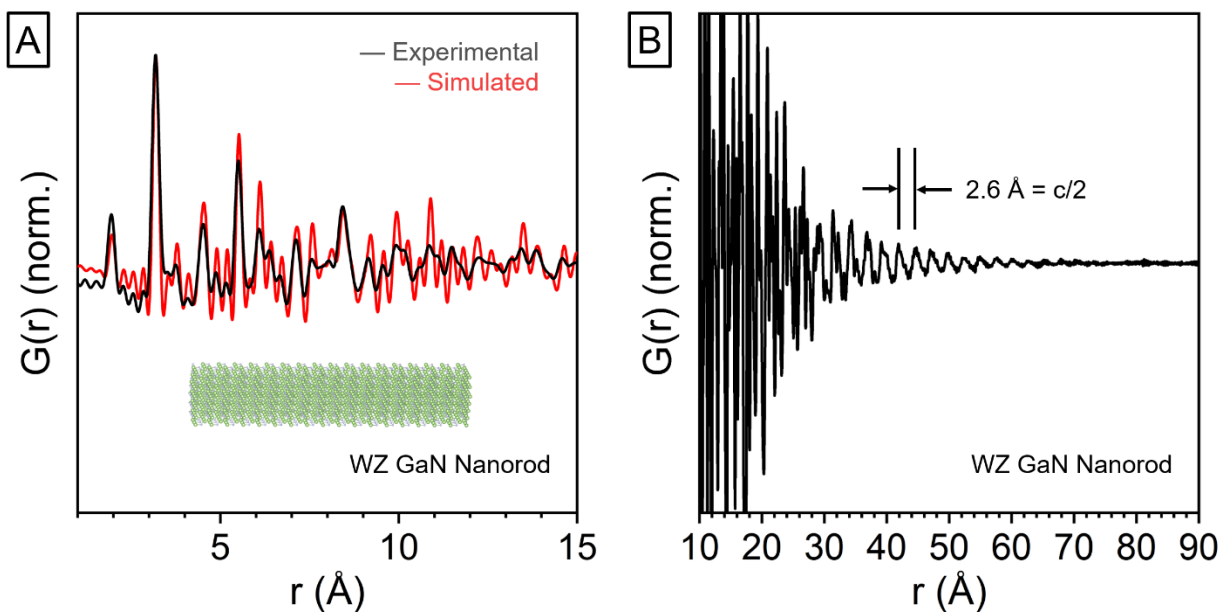


Figure 2.17. A PDF pattern of GaN nanorods synthesized with ammonia at 5 MPa. (E) Shorter range data (black line) in pair with a simulated PDF pattern (red line) from WZ GaN nanorod with 2-nm diameter and 9-nm length (inset cartoon). (F) A longer range PDF reveals $[0002]$ planes of WZ GaN. Adapted with permission from Ref. [20]. Copyright 2023 American Chemical Society.

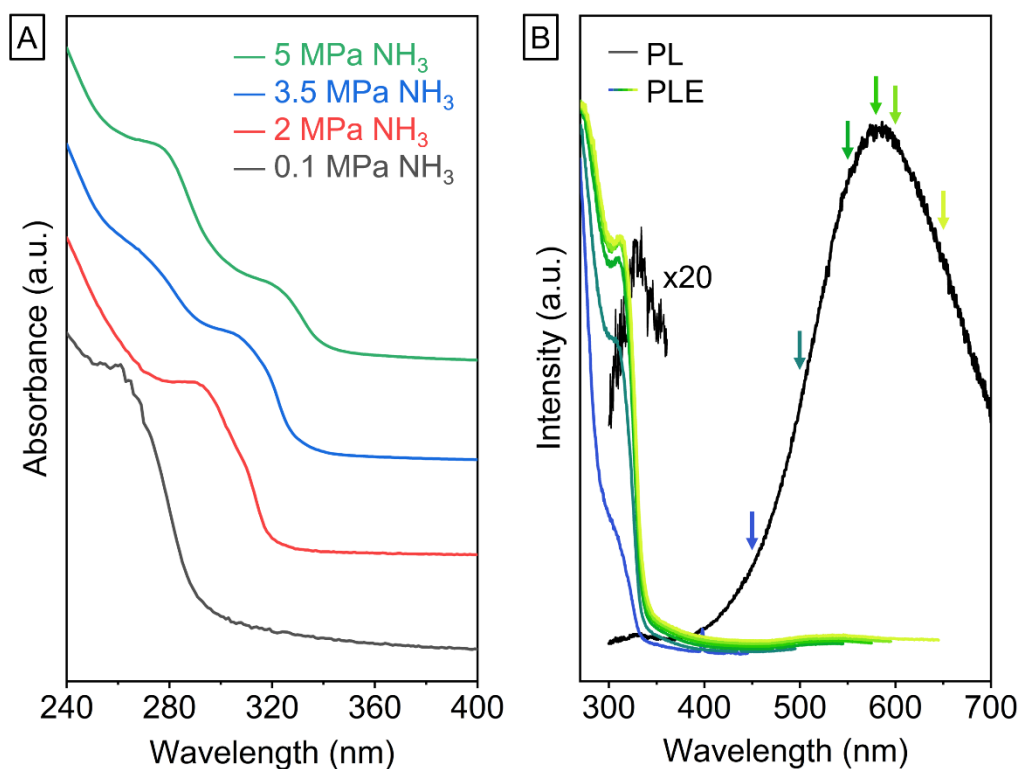


Figure 2.18. Optical properties of GaN nanorods synthesized using high-pressure ammonia. (A) Absorption spectra of GaN nanorods dispersed in methylcyclohexane produced using different ammonia pressures. Small artifacts between 250-270 nm are from trace amounts of residual toluene. (B) Photoluminescence (PL, black curves) and photoluminescence excitation (PLE, colored curves) spectra of GaN nanorods from synthesis with 5 MPa ammonia. Arrows indicate the monitored emission wavelengths of PLE spectra of corresponding colors. The PLE spectra hint that the populations of thicker nanorods emit from midgap states of lower energy. Reprinted with permission from Ref. [20]. Copyright 2023 American Chemical Society.

The absorption spectra of colloidal GaN nanorods showed absorption peaks that can be assigned to the excitonic transitions. As the synthesis pressure increased, the excitonic transitions in the absorption spectra of GaN nanorods shifted to longer wavelengths, as expected for reduced quantum confinement for larger nanorod diameters (Figure 2.18 A). Upon excitation at 270 nm, colloidal GaN nanorods synthesized at 5 MPa ammonia pressure showed a broad band of trap emission centered around 580 nm (Figure 2.18 B). The photoluminescence excitation (PLE)

spectra confirm that this trap emission originated from the particles. PLE spectra measured at different emission wavelengths indicate that our product consisted of nanocrystals of different absorption profiles and that thicker particles showed redder trap emission.

Colloidal GaN nanoparticle samples often showed a photoluminescence (PL) band between 300 nm and 350 nm. The solution of GaN nanorods synthesized at 5MPa ammonia pressure also showed a small peak at 330 nm (Figures 2.18 B). Very similar ultraviolet (UV) emission components slightly red-shifted with respect to the excitonic absorption peaks were observed in many GaN nanocrystal samples (Figure 2.19 A). These PL peaks are reminiscent of the band-edge emission from radiative exciton recombination, but such assignment requires great caution because molecular gallium species coordinated with amines and halides can also emit in this wavelength range. For example, we found that a stoichiometric mixture of gallium chloride and oleylamine dissolved in methylcyclohexane showed emission centered around 325 nm upon excitation at 270 nm (Figure 2.19 B). As a small quantity of gallium-amine complexes can be present in colloidal solutions of GaN nanocrystals as impurities, weak band-edge-like emission components of these solutions may be misleading. Similar to other nanocrystal systems, we expect that further improvements of surface passivation of GaN nanocrystals, e.g., by growing core-shell nano-heterostructures, will significantly amplify the band-edge emission.

To the best of our knowledge, controlling ammonia pressure has not previously been used for solution synthesis of III-nitride nanomaterials. We showed that elevated ammonia pressure can be useful for the synthesis of GaN nanocrystals, as their sizes and correspondingly their size-dependent electronic structures due to the quantum confinement effect can be successfully varied by controlling ammonia pressure. Growing nanocrystals with better crystal quality will be

beneficial for shell growth and other post-synthetic modifications, film deposition, electronic and optoelectronic properties, as well as other material characteristics.

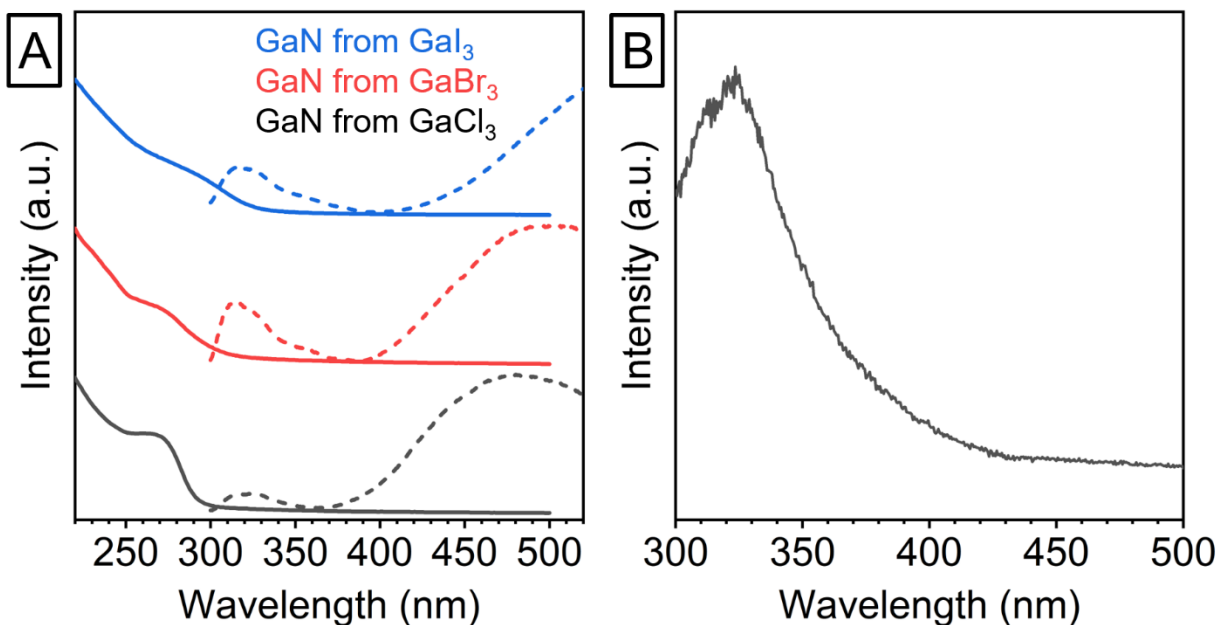


Figure 2.19. (A) Absorbance (solid lines) and photoluminescence (dashed lines) of colloidal GaN nanoparticles synthesized with GaCl₃ (black curves), GaBr₃ (red curves), and GaI₃ (blue curves). (B) Photoluminescence of stoichiometric mixture of GaCl₃ and oleylamine diluted in methylcyclohexane. Adapted with permission from Ref. [20]. Copyright 2023 American Chemical Society.

2.9. Summary and Outlook

We found that an inclusion of a molten salt phase into solution synthesis enables formation of crystalline GaN and AlN nanoparticles at mild temperatures. In the case of GaN, nanocrystals with different crystal phases and shapes could be obtained, depending on the precursor. We further showed that high-pressure ammonia increases the diameter of GaN nanorods and improves their crystallinity. We suggest that molten salt phases provide a solvent which is capable of stabilizing charged species generated during monomer detachment step, which facilitates microscopic

reversibility necessary for the growth of defect-free crystals. By utilizing molten salt emulsions, we hope that various III-nitrides and other difficult-to-crystallize materials can be synthesized via inexpensive and scalable solution methods for future applications.

2.10. Experimental Details

2.10.1. Chemicals

Aluminum bromide (AlBr_3 , Alfa Aesar, ultra dry, 99.999%), ethanol (Sigma-Aldrich, 200 proof, anhydrous, $\geq 99.5\%$), *n*-hexane (Sigma-Aldrich, anhydrous, 95%), gallium bromide (GaBr_3 , Alfa Aesar, ultra dry, 99.998%), gallium chloride (GaCl_3 , Alfa Aesar, ultra dry, 99.999%), gallium iodide (GaI_3 , Alfa Aesar, ultra dry, powder, 99.999%), methanol (Sigma-Aldrich, anhydrous, 99.8%), methylcyclohexane (Sigma-Aldrich, anhydrous, $\geq 99\%$) potassium chloride (KCl, Alfa Aesar, ultra dry, 99.95%), toluene (Sigma-Aldrich, anhydrous, 99.8%) were stored under inert atmosphere and used as received. Potassium tetrachlorogallate (KGaCl_4) was prepared by melting a stoichiometric mixture of GaCl_3 and KCl under nitrogen. Oleic acid (Sigma-Aldrich, technical grade, 90%), oleylamine (Sigma-Aldrich, technical grade, 70%), and stearic acid (Fluka, 97%) were dried under vacuum at 100 °C for 3 hours and stored under nitrogen. Trioctylamine (TOA, Sigma-Aldrich, 98%) and hexadecylamine (HDA, Sigma-Aldrich, technical grade, 90%) were vacuum distilled over sodium (Sigma-Aldrich, 99.8%) and stored under nitrogen. Since it is solid at room temperature, HDA was heated gently to melt it before use. Ammonia gas (Airgas, anhydrous grade) was distilled over sodium (Sigma-Aldrich, 99.8%) in a dry-ice bath right before use for ambient-pressure syntheses. For high-pressure syntheses, the same ammonia gas was condensed inside a high-pressure vessel. Details about high-pressure setups are described below.

2.10.2. Synthesis of Gallium Oxynitride

A solution of gallium stearate was prepared by degassing 0.5 mmol GaCl_3 and 1.5 mmol of stearic acid in 5 mL of TOA at 90 °C for 3 hours under vacuum with vigorous stirring. After degassing, the solution of gallium stearate was heated to 290 °C under nitrogen. Excess ammonia was passed over this mixture for 5 minutes. The reaction mixture was then heated for one hour at 290 °C. After the reaction, the reaction mixture was cooled down to a room temperature by removing the heat source. The gallium oxynitride produced was non-colloidal and was separated from the mixture by centrifugation. The obtained solid was washed with toluene, ethanol, and methanol a few times each.

2.10.3. Synthesis of Amorphous GaN and AlN

In a nitrogen atmosphere, 0.5-1 mmol of gallium or aluminum halide was fully dissolved in 4 mL of TOA. To this mixture, 0.6 g of HDA was added. For heating-up syntheses, the mixture was heated to 290 °C under constant ammonia flow with vigorous stirring. Alternatively, for hot-injection synthesis, the mixture was heated to 290 °C under nitrogen, and then ammonia was passed over the solution for 5 minutes. In both cases, the reaction mixture was heated afterward for 1 hour at 290 °C. The reaction mixture was cooled to a room temperature by removing the heat source. White solids precipitated from the reaction mixture upon cooling. This solid was separated from the solution by centrifugation and washed with 10 mL of toluene a few times for removal of excess organic materials. The remaining solids were washed with 40 mL of methanol a few times to remove ammonium halide byproducts of the reaction.

2.10.4. Synthesis of Crystalline GaN and AlN with Ambient-Pressure Ammonia

In a nitrogen atmosphere, 5 mmol of finely ground gallium or aluminum halide salt was mixed with 4 mL of TOA and 0.6 g of HDA. In a typical heat-up synthesis, the mixture was heated to 290 °C under constant ammonia flow with vigorous stirring. For the KGaCl_4 control experiment, the reaction mixture was first heated to 290 °C, and then ammonia was passed over the solution for 5 minutes. After 1 hour of heating at 290 °C, the heat source was removed, and the reaction mixture was cooled to room temperature. The product spontaneously precipitated from the reaction mixture. This solid was separated with centrifugation, and washed first with 10 mL of toluene and then with 40 mL of methanol a few times each to remove excess organics and salt byproducts. To extract colloidal particles from the solid, the solid was sonicated for 30 minutes with the mixture of 16 mL of *n*-hexane (or toluene), 2 mL of oleylamine, and 2 mL of oleic acid. A solution of nanoparticles was separated with centrifugation from non-colloidal solid. From this solution, nanoparticles could be flocculated with ethanol. Particles were washed a few times with ethanol before finally dispersed in methylcyclohexane or *n*-hexane for measurements.

2.10.5. High-Pressure Setup (Figure 2.20)

Two identical high-pressure vessels from Parr Instrument Company (Series 4740, 75 mL) were used for the setup. A tee with three needle valves was set to connect two vessels and a Schlenk line, which was necessary to operate the system under air-free condition. To one fully evacuated vessel, liquid ammonia was condensed by using an ice/water bath. The other one, equipped with a silicon nitride liner and a needle valve, worked as a detachable reaction vessel, which could be brought in and out of the nitrogen glovebox for air-free preparation of the reaction mixture. For an

operation, the system was assembled and properly evacuated through a Schlenk line. Two heating tapes were used to heat the two vessels separately. Caution! The pressure of ammonia will be high enough to break glassware, so needle valves must be manipulated with care to ensure high-pressure ammonia is not admitted to the Schlenk line.

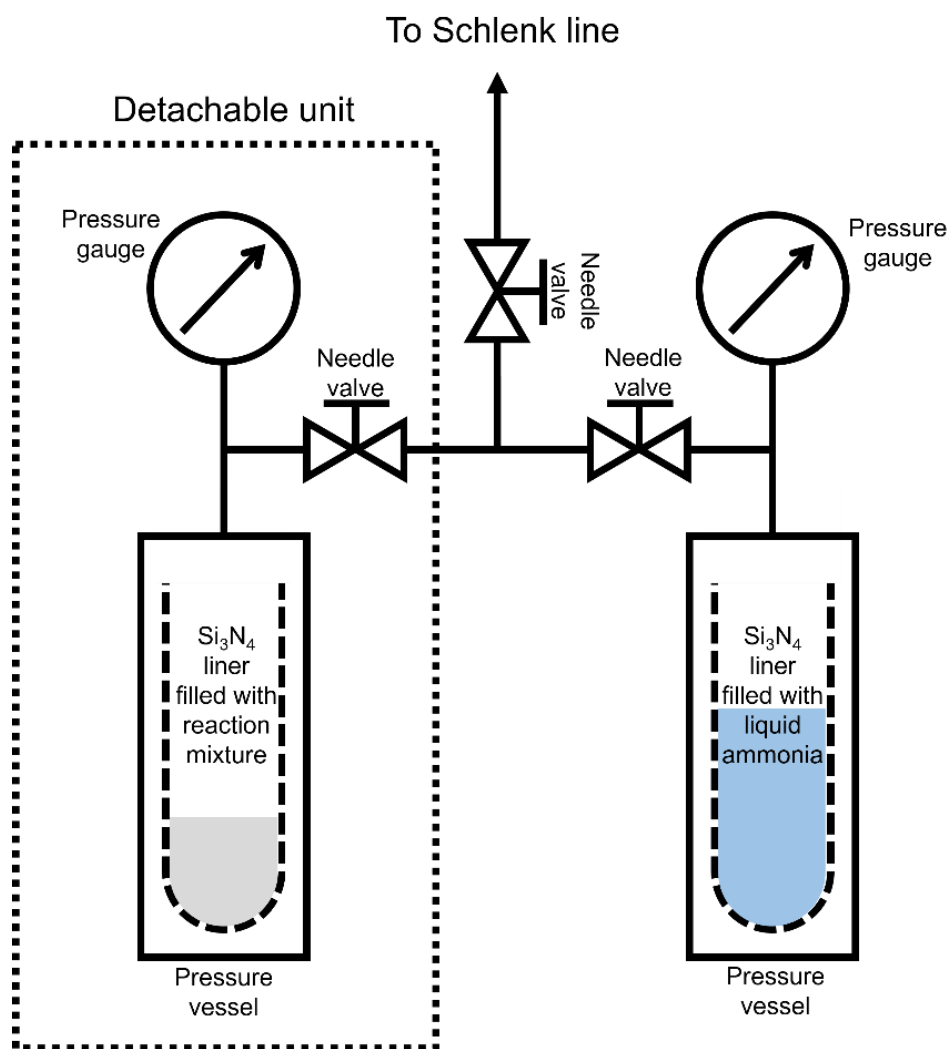


Figure 2.20. A scheme for the high-pressure reactor setup. Reprinted with permission from Ref. [20]. Copyright 2023 American Chemical Society.

2.10.6. Synthesis of GaN under High-Pressure Ammonia

In the reaction vessel, 5 mmol of finely ground KGaCl_4 , 4 mL of TOA, and 0.6 g of HDA were loaded together with a glass stir bar under nitrogen atmosphere. After the reaction vessel was assembled to the system, two pressure vessels were heated separately; the one with the reaction mixture was heated to 290 °C under ambient pressure nitrogen with vigorous stirring, while the other with liquid ammonia was heated gently to a pressure about 2-3 MPa higher than the target pressure. To the heated reaction mixture, desired pressure (2, 3.5, or 5 MPa) of hot ammonia gas was transferred by manipulating the two needle valves between the two pressure vessels. During this process, the needle valve toward the Schlenk line must be closed. After 1 hour of reaction, pressurized gas in the reaction vessel was slowly vented until the pressure reached 1 MPa, a pressure high enough to prevent back flow of an air into the vessel during venting and low enough to avoid a condensation of liquid ammonia during cooling. The reaction vessel was cooled to a room temperature and transferred into a nitrogen atmosphere. The reaction product was washed with toluene and methanol a few times each. Colloidal solutions of these products were obtained by sonication of the solid products with 16 mL of *n*-hexane (or toluene), 2 mL of oleylamine, and 2 mL of oleic acid. Nanoparticles were flocculated with ethanol from this solution, collected by centrifugation, and dispersed in methylcyclohexane or *n*-hexane for subsequent measurements.

2.10.7. Characterization Techniques

Transmission electron microscopy (TEM). TEM images were obtained with a 300kV FEI Tecnai G2 F30 microscope. Samples were prepared by drying colloidal solutions diluted in toluene

on Ted Pella pure carbon film grids. After evaporation of toluene, grids were washed gently with ethanol and dried under vacuum.

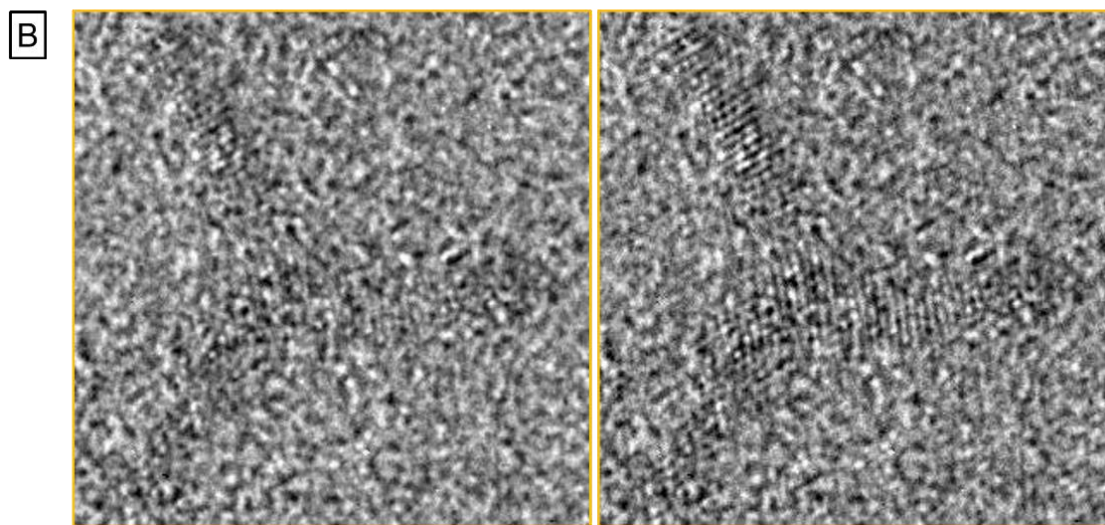
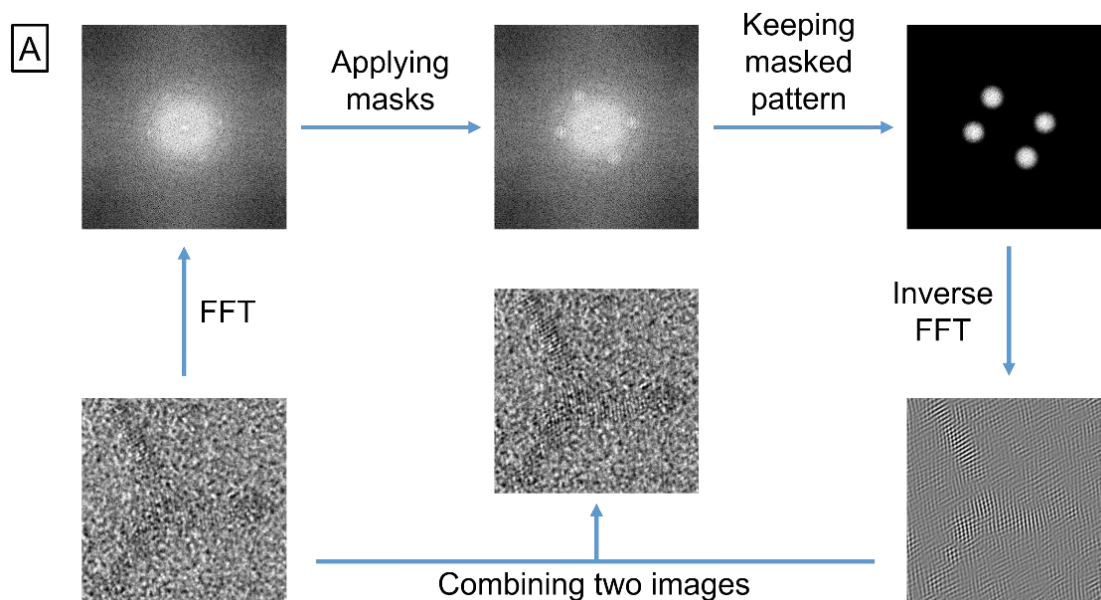


Figure 2.21. Enhancement of high-resolution TEM images. (A) Scheme for the enhancement. (B) Side-by-side comparison of an image of a GaN nanoparticle before (left) and after enhancement (right). Reprinted with permission from Ref. [20]. Copyright 2023 American Chemical Society.

As the lattice contrast of GaN and AlN nanoparticles in TEM images is naturally low due to low nuclear charges of the materials, small sizes of the nanoparticles, and high accelerating voltage of electron beam source, for better visibility, lattice fringes in high-resolution TEM images were enhanced in contrast with Gatan DigitalMicrograph® (Figure 2.21). In detail, raw high-resolution TEM images were cropped to desired sizes to represent a few nanoparticles. Diffraction patterns of these cropped images were obtained by fast Fourier transform (FFT). Spot masks were applied to bright spots in the diffraction patterns and separated from the whole pattern. These separated patterns were turned into real-space images by inverse FFT and added to the original image.

Optical spectra. Colloidal samples were gently washed with ethanol to remove excess organic ligands and the original solvent, and then were redispersed as dilute solutions in methylcyclohexane. Absorption spectra of these solution samples were taken with a Shimadzu UV-3600 Plus spectrophotometer from 220 nm to 500 nm. Photoluminescence (PL) and photoluminescence excitation (PLE) spectra of solution samples were taken with a Horiba Jobin Yvon FluoroMax-4.

Powder X-ray diffraction (PXRD). PXRD patterns were obtained with a Rigaku MiniFlex with a Cu K α source. Samples were prepared by drying concentrated colloidal solutions on zero-diffraction silicon plates (Rigaku 906165 Flush, Si510).

Pair distribution function (PDF) measurement. PDF data was collected from beamline 11-ID-B of the Advanced Photon Source (APS) at Argonne National Laboratory (ANL). Total scattering data were acquired as images on a large flat panel detector. GSAS-II software¹⁰⁷ was used to reduce 2-D diffraction images to 1-D diffraction patterns. Masks were drawn and

integration processes were carried out using the software. Pair distribution functions were extracted from 1-D diffraction patterns with scaling Q-range of 20.782 - 23.091.

2.11. Simulation Details

2.11.1. Powder X-ray Diffraction (PXRD) Simulations

Powder X-ray diffraction patterns were simulated from structures built using the AtomsK software package.¹⁰⁸ Briefly, GaN nanorods of different sizes were prepared by first generating a large GaN supercell and then using a cylindrical cutoff oriented parallel to the c-axis to prepare cylindrical nanorods. Atomic structures were visualized using the VESTA software package.¹⁰⁹ X-ray diffraction patterns were simulated using the DebyeByPy software package¹¹⁰ which calculates intensities (I) as a function of the scattering length vector (q) in units of \AA^{-1} using the Debye formula:

$$I(q) = \sum_i \sum_j f_i(q) f_j(q) \frac{\sin(qr_{ij})}{r_{ij}}$$

where the sums are over all of the atom pairs, f is the angle-dependent scattering factor calculated from Hartree-Fock wavefunctions by Cromer and Mann,¹¹¹ and r is the distance between atoms in \AA .¹¹² The simulated data were plotted against 2θ ($2\theta = 2 \arcsin(\lambda q / 4\pi)$), where λ is the wavelength of the X-ray source).

2.11.2. Pair Distribution Function (PDF) Simulations

Simulated pair distribution functions were obtained from conversion of simulated PXRD patterns. PXRD patterns were obtained from the method above in the q range of $(0,25] \text{ \AA}^{-1}$, and converted into PDFs with the program PDFgetX3 in the xPDFsuite package.¹¹³

CHAPTER THREE

HIGH-PRESSURE REACTOR SYSTEMS

A high-pressure reactor can be a useful setup for synthesis and post-synthetic treatment of nanoparticles. Though a pressure limit of this steel reactor is not comparable to that of a diamond anvil cell (770 GPa), it can contain much higher pressure than laboratory glass apparatus, up to 170 MPa for setups described in this chapter. A limitation in volume of a steel reactor is comparable to that of a glass counterpart. Reactions using high-pressure reactors are as scalable as those in glass reactors. Overall, any reaction that can be done in glass flasks can be done in high-pressure vessel in the similar way, but at an elevated pressure.

Taking advantage of a high-pressure reactor, colloidal nanoparticle synthesis can expand its solvent selection. Solvothermal process is an interesting way of utilizing the pressure vessel, as it allows a reaction to use a solvent having a lower boiling point than a reaction temperature. Limitation on the number of available high-boiling solvents in many nanoparticle syntheses is not a problem in solvothermal process. Furthermore, high-pressure reactor can contain a reaction in supercritical fluid. A solvent in supercritical fluid phase is much different from that of liquid phase in its characteristics such as density, viscosity, and dielectric constant. Consequently, solubility of chemicals and their reactivity in supercritical fluid are unlike those in liquid solvent. It seems that

nanoparticle synthesis in solvothermal or supercritical condition is not yet fully explored. A high-pressure reactor can provide new opportunities in this parameter space for nanoparticle synthesis.

A high-pressure reactor can be utilized to explore nanoparticle synthesis under high-pressure gas. For reactions using gaseous reactants, to use high-pressure reactant is to have the reactants in high concentration. As shown in the previous chapter, gallium nitride nanoparticle synthesis with gallium halide and ammonia yielded thicker nanorods with higher-pressure ammonia.²⁰ Controlling pressure is one of the most reliable way to control concentration of gaseous reactants and a high-pressure reactor will give chances to explore this parameter space. Also, high-pressure gas may directly affect the nucleation and growth of nanoparticle. As effective volumes of monomers and nucleus are different, outer pressure will certainly affect the nucleation and growth. The effect of this pressure to nanoparticle synthesis has not been explored well, and it is expected that high-pressure reactor can play a role in this research.

Another use of a high-pressure reactor in nanoparticle field is at post-synthetic treatments. It has been shown that III-V nanoparticles can be alloyed with other group XIII cations through cation exchange in molten salt.¹¹⁴ For III-nitrides, similar cation exchange has not been achieved yet due to thermal decomposition of III-nitride nanoparticles. It is known that high-pressure nitrogen can inhibit thermal decomposition of III-nitrides,⁵⁶ and cation exchange of these nanocrystals in molten salt may be realized under high-pressure nitrogen. Another use is at hot-isostatic pressing. Recently, a high-pressure reactor was utilized in hot-isostatic pressing of thin films of ZnSe and ZnS nanocrystals to tune porosity and refractive index.¹¹⁵

There can be many other usages of high-pressure reactor in nanocrystal chemistry, as most chemistry that have been done under ambient pressure in glass apparatus can also be done in a

high-pressure reactor. This chapter describes structures and uses of different high-pressure reactors and related systems in detail.

Table 3.1. Descriptions on parts used in flow diagrams.

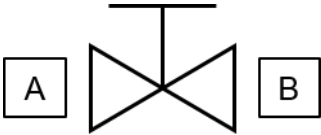
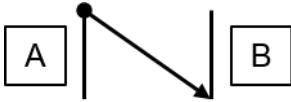
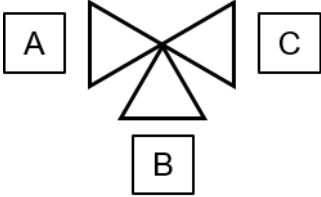
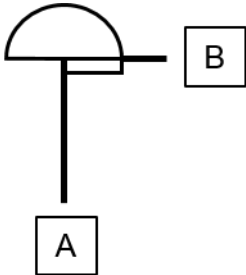
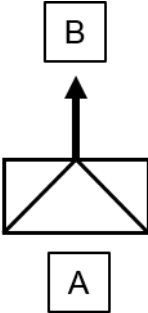
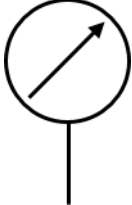



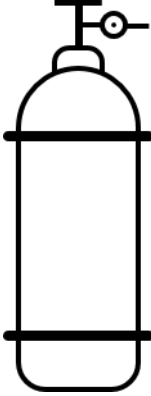
Symbol of the Part	Name of the Part	Description
	Gate Valve	A needle valve to close and open a path of fluid between [A] and [B] sides.
	Check Valve	An one-way valve that allows fluid to flow through it in only one direction from [A] to [B].
	3-Way Valve	A valve connecting three directions. It has three modes of operations: 1) closed for all direction, 2) connecting [A] and [B], and 3) connecting [B] and [C].
	Relief Valve	A safety valve that releases fluid from [A] to [B], when a pressure difference between [A] and [B] sides exceeds a desired level.
	Rupture Disc	A safety device containing a small disc that fails when a pressure difference between [A] and [B] sides exceeds a pressure limit. Upon failure, fluid is released from [A] to [B].

Table 3.1 (continued)

	<p>Pressure Gauge</p>	<p>A mechanical or digital gauge that measures a pressure difference between inside and outside of the gauge.</p>
	<p>Flow Controller</p>	<p>A device to control a flow rate and/or an outlet pressure of fluid that flows through it.</p>
	<p>Gas Purifier</p>	<p>A device to remove undesirable impurities from fluid that flows through it.</p>
	<p>Cold Trap</p>	<p>A device to condense all vapors except the permanent gases into a liquid or solid which is to prevent vapors to enter vacuum pump during evacuation.</p>
	<p>Gas Cylinder</p>	<p>A steel cylinder that contains high-pressure gas, equipped with a gate valve and a regulating valve to control a gas flow and an out pressure of the gas.</p>

3.1. A General Description on a High-Pressure Reactor System

3.1.1. A General Structure of a High-Pressure Reactor System

A high-pressure reactor system consists of a high-pressure reaction vessel, a pressure gauge, gas inlets and outlets, and valves to control gas flows. Gas can be delivered from pressured gas cylinder. With a pressure regulating valve and a flow controller, gas delivery can be controlled precisely. A vacuum line can be added when vacuum-evacuation of a part of the system is needed. Cold trap is necessary to be installed in vacuum line in case of evacuating reactor vessel containing volatile materials. Also, it is highly recommended to have safety devices to any part of the system where working pressure is close to the pressure limit of the part. There are two popular options for safety devices: a relief valve and a rupture disc. A relief valve is the valve that release fluids out of the system when the pressure to the valve is higher than the set pressure of the valve. When the inner pressure decreases below the set pressure during the release, a relief valve is shut and the release is stopped. As a relief valve can work semi-permanently, this valve is suitable for in-line safety device. A rupture disc is a small piece of metal that fails at predetermined pressure difference. This sacrificial part is instantly responding, cheap, leak-tight, and easy to clean, so it is more often used to protect high-pressure vessel. Finally, to prevent accident from any possible leakage and failure of the system, it is recommended to set up the high-pressure reactor system in a well-ventilated place, e.g. fume hood, and to install blast barrier around the system.

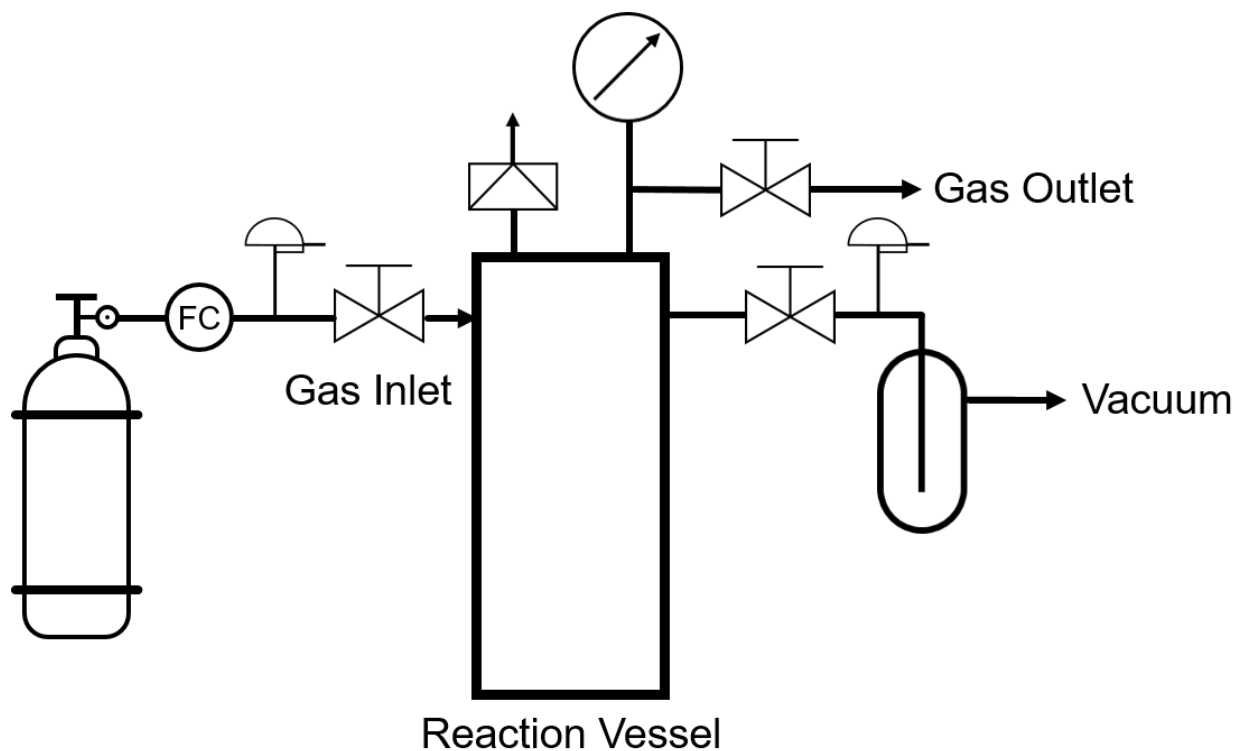


Figure 3.1. A flow diagram for a basic high-pressure reactor system.

3.1.2. A General Way of Assembling High-Pressure Reactor

A high-pressure reactor usually consists of a reaction vessel and a head part unit. For leak-tight assembly, a sealing material should be placed at the junction between the reactor vessel and the head part. It is usually an O-ring (lower pressure), a gasket (higher pressure), or a heavy-duty metal-based grease. To provide enough sealing force, the vessel can be closed with a screw cap. The head part can also include compression bolts to develop even higher sealing forces. These compression bolts should be coated with proper greases and fastened to the right torque specified in a manual. Also, the compression bolts should be tightened in a crisscross sequence to minimize elastic interaction between bolts.

3.2. Air-Free High-Pressure Reactor Systems

For chemical reactions having air-sensitive reagents, air-free preparation of reaction mixture is essential. There can be multiple air-free ways to prepare reaction with a high-pressure reactor. The most expensive but easiest way is to contain a whole reaction system in inert air environment, such as a glovebox. More cost-efficient options can be 1) having an air-tight reactor vessel detachable from the system and 2) having an air-free injection capability to a reaction vessel. For both options, proper vacuum evacuation and inert gas refill cycles are necessary for air-exposed parts before the operation. Structures and operations of four different high-pressure systems for air-free reactions are described below.

3.2.1. Transparent Reactor System with a Thick-Glass Reactor Vessel

Though glass is not the best material for containing high-pressure fluid, properly designed thick glass can bear some pressure difference. Unlike a steel reactor, a glass reactor is transparent, and thus ongoing reaction can be observed. Figure 3.2 shows a scheme for a high-pressure reactor system with a thick glass reactor vessel equipped with nitrogen and ammonia lines. Two inlet gas lines are equipped with flow controllers to control pressures and flows of each gas, and with check valves preventing any back flow and cross contamination. An in-line gas purifier can be also placed to improve a purity of an inlet gas. For the outlet side, a 3-way valve is placed to switch connections to a vacuum line and a gas outlet to an ambient atmosphere. A relief valve for the reactor is set to 225 psi as the pressure limit of the 3-oz pressure reaction vessel from Andrews Glass is 225 psi. This pressure limit should be tuned accordingly to the limit of the reactor vessel. A detachable

reactor unit consists of the glass reactor vessel and a head part, which includes a needle valve. The vessel and the head part can be assembled air-tight with O-rings and threaded couplings.

To prepare a reaction, the vessel and a head part are brought inside a glovebox, filled with reaction mixture, and assembled together. With the valve closed, this air-tight assembly can be brought out from the glovebox, and combined to the reactor system. While the valve of the reactor unit is still closed, with multiple cycles of vacuum evacuation and nitrogen fill, any remaining air is removed from parts of the reactor system which has been exposed to air. Before delivering pressured gas, a steel mesh protective cover should be added to the reaction vessel. If the reaction mixture is needed to be heated or cooled, a heating mantle/tape or a cooling bath can be placed accordingly. A heating can be controlled precisely by a temperature controller with a thermocouple placed in between the reactor vessel and the heat source. The reaction mixture can be stirred with a stir bar and a stir plate similarly to an ambient pressure reaction in a glass flask. Finally, it is recommended to install blast shield around the reactor. Desired pressure of nitrogen and/or ammonia can be delivered with help of flow controllers and pressure regulating valves.

After reaction is completed, the pressure should be released from the reaction vessel through the gas outlet. Purge with a nitrogen flow can be performed subsequently to remove remaining ammonia gas which is detrimental for glovebox atmosphere. With the valve on its head part closed, the reaction vessel can be detached from the reactor system, and transferred to a glovebox for air-free work-up.

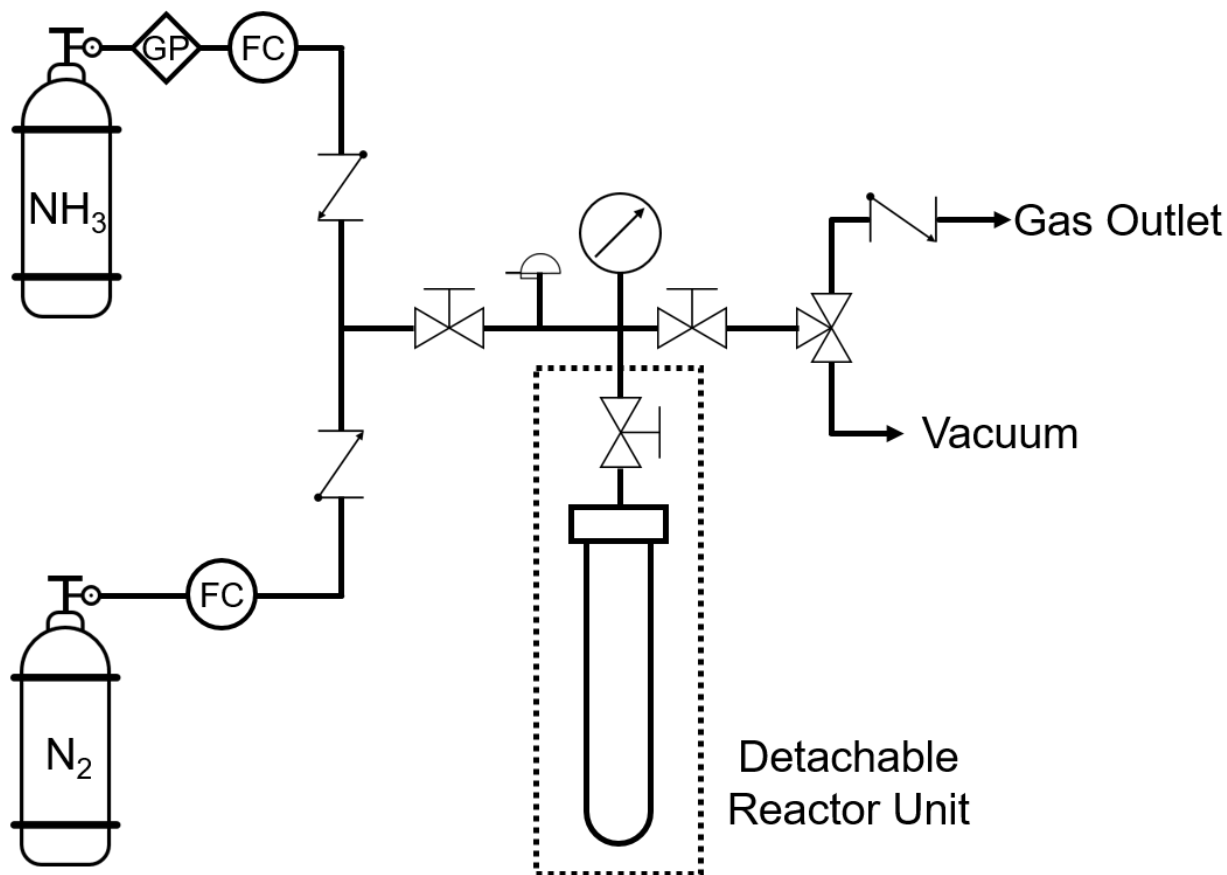


Figure 3.2. A flow diagram for an air-free high-pressure reactor system with a transparent thick-glass reactor vessel.

3.2.2. Stainless Steel Reactor System for High-Pressure Ammonia Delivery

For vapor pressure of ammonia only depends on the temperature, to deliver high-pressure ammonia, a pressure vessel containing liquid ammonia must be heated. Therefore, in this setup, two pressure vessels are integrated to the system; one is a reaction vessel, and the other is an ammonia reservoir. A simple setup includes two pressure vessels connected together with a tee linked to a vacuum/nitrogen Schlenk line and a gas outlet (Figure 3.3).

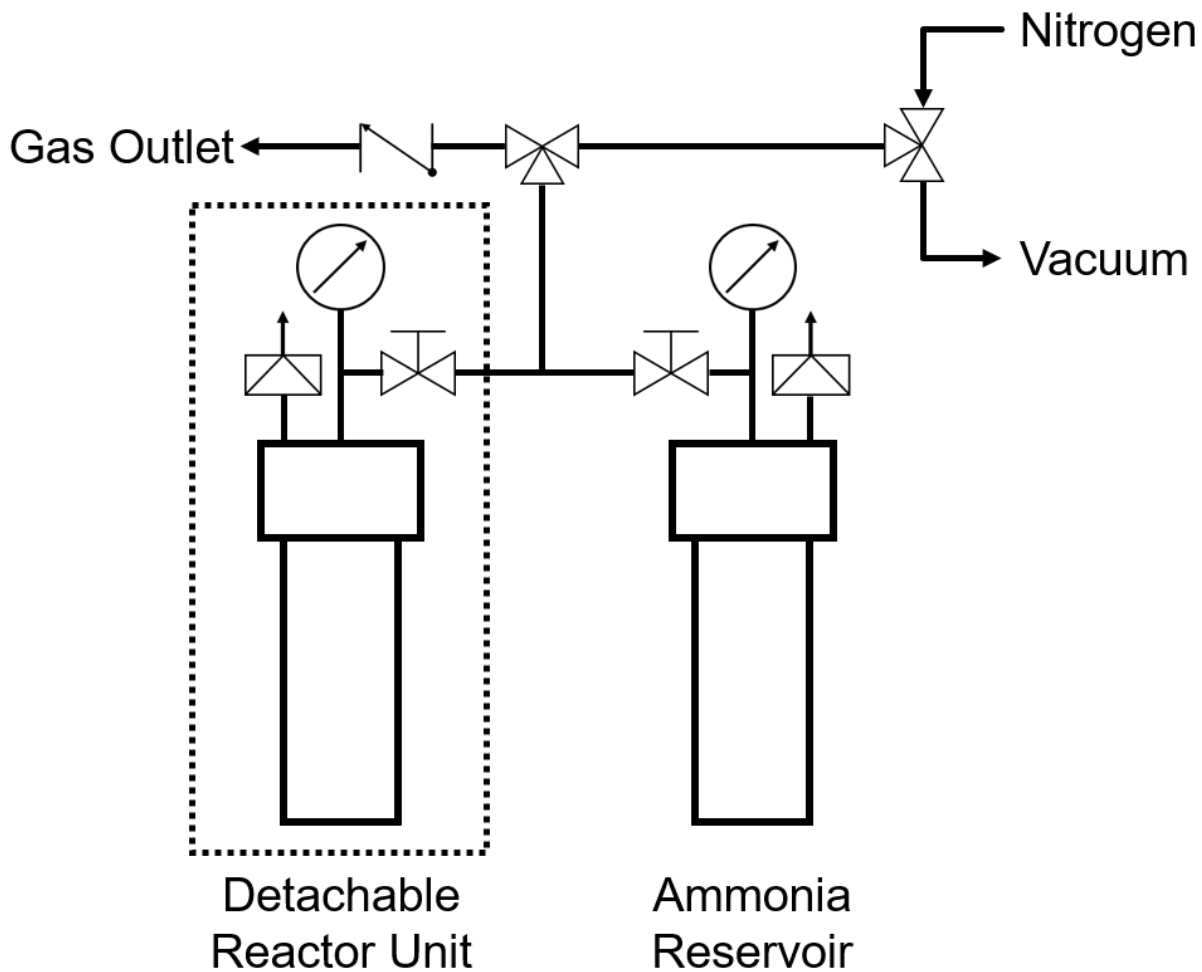


Figure 3.3. A flow diagram for high-pressure reactor system for high-pressure ammonia delivery.

Critical pressure of ammonia is 112.8 bar (1636 psi), which is much lower than pressure limits of common stainless steel vessels. A rupture disc assembly for the reactor vessel is not necessary when only gaseous ammonia is used. However, installation of the safety device is highly recommended when supercritical ammonia is used. Supercritical ammonia not only can challenge the pressure limit of the reactor but also is able to corrode stainless steel over time. Also, if

supercritical ammonia is used regularly, reactor parts need to be checked periodically and must be replaced if they are damaged.

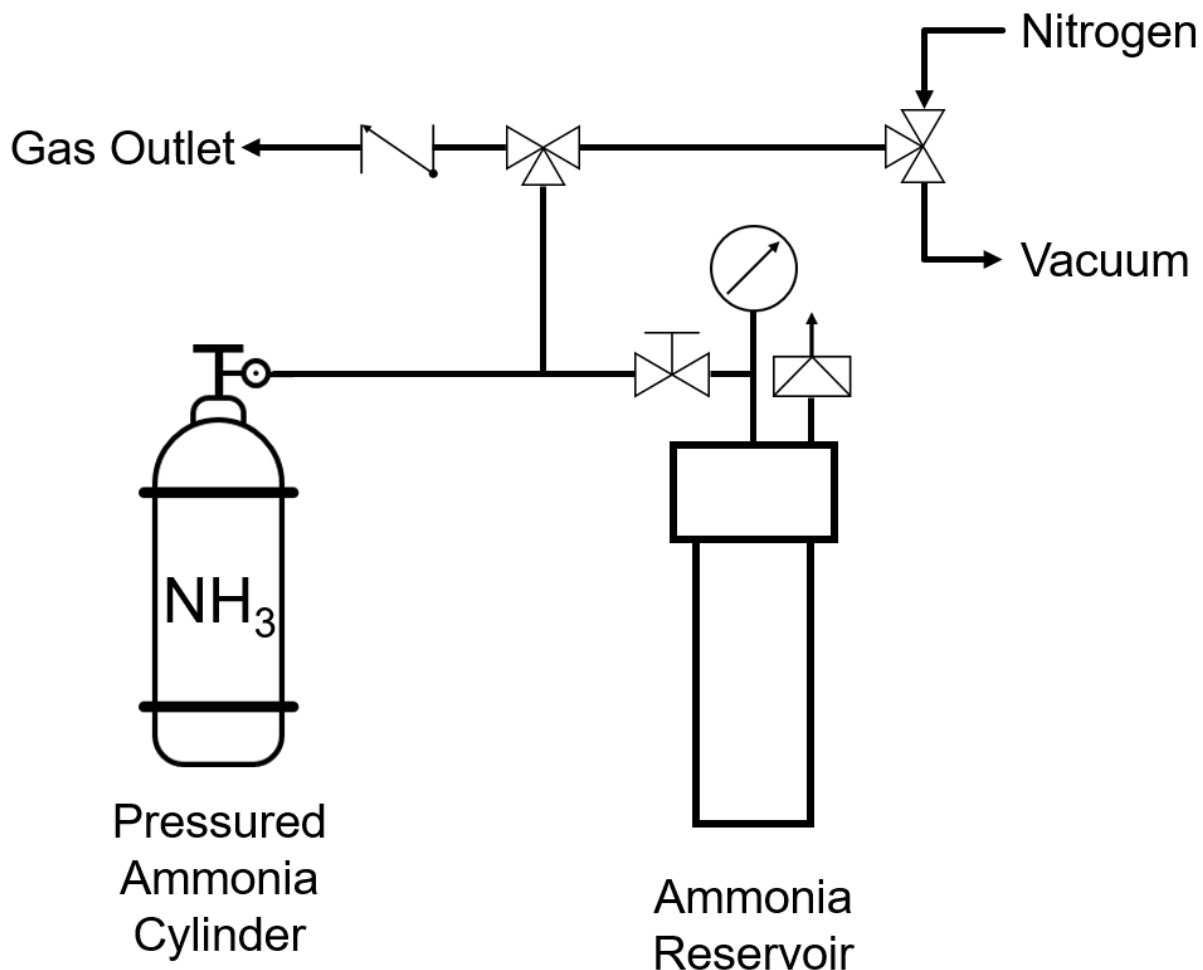


Figure 3.4. A flow diagram for high-pressure reactor system during ammonia fill to an ammonia reservoir.

To fill the ammonia reservoir, a pressured ammonia cylinder is connected to the system through a pressure tubing (Figure 3.4). After extensive evacuation of the reservoir and the tubing, the vacuum line is closed, and the reservoir vessel is placed in ice-water bath. Upon opening the

valves of the ammonia cylinder, ammonia starts to flow from the cylinder to the reservoir and condense inside of the reservoir. After condensation is done, valves on the two ammonia tanks are closed, remaining ammonia in the tubing is released through the gas outlet, and the ammonia cylinder is detached from the system.

The reaction vessel unit consists of a stainless steel cylinder with a silicon nitride liner and a head part with a needle valve. To prepare a reaction, this unit is transferred into a glovebox, filled with a reaction mixture, and assembled together with a graphite gasket in between. The valve at the head part is closed before the reactor unit is brought out from the glovebox. After assembling the reactor unit to the system, air-exposed connection part undergoes cycles of vacuum evacuation and nitrogen fill, and left under vacuum. If necessary, the reaction mixture can include a stir bar, and be stirred with a stir plate.

With two heating tapes, the reaction vessel and the ammonia vessel can be heated separately. The reaction vessel is heated to a desired reaction temperature precisely with a temperature controller. Thermocouple can be placed in between the reactor and the heating tape, or in a thermowell of the reactor vessel if the vessel has it. The ammonia reservoir can be heated to a desired pressure without a precise temperature control. As pressure of ammonia at the reservoir decreases during ammonia transfer to the reaction vessel, the reservoir is heated until it has a higher pressure than the desired ammonia pressure for the reaction. When the reaction vessel is heated to a desired temperature and the ammonia vessel is heated to have appropriate pressure, vacuum line is closed, and two valves in between two pressure vessels are opened. Ammonia transfer is quick and the valves are closed shortly to minimize any diffusion of reaction mixture to the ammonia reservoir. Heating to the ammonia reservoir is stopped when no more ammonia transfer is needed.

The reaction is stopped by removing heating source around the reaction vessel. If excess unreacted ammonia remains after the reaction, it condenses inside the reaction vessel during cooling down. If formation of liquid ammonia is detrimental to the reaction product, ammonia pressure should be released when the reaction vessel is still hot. After cooling down to room temperature, any remaining ammonia is released to the gas outlet. With the valve closed, the reaction vessel unit can be detached from the system and transferred to a glovebox for air-free work-up.

3.2.3. High-Pressure Reactor System with a Gas Booster

If a gas input to the high-pressure reactor is directly from a pressurized gas cylinder, the input pressure is limited by the pressure of the gas cylinder. There can be ways to overcome this limit, e.g. including liquid nitrogen or an azide salt in a reaction vessel which yields high-pressure dinitrogen at elevated temperature. Another way introduced here is using a gas booster (Haskel 80512). This air driven gas booster amplifies the pressure of input gas by cycles of compression driven with compressed air (air drive). The pressure of output gas is determined by pressure of the input gas and the air drive, and the maximum output pressure is 20000 psi. The gas booster cannot work with liquid and only gas which does not condense at this pressure range can be used.

Figure 3.5 describes the structure of the reactor system with the gas booster. A gas inlet equipped with the gas booster, ambient nitrogen/vacuum line for evacuation, and a gas outlet are linked to a pressure vessel with a needle valve. A gas purifier can be installed before the gas booster to further decrease the concentration of impurities which can also be amplified by the gas booster together with the input gas.

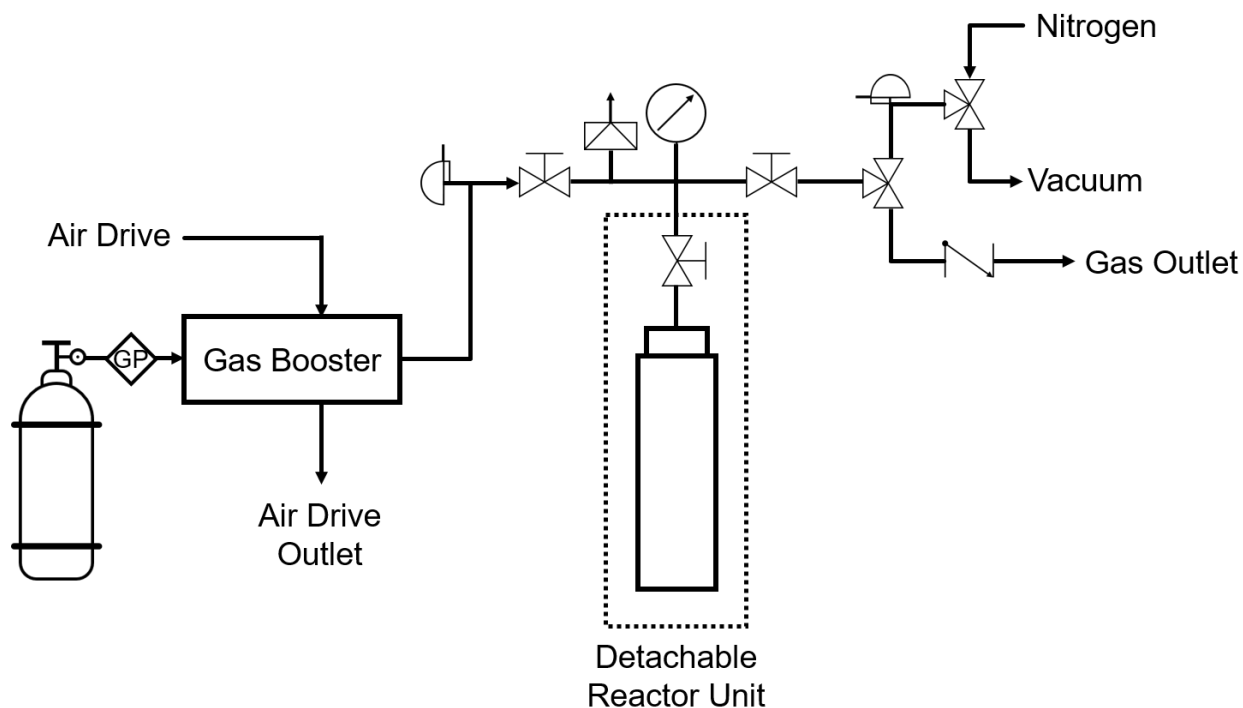


Figure 3.5. A flow diagram for high-pressure reactor system with a gas booster.

Operation of this reactor system is similar with that of previously described reactor system. The detachable reactor vessel unit is transferred into a glovebox for reaction preparation, assembled, and brought out from the glovebox with the valve closed. After the reactor vessel is assembled into the system, with cycles of vacuum evacuation and nitrogen fill, remaining air in the system is removed. The reactor vessel is filled with high-pressure gas of a desired pressure. The reactor vessel can be heated with a heating tape with a temperature control or be cooled with a cold bath. A thermocouple can be placed in between the reaction vessel and the heat source, or in a thermowell of the reactor vessel. Reaction mixture can be stirred with a stir bar and a stir plate.

After the reaction, the pressured air of the reaction vessel is released to the gas outlet. With a flow-control needle valve, outgoing flow can be moderated. Slow release of the gas is recommended as a reaction mixture can be carried by a fast gas flow and escape from the reaction vessel. For a viscous reaction mixture, it is also recommended to freeze the reaction mixture before the gas release. This trick helps much to contain the reaction mixture in the reaction vessel. After the pressure release, the reaction vessel unit is detached with the needle valve closed and transferred to a glovebox for air-free work-up.

3.2.4. A Reactor System with High-Pressure Injection and Aliquoting Capabilities

Injection and aliquot taking have been popular for nanoparticle synthesis in ambient pressure. Hot injection and continuous injection of reaction precursor are popular methods not only for nanoparticle synthesis but for shell growth on nanoparticle cores. Aliquot taking is to analyze reaction mixtures over reaction time without quenching a reaction. This increases amount of information from a reaction and provides clue for a reaction mechanism.

For a high-pressure reactor, these capabilities have been limited, as an injection needs to overcome a pressure difference and an aliquot taking needs a control not to lose all gas pressure during aliquoting. A plunger pump used for high-performance liquid chromatography (HPLC) can be utilized for high-pressure injection purpose. A single plunger pump from GL Science can deliver up to 5mL/min with maximum 10 MPa (1450 psi) pressure. For high-pressure aliquot taking, the system is equipped with a 4878 Automated Liquid Sampler from Parr Instrument. This programmable sampler can aliquot multiple times along the reaction through the dip tube from a

reaction mixture under high-pressure atmosphere. Any non-colloidal solid is filtered by a frit filter covering the dip tube.

Figure 3.6 depicts a scheme for the reactor system. Other than HPLC pump and the liquid sampler, this system is similar to the previously discussed reactor system for high-pressure ammonia delivery. A detachable reactor unit is connected with another high-pressure vessel containing liquid ammonia. The reactor vessel is also connected with a HPLC pump through 1/16" tubing bored-through 1/4" tubings and fittings. The aliquoting sampler is connected to the dip tube of the reactor unit. All three connections are equipped with needle valves so that the reactor unit can be air-tight during transfer in and out of the glovebox.

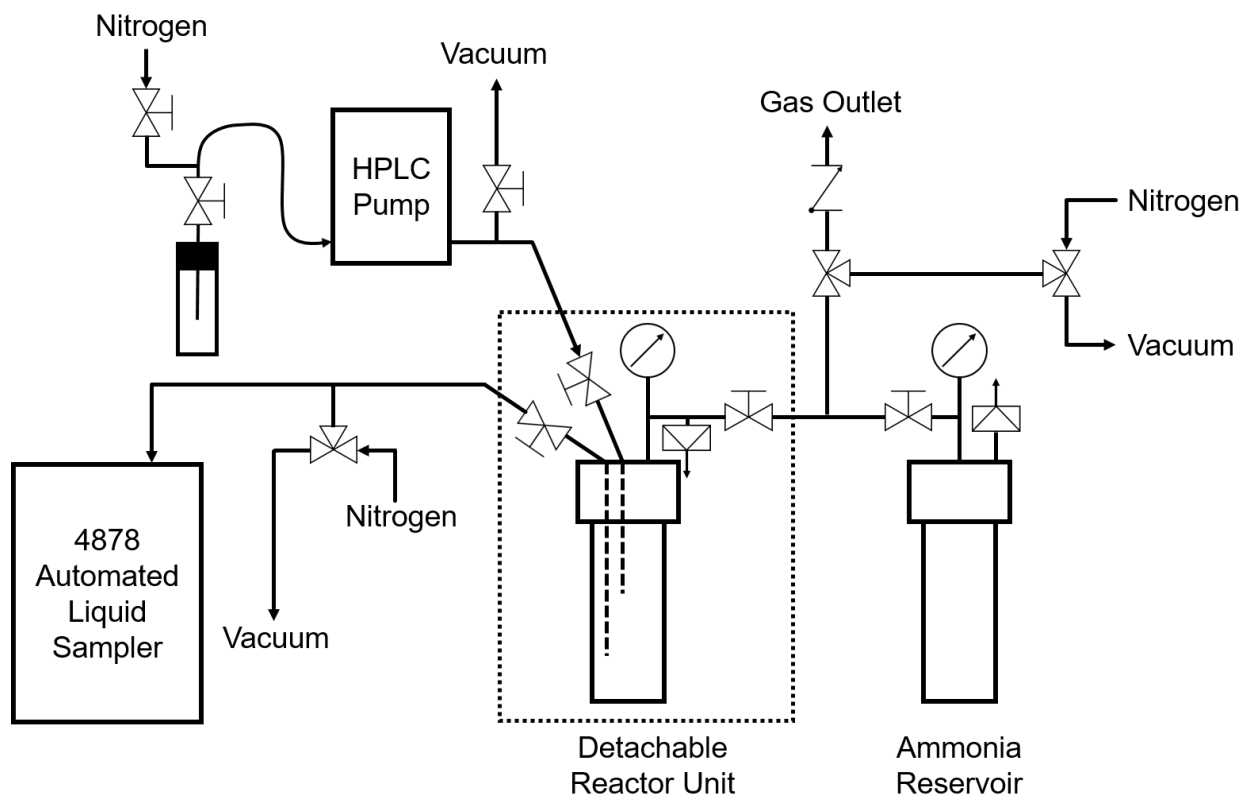


Figure 3.6. A flow diagram of a high-pressure reactor system with a capability of high-pressure injection and aliquoting.

The operation of this reactor system is similar to other reactor systems discussed previously. The detachable unit can be brought into a glovebox to contain reaction mixture, transferred out air-tight with three attached needle valves closed, and assembled to the system. For a high-pressure injection, additive solution is prepared inside of a glovebox and loaded in a vial with an air-tight cap having a dip tube and a needle valve. With the needle valve closed, the vial is brought out of the glovebox and attached to the system. Any air-exposed part of the reactor including the whole HPLC line is evacuated by cycles of vacuum evacuation and nitrogen refill. The reaction mixture can also be stirred with a stir bar and a stir plate, and heated with heating tape around the reaction vessel. With a temperature controller, reaction temperature is precisely controlled. A thermocouple for the controller can be placed in between reactor vessel and the heat source, or in a thermowell of the reactor vessel. Ammonia reservoir can be heated to a desired pressure without precise temperature control if high-pressure ammonia is needed for the reaction. At desired temperature and pressure, the additive solution is added with HPLC pump. At desired reaction times, 4878 Automated Liquid Sampler takes desired amount of aliquots.

After the reaction ends, heat source is removed and the reactor unit is cooled to a room temperature. High-pressure gas is released to the gas outlet during cooling down if needed. After cooling down and pressure release, all three valves of the detachable reactor unit are closed, and the reactor unit is separated from the system. The reactor unit can be transferred into a glovebox for air-free work-up.

3.3. Example Experiments with High-Pressure Reactors

3.3.1. Synthesis of Gallium Nitride Phase in Molten Halide Eutectic

Eutectic mixtures of alkali halides can have melting points lower than a reaction temperature of common nanoparticle synthesis. Potassium iodide (KI) and lithium iodide (LiI) makes a eutectic phase with melting point of 260.0 °C at the composition with 36.9 mol% KI. In a nitrogen atmosphere, to 2 g of this anhydrous iodide eutectic, 200 mg of anhydrous gallium iodide was mixed. This mixture was filled in a dried boron nitride crucible, and this crucible was placed inside of the thick glass reactor vessel. It is important to place a cushion material in between the glass reactor and the crucible, because glass thermally expands and shrinks during heating up and cooling down the reactor, and the crucible damages the outer glass reactor during cooling down if they contact each other directly. A glass or quartz wool is a good option for this. The reactor vessel was assembled air-freely to the reactor system. The mixture of salts was heated to 300 °C to become homogenous melt under ambient nitrogen atmosphere, and around 100 psi (7 bar) of gaseous ammonia was flowed into the reactor. The reaction occurred almost instantly upon ammonia injection, fuming white fog of ammonium iodide. After 30 minutes, a heat source was removed and the reactor was cooled to a room temperature. The reactor unit was detached with the needle valve closed, and transferred into a glovebox. The reaction mixture was washed with methanol to dissolve unreacted iodide eutectic and ammonium iodide byproduct. After several times of washing, undissolved light yellow solids were collected and stored under nitrogen atmosphere.

Resulted solid could not be turned colloidal with addition of long carbon chain carboxylates or amines. Powder X-ray diffraction (PXRD) of this solid matches with wurtzite (WZ) gallium

nitride (GaN) phase, with sharp features hinting formation of large particles (Figure 3.7 A). Transmission electron microscopy (TEM) backs up this showing urchin-like particles over 100nm with large size distribution (Figure 3.7 B-C). Apparently this method failed to produce nanoparticles with desired properties. However, this reaction succeeded to make a desired phase and hinted that GaN nanoparticles may be produced in molten salt. As direct synthesis of nanoparticles in molten salt media is not fully understood yet, this reaction system can be a viable starting point for a future project.

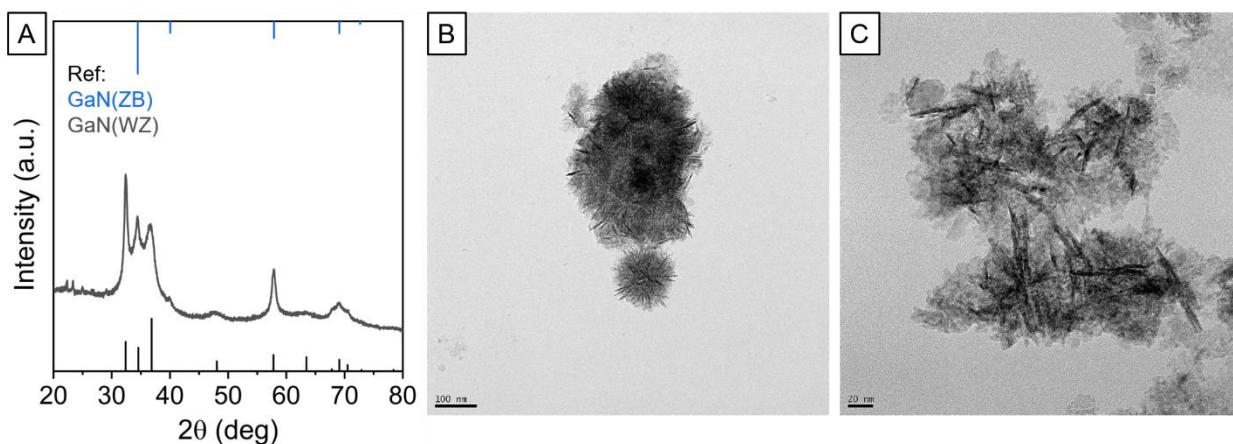


Figure 3.7. (A) Powder X-ray diffraction (PXRD) pattern, (B) TEM image, and (C) high-resolution of TEM image of produced particles from the reaction of GaI₃ in iodide eutectic and ammonia.

Resulted solid could not be turned colloidal with addition of long carbon chain carboxylates or amines. Powder X-ray diffraction (PXRD) of this solid matches with wurtzite (WZ) gallium nitride (GaN) phase, with sharp features hinting formation of large particles (Figure 3.7 A). Transmission electron microscopy (TEM) backs up this showing urchin-like particles over 100nm with large size distribution (Figure 3.7 B-C). Apparently this method failed to produce nanoparticles with desired properties. However, this reaction succeeded to make a desired phase

and hinted that GaN nanoparticles may be produced in molten salt. As direct synthesis of nanoparticles in molten salt media is not fully understood yet, this reaction system can be a viable starting point for a future project.

3.3.2. Synthesis of Gallium Nitride Nanoparticles with High-Pressure Ammonia

As shown in the previous chapter, gallium nitride nanoparticles can be synthesized from hot-injection of high-pressure ammonia to a mixture of potassium tetraiodogallate (KGaCl_4), trioctylamine (TOA), and hexadecylamine (HDA). It is shown that the pressure of ammonia affected the thickness of resulted GaN nanorods. The reaction was performed in the reactor system described in the section 3.2.2. with a method described in the section 2.10.6.

In detail, the head part, the reactor vessel, and the silicon nitride liner of the detachable reactor unit were heated in an oven set to 100 °C, and transferred to a nitrogen glovebox before they were still at elevated temperature. With a vacuum evacuation in an antechamber of the glovebox, any moisture on these parts could be removed. The parts were cooled down to a room temperature inside of the glovebox. To the silicon nitride liner, 5 mmol of finely ground KGaCl_4 , 4 mL of TOA, and 0.6 g of HDA were loaded together with a glass stir bar. After the silicon nitride liner was placed inside the reactor vessel, the vessel and the head part was assembled together having a graphite gasket in between. The assembled reactor unit was brought out of the glovebox and connected to the reactor system. After the reaction vessel was assembled to the system, two pressure vessels were heated separately; the reactor vessel was heated to 290 °C under ambient pressure nitrogen with vigorous stirring, while the ammonia reservoir was heated gently to a pressure about 2-3 MPa higher than the target pressure. If the temperature of a reactor unit was

measured from outside wall of the reactor vessel, the temperature was held at 290 °C for at least 10 minutes before ammonia transfer to provide enough time for the reaction mixture to reach the desired reaction temperature. When both pressure vessels were readied, desired pressure of hot ammonia gas was transferred by manipulating the two needle valves between the two pressure vessels. During this process, the needle valve toward the Schlenk line must be closed. All needle valves were closed after the transfer. After 1 hour of reaction, pressurized gas in the reaction vessel was slowly vented until the pressure reached 1 MPa, a pressure high enough to prevent back flow of an air into the vessel during venting and low enough to avoid a condensation of liquid ammonia during cooling. The reaction vessel was cooled to a room temperature and transferred into a nitrogen glovebox. The reaction product was washed with toluene and methanol a few times each. Colloidal solutions of these products were obtained by sonication of the solid products with 16 mL of *n*-hexane (or toluene), 2 mL of oleylamine, and 2 mL of oleic acid. Nanoparticles were flocculated with ethanol from this solution, collected by centrifugation, and dispersed in methylcyclohexane or *n*-hexane for subsequent measurements.

3.3.3. Hot Isostatic Pressing of ZnS and ZnSe Nanoparticle Thin Films¹¹⁵

Not only in the chemical reaction, but also in post-synthetic treatment, a high-pressure reactor can be utilized. Hot-isostatic pressing is a popular process to reduce porosity of a material. Using high-pressure reactor system described in the section 3.2.3, hot isostatic pressing on nanoparticle thin film was performed. Thin films produced by spin-coating of ZnS and ZnSe nanoparticle solution were placed in the reactor vessel. The reactor vessel was assembled with a head part unit and connected to the reactor system. As these nanoparticle films were not air-sensitive, assembly process could be performed outside of a glovebox. Then, the whole system

was evacuated with cycles of vacuum evacuation and nitrogen fill. Finally, the vessel was filled with high-pressure nitrogen and heated to desired temperature to have desired pressure. Required nitrogen pressure at room temperature was estimated based on the ideal gas law. After 16 hours of heating, the vessel was cooled to a room temperature, pressured air was released, and the thin films were retrieved. The retrieved films were investigated with an optical microscope, scanning electron microscope (SEM), and ellipsometer. Both ZnS and ZnSe thin films showed increase of packing density and refractive indices (Figure 3.8).

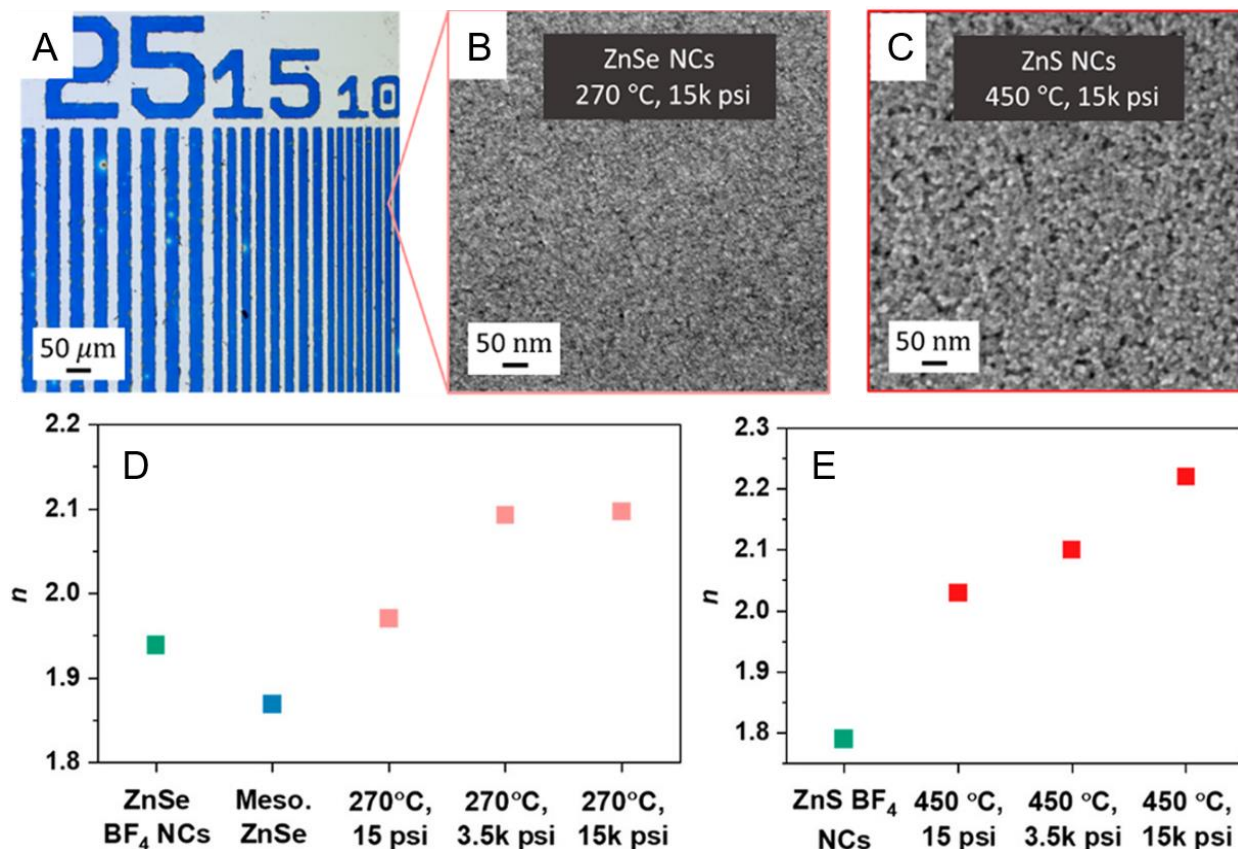


Figure 3.8. Hot isostatic pressing of ZnS and ZnSe nanoparticle films. (A) Optical microscopy and (B) SEM image of film of ZnSe nanoparticles after hot isostatic pressing at 270 °C and 15000 psi (100 MPa). (C) SEM image of film of ZnS nanoparticles after hot isostatic pressing at 450 °C and 15000 psi (100 MPa). (D) Refractive indices of ZnSe nanoparticle films before and after hot isostatic pressing. (E) Refractive indices of ZnS nanoparticle films before and after hot isostatic pressing. Adapted with permission from Ref. [115]. Copyright 2022 American Chemical Society.

3.4. Summary and Outlook

Multiple high-pressure reactor systems are described in this chapter. Descriptions on reactors are mainly focused on utilizing ammonia and nitrogen, but other gases can also be utilized in the similar way if necessary. Air-free operations of the high-pressure reactor are also explained. The key to the air-free operation is to have a detachable reactor unit with a needle valve so that the reactor vessel can be prepared under inert atmosphere and sealed completely during transfer and assembly to the reactor system.

A few example experiments of reactor operations are described. GaN phase could be nucleated in molten salt media under pressure of ammonia. GaN nanorod synthesized in the biphasic mixture of KGaCl_4 and alkylamines could be tuned to different thickness by controlling ammonia pressure. Also, thin films of ZnSe and ZnS nanoparticles could be annealed to denser films through hot isostatic pressing in the high-pressure reactor.

High-pressure reactor systems can also be utilized in many other experiments. One interesting immediate research will be a cation exchange on III-nitride nanomaterials. As described at the beginning of this chapter, high-pressure nitrogen will allow higher reaction temperature with increase of thermal stability of III-nitrides.⁵⁶ At higher reaction temperature, exchange reaction rate is faster as well as a diffusion rate of cations into the III-nitride nanocrystal increases providing higher opportunity to result in a uniform cation exchange throughout the nanocrystal.

REFERENCES

1. Talapin, D. V.; Shevchenko, E. V. Introduction: Nanoparticle Chemistry. *Chem. Rev.* **2016**, *116*, 10343-10345.
2. Chang, J.; Waclawik, E. R. Colloidal Semiconductor Nanocrystals: Controlled Synthesis and Surface Chemistry in Organic Media. *RSC Adv.* **2014**, *4*, 23505-23527.
3. Gaponik, N.; Hickey, S. G.; Dorfs, D.; Rogach, A. L.; Eychmüller, A. Progress in the Light Emission of Colloidal Semiconductor Nanocrystals. *Small* **2010**, *6*, 1364-1378.
4. Kovalenko, M. V.; Manna, L.; Cabot, A.; Hens, Z.; Talapin, D. V.; Kagan, C. R.; Klimov, V. I.; Rogach, A. L.; Reiss, P.; Milliron, D. J.; Guyot-Sionnest, P.; Konstantatos, G.; Parak, W. J.; Hyeon, T.; Korgel, B. A.; Murray, C. B.; Heiss, W. Prospects of Nanoscience with Nanocrystals. *ACS Nano* **2015**, *9*, 1012-1057.
5. Talapin, D. V.; Lee, J.-S.; Kovalenko, M. V.; Shevchenko, E. V. Prospects of Colloidal Nanocrystals for Electronic and Optoelectronic Applications. *Chem. Rev.* **2010**, *110*, 389-458.
6. Kagan, C. R.; Lifshitz, E.; Sargent, E. H.; Talapin, D. V. Building Devices from Colloidal Quantum Dots. *Science* **2016**, *353*, aac5523.
7. Thanh, N. T. K.; Maclean, N.; Mahiddine, S. Mechanisms of Nucleation and Growth of Nanoparticles in Solution. *Chem. Rev.* **2014**, *114*, 7610-7630.
8. LaMer, V. K.; Dinegar, R. H. Theory, Production and Mechanism of Formation of Monodispersed Hydrosols. *J. Am. Chem. Soc.* **1950**, *72*, 4847-4854.
9. Prins, P. T.; Montanarella, F.; Dümbgen, K.; Justo, Y.; van der Bok, J. C.; Hinterding, S. O. M.; Geuchies, J. J.; Maes, J.; De Nolf, K.; Deelen, S.; Meijer, H.; Zinn, T.; Petukhov, A. V.; Rabouw, F. T.; De Mello Donega, C.; Vanmaekelbergh, D.; Hens, Z. Extended Nucleation and Superfocusing in Colloidal Semiconductor Nanocrystal Synthesis. *Nano Lett.* **2021**, *21*, 2487-2496.
10. McMurtry, B. M.; Qian, K.; Teglassi, J. K.; Swarnakar, A. K.; De Roo, J.; Owen, J. S. Continuous Nucleation and Size Dependent Growth Kinetics of Indium Phosphide Nanocrystals. *Chem. Mater.* **2020**, *32*, 4358-4368.
11. Ostwald, W. Über die Vermeintliche Isomerie des Roten und Gelben Quecksilberoxyds und die Oberflächenspannung Fester Körper. *Z. Phys. Chem.* **1900**, *34*, 495-503.
12. Talapin, D. V.; Rogach, A. L.; Haase, M.; Weller, H. Evolution of an Ensemble of Nanoparticles in a Colloidal Solution: Theoretical Study. *J. Phys. Chem. B* **2001**, *105*, 12278-12285.
13. Lee, D.-K.; Park, S.-I.; Lee, J. K.; Hwang, N.-M. A Theoretical Model for Digestive Ripening. *Acta Mater.* **2007**, *55*, 5281-5288.

14. Ithurria, S.; Dubertret, B. Quasi 2D Colloidal CdSe Platelets with Thicknesses Controlled at the Atomic Level. *J. Am. Chem. Soc.* **2008**, *130*, 16504-16505.
15. Manthiram, K.; Beberwyck, B. J.; Talapin, D. V.; Au - Alivisatos, A. P. Seeded Synthesis of CdSe/CdS Rod and Tetrapod Nanocrystals. *J. Vis. Exp.* **2013**, *82*, e50731.
16. Manna, L.; Scher, E. C.; Alivisatos, A. P. Synthesis of Soluble and Processable Rod-, Arrow-, Teardrop-, and Tetrapod-Shaped CdSe Nanocrystals. *J. Am. Chem. Soc.* **2000**, *122*, 12700-12706.
17. Liu, L.; Zhuang, Z.; Xie, T.; Wang, Y.-G.; Li, J.; Peng, Q.; Li, Y. Shape Control of CdSe Nanocrystals with Zinc Blende Structure. *J. Am. Chem. Soc.* **2009**, *131*, 16423-16429.
18. Zhou, J. H.; Zhu, M. Y.; Meng, R. Y.; Qin, H. Y.; Peng, X. G. Ideal CdSe/CdS Core/Shell Nanocrystals Enabled by Entropic Ligands and Their Core Size-, Shell Thickness-, and Ligand-Dependent Photoluminescence Properties. *J. Am. Chem. Soc.* **2017**, *139*, 16556-16567.
19. Cho, W.; Kim, S.; Coropceanu, I.; Srivastava, V.; Diroll, B. T.; Hazarika, A.; Fedin, I.; Galli, G.; Schaller, R. D.; Talapin, D. V. Direct Synthesis of Six-Monolayer (1.9 nm) Thick Zinc-Blende CdSe Nanoplatelets Emitting at 585 nm. *Chem. Mater.* **2018**, *30*, 6957-6960.
20. Cho, W.; Zhou, Z.; Lin, R.; Ondry, J. C.; Talapin, D. V. Synthesis of Colloidal GaN and AlN Nanocrystals in Biphasic Molten Salt/Organic Solvent Mixtures under High-Pressure Ammonia. *ACS Nano* **2023**, *17*, 1315-1326.
21. Riedinger, A.; Ott, F. D.; Mule, A.; Mazzotti, S.; Knüsel, P. N.; Kress, Stephan J. P.; Prins, F.; Erwin, S. C.; Norris, D. J. An Intrinsic Growth Instability in Isotropic Materials Leads to Quasi-Two-Dimensional Nanoplatelets. *Nat. Mater.* **2017**, *16*, 743-748.
22. Nasilowski, M.; Mahler, B.; Lhuillier, E.; Ithurria, S.; Dubertret, B. Two-Dimensional Colloidal Nanocrystals. *Chem. Rev.* **2016**, *116*, 10934-10982.
23. Lembke, D.; Bertolazzi, S.; Kis, A. Single-Layer MoS₂ Electronics. *Acc. Chem. Res.* **2015**, *48*, 100-110.
24. Lhuillier, E.; Pedetti, S.; Ithurria, S.; Nadal, B.; Heuclin, H.; Dubertret, B. Two-Dimensional Colloidal Metal Chalcogenides Semiconductors: Synthesis, Spectroscopy, and Applications. *Acc. Chem. Res.* **2015**, *48*, 22-30.
25. Lv, R.; Robinson, J. A.; Schaak, R. E.; Sun, D.; Sun, Y.; Mallouk, T. E.; Terrones, M. Transition Metal Dichalcogenides and Beyond: Synthesis, Properties, and Applications of Single- and Few-Layer Nanosheets. *Acc. Chem. Res.* **2015**, *48*, 56-64.
26. Bekenstein, Y.; Koscher, B. A.; Eaton, S. W.; Yang, P.; Alivisatos, A. P. Highly Luminescent Colloidal Nanoplates of Perovskite Cesium Lead Halide and Their Oriented Assemblies. *J. Am. Chem. Soc.* **2015**, *137*, 16008-16011.
27. Akkerman, Q. A.; Motti, S. G.; Srimath Kandada, A. R.; Mosconi, E.; D'Innocenzo, V.; Bertoni, G.; Marras, S.; Kamino, B. A.; Miranda, L.; De Angelis, F.; Petrozza, A.; Prato, M.; Manna, L. Solution Synthesis Approach to Colloidal Cesium Lead Halide Perovskite Nanoplatelets with Monolayer-Level Thickness Control. *J. Am. Chem. Soc.* **2016**, *138*, 1010-1016.

28. Li, Z.; Qin, H.; Guzun, D.; Benamara, M.; Salamo, G.; Peng, X. Uniform Thickness and Colloidal-Stable CdS Quantum Disks with Tunable Thickness: Synthesis and Properties. *Nano Res.* **2012**, *5*, 337-351.
29. Pedetti, S.; Nadal, B.; Lhuillier, E.; Mahler, B.; Bouet, C.; Abécassis, B.; Xu, X.; Dubertret, B. Optimized Synthesis of CdTe Nanoplatelets and Photoresponse of CdTe Nanoplatelets Films. *Chem. Mater.* **2013**, *25*, 2455-2462.
30. Scott, R.; Kickhofel, S.; Schoeps, O.; Antanovich, A.; Prudnikau, A.; Chuvilin, A.; Woggon, U.; Artemyev, M.; Achtstein, A. W. Temperature Dependent Radiative and Non-Radiative Recombination Dynamics in CdSe-CdTe and CdTe-CdSe Type II Hetero Nanoplatelets. *Phys. Chem. Chem. Phys.* **2016**, *18*, 3197-3203.
31. Wang, F.; Wang, Y.; Liu, Y.-H.; Morrison, P. J.; Loomis, R. A.; Buhro, W. E. Two-Dimensional Semiconductor Nanocrystals: Properties, Templated Formation, and Magic-Size Nanocluster Intermediates. *Acc. Chem. Res.* **2015**, *48*, 13-21.
32. Lhuillier, E.; Pedetti, S.; Ithurria, S.; Heuclin, H.; Nadal, B.; Robin, A.; Patriarche, G.; Lequeux, N.; Dubertret, B. Electrolyte-Gated Field Effect Transistor to Probe the Surface Defects and Morphology in Films of Thick CdSe Colloidal Nanoplatelets. *ACS Nano* **2014**, *8*, 3813-3820.
33. Bouet, C.; Mahler, B.; Nadal, B.; Abecassis, B.; Tessier, M. D.; Ithurria, S.; Xu, X.; Dubertret, B. Two-Dimensional Growth of CdSe Nanocrystals, from Nanoplatelets to Nanosheets. *Chem. Mater.* **2013**, *25*, 639-645.
34. Chen, Y.; Chen, D.; Li, Z.; Peng, X. Symmetry-Breaking for Formation of Rectangular CdSe Two-Dimensional Nanocrystals in Zinc-Blende Structure. *J. Am. Chem. Soc.* **2017**, *139*, 10009-10019.
35. Jana, S.; Phan, T. N. T.; Bouet, C.; Tessier, M. D.; Davidson, P.; Dubertret, B.; Abécassis, B. Stacking and Colloidal Stability of CdSe Nanoplatelets. *Langmuir* **2015**, *31*, 10532-10539.
36. Achtstein, A. W.; Schliwa, A.; Prudnikau, A.; Hardzei, M.; Artemyev, M. V.; Thomsen, C.; Woggon, U. Electronic Structure and Exciton-Phonon Interaction in Two-Dimensional Colloidal CdSe Nanosheets. *Nano Lett.* **2012**, *12*, 3151-3157.
37. Rowland, C. E.; Fedin, I.; Zhang, H.; Gray, S. K.; Govorov, A. O.; Talapin, D. V.; Schaller, R. D. Picosecond Energy Transfer and Multiexciton Transfer Outpaces Auger Recombination in Binary CdSe Nanoplatelet Solids. *Nat. Mater.* **2015**, *14*, 484-489.
38. Rossinelli, A. A.; Riedinger, A.; Marques-Gallego, P.; Knusel, P. N.; Antolinez, F. V.; Norris, D. J. High-Temperature Growth of Thick-Shell CdSe/CdS Core/Shell Nanoplatelets. *Chem. Comm.* **2017**, *53*, 9938-9941.
39. Mahler, B.; Nadal, B.; Bouet, C.; Patriarche, G.; Dubertret, B. Core/Shell Colloidal Semiconductor Nanoplatelets. *J. Am. Chem. Soc.* **2012**, *134*, 18591-18598.
40. Tessier, M. D.; Biadala, L.; Bouet, C.; Ithurria, S.; Abecassis, B.; Dubertret, B. Phonon Line Emission Revealed by Self-Assembly of Colloidal Nanoplatelets. *ACS Nano* **2013**, *7*, 3332-3340.

41. Chu, A.; Livache, C.; Ithurria, S.; Lhuillier, E. Electronic Structure Robustness and Design Rules for 2D Colloidal Heterostructures. *J. Appl. Phys.* **2018**, *123*, 035701.
42. Ott, F. D.; Riedinger, A.; Ochsenbein, D. R.; Knüsel, P. N.; Erwin, S. C.; Mazzotti, M.; Norris, D. J. Ripening of Semiconductor Nanoplatelets. *Nano Lett.* **2017**, *17*, 6870-6877.
43. Pelton, M.; Ithurria, S.; Schaller, R. D.; Dolzhenkov, D. S.; Talapin, D. V. Carrier Cooling in Colloidal Quantum Wells. *Nano Lett.* **2012**, *12*, 6158-6163.
44. Ithurria, S.; Tessier, M. D.; Mahler, B.; Lobo, R. P. S. M.; Dubertret, B.; Efros, A. L. Colloidal Nanoplatelets with Two-Dimensional Electronic Structure. *Nat. Mater.* **2011**, *10*, 936-941.
45. Kelley, A. M.; Dai, Q.; Jiang, Z.-J.; Baker, J. A.; Kelley D. F. Resonance Raman Spectra of Wurtzite and Zincblende CdSe Nanocrystals. *Chem. Phys.* **2013**, *422*, 272-276.
46. Lovette, M. A.; Browning, A. R.; Griffin, D. W.; Sizemore, J. P.; Snyder, R. C.; Doherty, M. F. Crystal Shape Engineering. *Ind. & Eng. Chem. Res.* **2008**, *47*, 9812-9833.
47. Boles, M. A.; Ling, D.; Hyeon, T.; Talapin, D. V. The Surface Science of Nanocrystals. *Nat. Mater.* **2016**, *15*, 141-153.
48. Zherebetsky, D.; Scheele, M.; Zhang, Y.; Bronstein, N.; Thompson, C.; Britt, D.; Salmeron, M.; Alivisatos, P.; Wang, L.-W. Hydroxylation of the Surface of PbS Nanocrystals Passivated with Oleic Acid. *Science* **2014**, *344*, 1380-1384.
49. She, C.; Fedin, I.; Dolzhenkov, D. S.; Dahlberg, P. D.; Engel, G. S.; Schaller, R. D.; Talapin, D. V. Red, Yellow, Green, and Blue Amplified Spontaneous Emission and Lasing Using Colloidal CdSe Nanoplatelets. *ACS Nano* **2015**, *9*, 9475-9485.
50. She, C.; Fedin, I.; Dolzhenkov, D. S.; Demortière, A.; Schaller, R. D.; Pelton, M.; Talapin, D. V. Low-Threshold Stimulated Emission Using Colloidal Quantum Wells. *Nano Lett.* **2014**, *14*, 2772-2777.
51. Ithurria, S.; Talapin, D. V. Colloidal Atomic Layer Deposition (c-ALD) using Self-Limiting Reactions at Nanocrystal Surface Coupled to Phase Transfer between Polar and Nonpolar Media. *J. Am. Chem. Soc.* **2012**, *134*, 18585-18590.
52. Hazarika, A.; Fedin, I.; Hong, L.; Guo, J.; Srivastava, V.; Cho, W.; Coropceanu, I.; Portner, J.; Diroll, B. T.; Philbin, J. P.; Rabani, E.; Klie, R.; Talapin, D. V. Colloidal Atomic Layer Deposition with Stationary Reactant Phases Enables Precise Synthesis of “Digital” II–VI Nano-Heterostructures with Exquisite Control of Confinement and Strain. *J. Am. Chem. Soc.* **2019**, *141*, 13487-13496.
53. Dufour, M.; Qu, J.; Greboval, C.; Méthivier, C.; Lhuillier, E.; Ithurria, S. Halide Ligands To Release Strain in Cadmium Chalcogenide Nanoplatelets and Achieve High Brightness. *ACS Nano* **2019**, *13*, 5326–5334.
54. Nakamura, S.; Mukai, T.; Senoh, M.; Iwasa, N. Thermal Annealing Effects on P-Type Mg-Doped GaN Films. *Jpn. J. Appl. Phys.* **1992**, *31*, L139-L142.

55. Ding, X.; Zhou, Y.; Cheng, J. A Review of Gallium Nitride Power Device and Its Applications in Motor Drive. *CES trans. electr. mach. syst.* **2019**, *3*, 54-64.
56. Oda, O. Nitride and Other III-V Compounds. In *Compound Semiconductor Bulk Materials and Characterizations*; World Scientific Publishing Co.: Singapore, 2012; Vol. 2, pp 27-125.
57. Raty, J.-Y.; Schumacher, M.; Golub, P.; Deringer, V. L.; Gatti, C.; Wuttig, M. A Quantum-Mechanical Map for Bonding and Properties in Solids. *Adv. Mater.* **2019**, *31*, 1806280.
58. Iqbal, A.; Mohd-Yasin, F. Reactive Sputtering of Aluminum Nitride (002) Thin Films for Piezoelectric Applications: A Review. *Sensors* **2018**, *18*, 1797.
59. Liu, G.; Zhou, G.; Qin, Z.; Zhou, Q.; Zheng, R.; Wu, H.; Sun, Z. Luminescence Characterizations of Freestanding Bulk Single Crystalline Aluminum Nitride towards Optoelectronic Application. *CrystEngComm* **2017**, *19*, 5522-5527.
60. Lu, T.-J.; Fanto, M.; Choi, H.; Thomas, P.; Steidle, J.; Mouradian, S.; Kong, W.; Zhu, D.; Moon, H.; Berggren, K.; Kim, J.; Soltani, M.; Preble, S.; Englund, D. Aluminum Nitride Integrated Photonics Platform for the Ultraviolet to Visible Spectrum. *Opt. express* **2018**, *26*, 11147-11160.
61. Bondokov, R. T.; Mueller, S. G.; Morgan, K. E.; Slack, G. A.; Schujman, S.; Wood, M. C.; Smart, J. A.; Schowalter, L. J. Large-Area AlN Substrates for Electronic Applications: An Industrial Perspective. *J. Cryst. Growth* **2008**, *310*, 4020-4026.
62. Piazza, G.; Stephanou, P. J.; Pisano, A. P. Piezoelectric Aluminum Nitride Vibrating Contour-Mode MEMS Resonators. *J. Microelectromech. Syst.* **2006**, *15*, 1406-1418.
63. Bhattacharyya, A.; Moustakas, T.; Zhou, L.; Smith, D. J.; Hug, W. Deep Ultraviolet Emitting AlGaIn Quantum Wells with High Internal Quantum Efficiency. *Appl. Phys. Lett.* **2009**, *94*, 181907.
64. Wang, Y.; Fedin, I.; Zhang, H.; Talapin, D. V. Direct Optical Lithography of Functional Inorganic Nanomaterials. *Science* **2017**, *357*, 385-388.
65. Jones, A. C.; Whitehouse, C. R.; Roberts, J. S. Chemical Approaches to the Metalorganic CVD of Group-III Nitrides. *Chem. Vap. Deposition* **1995**, *1*, 65-74.
66. Richter, T. M.; Niewa, R. Chemistry of Ammonothermal Synthesis. *Inorganics* **2014**, *2*, 29-78.
67. Han, W.; Fan, S.; Li, Q.; Hu, Y. Synthesis of Gallium Nitride Nanorods through a Carbon Nanotube-Confined Reaction. *Science* **1997**, *277*, 1287-1289.
68. Goldberger, J.; He, R.; Zhang, Y.; Lee, S.; Yan, H.; Choi, H.-J.; Yang, P. Single-Crystal Gallium Nitride Nanotubes. *Nature* **2003**, *422*, 599-602.
69. Tang, Y.; Cong, H.; Zhao, Z.; Cheng, H. Field Emission from AlN Nanorod Array. *Appl. Phys. Lett.* **2005**, *86*, 153104.

70. Shen, L.; Lv, W.; Wang, N.; Wu, L.; Qi, D.; Ma, Y.; Lei, W. Controllable Synthesis of AlN Nanostructures and Their Photoluminescence. *CrystEngComm* **2017**, *19*, 5940-5945.
71. Lei, W.; Liu, D.; Zhang, J.; Zhu, P.; Cui, Q.; Zou, G. Direct Synthesis, Growth Mechanism, and Optical Properties of 3D AlN Nanostructures with Urchin Shapes. *Cryst. Growth Des.* **2009**, *9*, 1489-1493.
72. Zhang, F.; Wu, Q.; Wang, X.; Liu, N.; Yang, J.; Hu, Y.; Yu, L.; Wang, X.; Hu, Z.; Zhu, J. 6-Fold-Symmetrical AlN Hierarchical Nanostructures: Synthesis and Field-Emission Properties. *J. Phys. Chem. C* **2009**, *113*, 4053-4058.
73. Chen, F.; Ji, X.; Lau, S. P. Recent Progress in Group III-Nitride Nanostructures: From Materials to Applications. *Mater. Sci. Eng. R Rep.* **2020**, *142*, 100578.
74. Al Balushi, Z. Y.; Wang, K.; Ghosh, R. K.; Vilá, R. A.; Eichfeld, S. M.; Caldwell, J. D.; Qin, X.; Lin, Y.-C.; DeSario, P. A.; Stone, G.; Subramanian, S.; Paul, D. F.; Wallace, R. M.; Datta, S.; Redwing, J. M.; Robinson, J. A. Two-Dimensional Gallium Nitride Realized via Graphene Encapsulation. *Nat. Mater.* **2016**, *15*, 1166-1171.
75. Chen, Y.; Liu, K.; Liu, J.; Lv, T.; Wei, B.; Zhang, T.; Zeng, M.; Wang, Z.; Fu, L. Growth of 2D GaN Single Crystals on Liquid Metals. *J. Am. Chem. Soc.* **2018**, *140*, 16392-16395.
76. Sardar, K.; Rao, C. New Solvothermal Routes for GaN Nanocrystals. *Adv. Mater.* **2004**, *16*, 425-429.
77. Choi, Y. C.; Kim, H.; Lee, C.; Son, J.; Baik, H.; Park, S.; Kim, J.; Jeong, K. S. Blue Emission of α -GaN Colloidal Quantum Dots via Zn Doping. *Chem. Mater.* **2019**, *31*, 5370-5375.
78. Manz, A.; Birkner, A.; Kolbe, M.; Fischer, R. A. Solution Synthesis of Colloidal Gallium Nitride at Unprecedented Low Temperatures. *Adv. Mater.* **2000**, *12*, 569-573.
79. Mičić, O.; Ahrenkiel, S.; Bertram, D.; Nozik, A. J. Synthesis, Structure, and Optical Properties of Colloidal GaN Quantum Dots. *Appl. Phys. Lett.* **1999**, *75*, 478-480.
80. Pan, G.; Kordesch, M. E.; Van Patten, P. G. New Pyrolysis Route to GaN Quantum Dots. *Chem. Mater.* **2006**, *18*, 3915-3917.
81. Lan, Y.; Chen, X.; Cao, Y.; Xu, Y.; Xun, L.; Xu, T.; Liang, J. Low-Temperature Synthesis and Photoluminescence of AlN. *J. Cryst. Growth* **1999**, *207*, 247-250.
82. Sardar, K.; Rao, C. AlN Nanocrystals by New Chemical Routes. *Solid State Sci.* **2005**, *7*, 217-220.
83. Lu, S.; Tong, Y.; Liu, Y.; Xu, C.; Lu, Y.; Zhang, J.; Shen, D.; Fan, X. The Structure and Optical Properties of AlN Nanocrystals Prepared by Schlenk Techniques at Atmospheric Pressure and Low Temperature. *J. Phys. Chem. Solids* **2005**, *66*, 1609-1613.
84. Whitelam, S.; Jack, R. L. The Statistical Mechanics of Dynamic Pathways to Self-Assembly. *Annu. Rev. Phys. Chem.* **2015**, *66*, 143-163.
85. Luo, Y.-R.; Kerr, J. A. Bond Dissociation Energies. In *CRC Handbook of Chemistry and Physics*, 87th ed.; Lide, D. R., Ed.; CRC Press/Taylor and Francis: Boca Raton, FL, 2006.

86. Kandalam, A. K.; Pandey, R.; Blanco, M.; Costales, A.; Recio, J.; Newsam, J. M. First Principles Study of Polyatomic Clusters of AlN, GaN, and InN. 1. Structure, Stability, Vibrations, and Ionization. *J. Phys. Chem. B* **2000**, *104*, 4361-4367.
87. Herndon, L. R.; Reid, E. E. The Decomposition of Organic Compounds at High Temperatures and Pressures. *J. Am. Chem. Soc.* **1928**, *50*, 3066-3073.
88. Reiss, P.; Carriere, M.; Lincheneau, C.; Vaure, L.; Tamang, S. Synthesis of Semiconductor Nanocrystals, Focusing on Nontoxic and Earth-Abundant Materials. *Chem. Rev.* **2016**, *116*, 10731-10819.
89. Fan, G.; Wang, C.; Fang, J. Solution-Based Synthesis of III–V Quantum Dots and Their Applications in Gas Sensing and Bio-Imaging. *Nano Today* **2014**, *9*, 69-84.
90. Ramasamy, P.; Kim, N.; Kang, Y.-S.; Ramirez, O.; Lee, J.-S. Tunable, Bright, and Narrow-Band Luminescence from Colloidal Indium Phosphide Quantum Dots. *Chem. Mater.* **2017**, *29*, 6893-6899.
91. Battaglia, D.; Peng, X. Formation of High Quality InP and InAs Nanocrystals in a Noncoordinating Solvent. *Nano Lett.* **2002**, *2*, 1027-1030.
92. Gates-Rector, S.; Blanton, T. The Powder Diffraction File: A Quality Materials Characterization Database. *Powder Diffr.* **2019**, *34*, 352-360.
93. Kinski, I.; Miehe, G.; Heymann, G.; Theissmann, R.; Riedel, R.; Huppertz, H. High-Pressure Synthesis of a Gallium Oxonitride with a Spinel-Type Structure. *Z. Naturforsch. B* **2005**, *60*, 831-836.
94. Yu, M.; Drabold, D. Density Dependence of the Structural and Electronic Properties of Amorphous GaN. *Solid State Commun.* **1998**, *108*, 413-417.
95. Waggoner, K. M.; Olmstead, M. M.; Power, P. P. Structural and Spectroscopic Characterization of the Compounds [Al(NMe₂)₃]₂, [Ga(NMe₂)₃]₂, [(Me₂N)₂Al{μ-N(H)1-Ad}]₂ (1-Ad = 1-Adamantanyl) and [{Me(μ-NPh₂)Al}₂NPh(μ-C₆H₄)]. *Polyhedron* **1990**, *9*, 257-263.
96. Peterson, P. F.; Božin, E. S.; Proffen, T.; Billinge, S. J. Improved Measures of Quality for the Atomic Pair Distribution Function. *J. Appl. Crystallogr.* **2003**, *36*, 53-64.
97. Anderson, N. C.; Hendricks, M. P.; Choi, J. J.; Owen, J. S. Ligand Exchange and the Stoichiometry of Metal Chalcogenide Nanocrystals: Spectroscopic Observation of Facile Metal-Carboxylate Displacement and Binding. *J. Am. Chem. Soc.* **2013**, *135*, 18536-18548.
98. Dumbgen, K. C.; Zito, J.; Infante, I.; Hens, Z. Shape, Electronic Structure, and Trap States in Indium Phosphide Quantum Dots. *Chem. Mater.* **2021**, *33*, 6885-6896.
99. Bugaris, D. E.; zur Loye, H. C. Materials Discovery by Flux Crystal Growth: Quaternary and Higher Order Oxides. *Angew. Chem. Int. Ed.* **2012**, *51*, 3780-3811.
100. Gupta, S. K.; Mao, Y. Recent Developments on Molten Salt Synthesis of Inorganic Nanomaterials: A Review. *J. Phys. Chem. C* **2021**, *125*, 6508-6533.

101. Wiley, J. B.; Kaner, R. B. Rapid Solid-State Precursor Synthesis of Materials. *Science* **1992**, *255*, 1093-1097.
102. Treece, R. E.; Macala, G. S.; Rao, L.; Franke, D.; Eckert, H.; Kaner, R. B. Synthesis of III-V Semiconductors by Solid-State Metathesis. *Inorg. Chem.* **1993**, *32*, 2745-2752.
103. Cunningham, P. D.; Coropceanu, I.; Mulloy, K.; Cho, W.; Talapin, D. V. Quantized Reaction Pathways for Solution Synthesis of Colloidal ZnSe Nanostructures: A Connection between Clusters, Nanowires, and Two-Dimensional Nanoplatelets. *ACS nano* **2020**, *14*, 3847-3857.
104. DuChene, J. S.; Niu, W.; Abendroth, J. M.; Sun, Q.; Zhao, W.; Huo, F.; Wei, W. D. Halide Anions as Shape-Directing Agents for Obtaining High-Quality Anisotropic Gold Nanostructures. *Chem. Mater.* **2013**, *25*, 1392-1399.
105. Filankembo, A.; Giorgio, S.; Lisiecki, I.; Pileni, M. Is the Anion the Major Parameter in the Shape Control of Nanocrystals? *J. Phys. Chem. B* **2003**, *107*, 7492-7500.
106. Ehretraut, D.; Kagamitani, Y. Acidic Ammonothermal Growth Technology for GaN. In *Technology of Gallium Nitride Crystal Growth*; Springer-Verlag Berlin Heidelberg: Berlin, Heidelberg, 2010; pp 183-203.
107. Toby, B. H.; Von Dreele, R. B. Gsas-II: The Genesis of a Modern Open-Source All Purpose Crystallography Software Package. *J. Appl. Crystallogr.* **2013**, *46*, 544-549.
108. Hirel, P. Atomsk: A Tool for Manipulating and Converting Atomic Data Files. *Comput. Phys. Commun.* **2015**, *197*, 212-219.
109. Momma, K.; Izumi, F. Vesta 3 for Three-Dimensional Visualization of Crystal, Volumetric and Morphology Data. *J. Appl. Crystallogr.* **2011**, *44*, 1272-1276.
110. Trigg, E. B. DebyeByPy. <https://github.com/etrigg/DebyeByPy> (Sep 25, 2022).
111. Cromer, D. T.; Mann, J. B. X-ray Scattering Factors Computed from Numerical Hartree-Fock Wave Functions. *Acta Crystallogr., Sect. A: Cryst. Phys., Diffr., Theor. Gen. Crystallogr.* **1968**, *24*, 321-324.
112. Bawendi, M. G.; Kortan, A. R.; Steigerwald, M. L.; Brus, L. E. X-ray Structural Characterization of Larger CdSe Semiconductor Clusters. *J. Chem. Phys.* **1989**, *91*, 7282-7290.
113. Juhás P.; Davis, T.; Farrow, C. L.; Billinge, S. J. L. PDFgetX3: A Rapid and Highly Automatable Program for Processing Powder Diffraction Data into Total Scattering Pair Distribution Functions. *J. Appl. Crystallogr.* **2013**, *46*, 560-566.
114. Srivastava, V.; Kamysbayev, V.; Hong, L.; Dunietz, E.; Klie, R. F.; Talapin, D. V. Colloidal Chemistry in Molten Salts: Synthesis of Luminescent In_{1-x}Ga_xP and In_{1-x}Ga_xAs Quantum Dots. *J. Am. Chem. Soc.* **2018**, *140*, 12144-12151.
115. Pan, J.-A.; Wu, H.; Gomez, A.; Ondry, J. C.; Portner, J.; Cho, W.; Hinkle, A.; Wang, D.; Talapin D. V. Ligand-Free Direct Optical Lithography of Bare Colloidal Nanocrystals via Photo-Oxidation of Surface Ions with Porosity Control. *ACS Nano* **2022**, *16*, 16067-16076.